EXPLORING LOW-OXYGEN CONDITIONS IN THE CAMBRIAN THROUGH TRILOBITES OF THE WHEELER SHALE

by

DOUGLAS L. JOHN

(Under the Direction of Sally Walker)

ABSTRACT

The Middle Cambrian Wheeler Shale of Utah is host to one of the most famous trilobite assemblages in North America. These trilobites are exceptionally well-preserved, and many bear an unusually thick encrustation of cone-in-cone calcite. The conditions under which these trilobites lived and were preserved has been scrutinized in many previous studies; however, more detailed study has led only to more outstanding questions about the paleoenvironment in the Cambrian.

The environment in the Wheeler Shale has been interpreted as dysoxic in the benthos, based on sedimentology and ichnofabric in the sediment, and on the occurrence of the benthic ptychopariid *Elrathia kingii* in low-diversity, high-abundance assemblages that are characteristic of such conditions in modern oceans. As a consequence of specialization for extreme low-oxygen conditions, *Elrathia* was proposed to be possibly symbiotic with sulfur-oxidizing bacteria, based on their morphological similarity to olenid trilobites. Olenids were previously proposed as symbiotic low-oxygen specialists, based on their morphology which would be well-suited to harboring symbionts.

However, the accuracy of a symbiotic interpretation and the presence of low-oxygen conditions that would predicate such symbiosis have not been directly examined.

This study addresses these questions by examining the morphological basis for interpreting symbiosis in trilobites, and comparing putatively symbiotic forms to the spectrum of morphologies among Cambrian trilobites. I search for direct evidence of sulfur-oxidizing bacterial symbionts through molecular biomarkers associated with trilobite exoskeletons. I perform several geochemical analyses that constrain the extent and position of low-oxygen conditions above and below the sediment-water interface. I found that symbiosis was not well supported in trilobites, and morphology may be related more to taxonomic relationships than to environmental constraints such as reduced oxygen. While biomarker evidence of bacterial symbionts was not found, fossils from the Wheeler Shale revealed a suite of other biomarkers indicating more about Anthropocene terrestrial changes, indicating fossils may be a storehouse for information about modern ecosystem dynamics. Geochemistry suggests that benthic conditions were not extremely dysoxic, and the distribution of *Elrathia* may not be related to specialization for extreme low oxygen.

INDEX WORDS: Trilobite, Cambrian, Wheeler Shale, Symbiosis, Morphology, Paleoenvironment, Biomarker, Anthropocene, Geochemistry, Sulfur, Iron, Carbon, Trace metals, Dysoxia, Euxinia, Cone-in-cone calcite, Taphonomy

EXPLORING LOW-OXYGEN CONDITIONS IN THE CAMBRIAN THROUGH TRILOBITES OF THE WHEELER SHALE

by

DOUGLAS L. JOHN

B.S., The University of California at Riverside, 2004

M.S., The University of California at Riverside, 2008

A Dissertation submitted to the Graduate Faculty of the University of Georgia

In Partial Fulfillment of the Requirements for the Degree

DOCTOR OF PHILOSOPHY

ATHENS, GEORGIA

2016

EXPLORING LOW-OXYGEN CONDITIONS IN THE CAMBRIAN

THROUGH TRILOBITES OF THE WHEELER SHALE

By

DOUGLAS L. JOHN

Major Professor:	Sally Walker
Committee:	Patricia Medeiros Doug Crowe Paul Schroeder Alberto Perez-Huerta

Electronic Version Approved:

Suzanne Barbour
Dean of the Graduate School
The University of Georgia
May 2016

DEDICATION

To my wife Laura, whose love and support have kept me going through many a long and stressful night of research and writing. Without her, this dissertation may never have come to be.

And to my parents, for all their support throughout my educational career. It brings me great satisfaction to know that I've done something worthy of the pride they already feel for me.

ACKNOWLEDGEMENTS

I first thank my advisor, Sally Walker, for her endless support, encouragement, and advisement throughout these studies. I extend my appreciation to the members of my committee and the other faculty at the UGA Department of Geology for all their input during this research project.

I also thank S. Holland for his advice on NMDS and H. D. Sheets for his advice on k-means cluster analysis. West Desert Collectors and Jennifer Smith of Terra Trilobites of Delta, UT provided assistance in acquiring samples and maintaining safe handling protocols. Vancouver Petrographics of Vancouver, British Columbia prepared thin sections. P. Medeiros and L. Babcock-Adams assisted with sample preparation and biomarker analyses with GC-MS. The expertise of C. Fleisher and E. Formo in performing the microprobe and ESEM analyses, respectively, is greatly appreciated. Steve Bates at the Lyons Geochemistry Lab, University of California, Riverside, provided training and assistance with geochemical analyses.

Funding for this research was provided by the Geological Society of America, the Society for Sedimentary Geology (SEPM), the Watts-Wheeler Fund, and the National Science Foundation (OCE-1057683).

TABLE OF CONTENTS

Page

APPENDICES…

CHAPTER 1

INTRODUCTION

The Wheeler Shale of Utah contains one of the most well-known occurrences of Cambrian (507 Ma) trilobites from North America. These trilobites are exceptionally well-preserved, and unusually preserved in that they commonly occur with encrustations of cone-in-cone calcite (CIC) up to several mm in thickness armoring their ventral surfaces. Because of this unusual preservation, and because of their similarities to the famous and roughly contemporaneous Burgess Shale, the Wheeler Shale has been well studied; however, though over a century of scientific examination yielded a wealth of data on the Wheeler Shale, much of it only raised further questions about the unique conditions that generated the preservation of fossils discovered there.

The Wheeler Shale represents a mixed siliciclastic-carbonate environment, restricted within a trough-bound basin in a shallow epeiric sea (Rees, 1986). The fossils of the Wheeler Shale fall into three assemblages: a soft-bodied assemblage associated with finely laminar sediments, thought to represent anoxic benthic conditions; a low-diversity, high-abundance assemblage dominated by the ptychopariid trilobite *Elrathia kingii* and species of the agnostid *Peronopsis*, associated with weakly laminar sediments and thought to represent dysoxic conditions, and a more diverse benthic trilobite assemblage associated with bioturbated sediments, interpreted as fully oxic conditions (Gaines et al., 2005; Brett et al. 2009).

The unusual occurrence of *Elrathia* in these low-diversity assemblages, with only the planktonic *Peronopsis* co-occurring, has been the focus of much attention: Gaines and Droser (2003) interpreted them as low-oxygen specialists, the first benthic colonists following the leading edge of the oxycline as it fell, based on the low-diversity, high-abundance assemblages characteristic of modern animals with that mode of life, and on the lack of pervasively bioturbated sediments where they were found. Gaines and Droser (2003) also drew a parallel between *Elrathia* and the olenids of Fortey (2000), who suggested that these trilobites were adapted for dysoxic or euxinic conditions through symbiosis with sulfur-oxidizing bacteria. This hypothesis was based on the idea that an olenimorph body plan – wide, flat, with numerous thoracic segments for harboring symbionts, and a simple feeding structure – were particularly well-suited for such a mode of life.

While the idea of symbiotic trilobites living in extreme environments is enticing, there remains work to be done to ascertain if these conditions actually existed, and whether trilobites actually carried out a symbiotic mode of life. Existing studies have examined the ecology, sedimentology, and ichnofabric of the Wheeler Shale (Gaines and Droser, 2003; Gaines et al., 2005; Brett et al., 2009), but aspects of the geochemistry remain unexamined that could directly address the question of benthic oxygenation. The question of symbiosis in trilobites, based thus far on morphology and occurrence, also can be more rigorously examined, and direct evidence for symbiosis could be identified.

This study addresses these outstanding questions in four parts. In the first part, I compare the characteristic morphology of putatively symbiotic trilobites with a group of their contemporaries representing the broader range of Cambrian trilobite morphologies.

If symbiotic trilobites possessed a morphology uniquely suited for symbiosis, then they should be morphologically distinct from the greater group of Cambrian trilobites, who represented a great diversity of disparate life habits governing their own morphologies.

In the second part, I search for direct evidence of sulfur-oxidizing bacterial symbionts through molecular biomarkers. If *Elrathia* had a symbiotic mode of life, then biomarkers characteristic of those sulfur-oxidizing bacteria may be detected in association with trilobite fossils.

In the third part, I compare the petrology and geochemistry of exoskeletal calcite of *Elrathia* and *Peronopsis*. The presence of abundant cone-in-cone calcite in association with exoskeletal calcite presents an opportunity to potentially compare geochemical proxies representing seawater and porewater conditions. If *Elrathia* was living in low-oxygen benthic conditions, and their skeletons still contain original calcite, then their exoskeletons should bear a distinct geochemical signal from the oxic *Peronopsis*, and from the later diagenetic calcites that formed in the sulfur-reduction zone necessary for the formation of cone-in-cone structures. If both exoskeletons are similar to the diagenetic calcites, then that suggests original exoskeletal calcite has been recrystallized during diagenesis and reflects porewater conditions.

In the fourth part, I compare sulfur, iron, and trace metal proxies from the sediment, to determine whether conditions on the seafloor were oxic, dysoxic, or euxinic, and how extensive anoxia or euxinia was in the underlying sediments. If the seafloor was not severely limited in oxygen, then some other factor than oxygenation may have been driving the abundance patterns described in the Wheeler Shale. If the subsurface did not

have extensive bacterial sulfate reduction, then rapid formation of CIC could not have occurred quickly after burial.

CHAPTER 2

TESTING SYMBIOTIC MORPHOLOGY IN TRILOBITES UNDER DYSOXIC AND OXIC CONDITIONS FROM CAMBRIAN TO EARLY ORDOVICIAN LAGERSTÄTTEN[1]

[1] John, D. L., and Walker, S. E. 2016. Testing symbiotic morphology in trilobites under dysoxic and oxic conditions from Cambrian to Early Ordovician Lagerstätten. Palaeogeography, Palaeoclimatology, Palaeoecology, 441, 704-720. Reprinted here with permission of publisher.

Abstract

Dysoxic conditions were prevalent in Cambrian and Early Ordovician oceans. Adaptations of trilobites to these conditions yield insight into the selective forces driving their evolution and the potential for modern arthropods to adapt to anthropogenically-driven dysoxia. In the early Paleozoic, olenid trilobites may have adapted to dysoxia through olenimorphy, special morphologic adaptations facilitating symbiosis with sulfur-oxidizing bacteria. Olenimorphy's link to symbiosis has never been tested and might instead be related to phylogeny. Here, we tested whether olenimorphy occurs predominately in dysoxic environments, as expected, or whether it occurs within certain trilobite groups regardless of environment. Trilobites were selected from nine fossil Lagerstätten representing the early-to-middle Cambrian prior to olenid evolution and the middle Cambrian-Early Ordovician Alum Shale with olenids, putative exemplars of symbiosis. Trilobite morphology was scored as ranked characters and reduced via non-metric multidimensional scaling (NMDS) to a single metric describing suitability for symbiosis. Results indicated that olenimorphy was significantly related to phylogeny and not environment. In the early-to-middle Cambrian, dysoxic corynexochids and oxic redlichiids were equally unsuitable for symbiosis, while ptychopariids from both oxic and dysoxic conditions were equally well-suited for symbiosis. In the Alum Shale, asaphids and ptychopariids from both oxic and dysoxic conditions were equally well-suited for symbiosis, and redlichiids from oxic conditions were poorly-suited. Olenids were not the best-suited trilobites within their data set, nor even within their order. Secular trends in thoracic segmentation did not bias our results. Trilobite hard parts do not appear to provide evidence for symbiosis, which is consistent with modern arthropods that have

few morphological adaptations for dysoxic conditions. In fact, arthropods are rare in persistently dysoxic conditions, raising concerns about the spread of anthropogenically-triggered benthic dysoxia in the future, particularly given the extinction of trilobites under similar conditions at the end of the Permian.

Introduction

Hypoxic conditions were prevalent in Cambrian and Early Ordovician oceans when higher global temperatures, lower atmospheric O2, higher CO2 and continental configurations contributed to stratified marine conditions in shallow shelf environments (Frakes et al., 1992; Berner, 2006; Gill et al., 2011; Xu et al., 2012). Persistently hypoxic conditions can lead to the development of dysoxia (critically low oxygen levels; < ~0.1 ml/l), as well as euxinia (low oxygen, free sulfate) where organic carbon input drives microbial sulfate reduction generating H2S from ubiquitous oceanic sulfate (Canfield, 1989; Feng et al., 2014). For benthic environments, euxinia is typically achieved whenever dysoxia persists beyond seasonal fluctuations and poor mixing generates a well-stratified chemocline below oxic surface waters (e.g., the Black Sea, Nägler, 2011; Slomp, 2013).

In modern oceans, persistently dysoxic environments such as oxygen minimum zones (OMZs) are characterized by benthos adapted for dysoxia through, among other factors, symbiosis with sulfur-oxidizing bacteria (Taylor and Glover, 2010). Dysoxic environments are also characterized by low-diversity, high-abundance metazoan assemblages (Levin et al., 2000). Modern benthic communities in persistently dysoxic environments are dominated by polychaete worms, nematodes and bivalve mollusks,

while arthropods are not common (Lu and Wu, 2000; Levin, 2003; Sellanes et al., 2010). In fact, modern arthropods show little tolerance for reduced oxygen conditions (Rabalais et al., 2002; Vaquer-Sunyer and Duarte, 2008), though some arthropods have morphological adaptations for high-sulfur conditions at hydrothermal vents such as increased surface area of the mouthparts for cultivation of thiotropic symbionts (Petersen et al., 2010).

It is curious, then, that at least some fossil arthropods – the trilobites – are associated with dysoxic environments (Speyer and Brett, 1986; Lehmann et al., 1995; Gaines and Droser, 2003). The mechanisms by which trilobites adapted to low-oxygen conditions can elucidate the selective forces driving trilobite evolution and also shed light on the potential for modern benthic arthropods to adapt to low oxygen levels that are predicted to occur in the Anthropocene.

One group of trilobites thought to have adapted for low-oxygen conditions are the late Cambrian to Ordovician olenids (Fortey and Owens, 1990). Fortey (2000) suggested they adapted to reduced oxygen through symbiosis with sulfur-oxidizing bacteria. He proposed a suite of morphological adaptations that would facilitate symbiosis, including reduction in exoskeletal and muscular robustness spurred by reduced feeding and predatory selective pressures, and a trend toward greater surface area under the exoskeleton that would facilitate symbiont cultivation. Trilobites bearing these morphologic characters, and thus similar to olenids, were termed olenimorphs (Fortey, 2000).

Fortey (2000) suggested that symbiosis, as indicated by olenimorph morphology, may not be limited to the olenids and might be widespread among trilobites. For example,

Fortey's morphological characters were used to suggest that the middle Cambrian ptychopariid *Elrathia kingii*, from the mostly dysoxic Wheeler Shale, was possibly symbiotic (Gaines and Droser, 2003). To date, Fortey's morphological characters have not been systematically tested to determine if they are indicative of symbiosis or are simply a phylogenetic legacy of certain trilobite groups.

Here, we tested whether symbiotic morphology meets the expectation that it occurs predominately in dysoxic environments or whether it occurs within particular trilobite groups regardless of environment. Trilobites from nine fossil Lagerstätten, representing the early Cambrian to Early Ordovician, were selected based on complete taxonomic and environmental (sedimentology, geochemistry) descriptions. Fortey's qualitative morphological characters (i.e., thoracic segments, carapace morphology, pleural morphology, hypostome attachment, and exoskeletal ornamentation) were converted into ranked quantitative characters and scored for each genus, forming a matrix. The matrix was then reduced via non-metric multidimensional scaling ordination (NMDS) to a single metric that adequately synthesized the individual characters. This metric described overall morphology for each trilobite as either well-suited for symbiosis, yielding high NMDS scores, or poorly-suited for symbiosis, yielding low NMDS scores. Two NMDS analyses were performed to examine the relationship of morphology with phylogeny (i.e., different taxonomic groups) and environment (i.e., oxic versus dysoxic). We first tested a set of early-to-middle Cambrian trilobites to describe the occurrence of Fortey's morphological characters prior to the evolution of olenids. One Ordovician olenid, *Hypermecaspis*, a trilobite that Fortey (2000) deemed to be symbiotic, was included to orient this analysis. Second, we tested a set of trilobites from the middle

Cambrian-Early Ordovician Alum Shale that included Fortey's (2000) original olenids. These trilobites represent a progression from an oxic, diverse assemblage in the middle Cambrian to a dysoxic, olenid-dominated assemblage in the late Cambrian-Early Ordovician.

A key issue that could affect our analyses is the fact that Cambrian trilobites had greater variability in their thoracic segments and more segments overall than in later periods (Hughes et al., 1999). Segmentation controls the number of gill structures, which in turn increases surface area for symbiotic cultivation (Fortey 2000). This one character could skew the NMDS scores of earlier trilobites artificially high, making them appear more suitable for symbiosis. Therefore, we also tested the effect of segmentation on both datasets to determine if segmentation was unduly affecting our analyses.

We predict that if Fortey's morphological characters collectively describe adaptations for symbiosis, then symbiotically-suitable trilobites (i.e., those with higher NMDS scores) should be more common in dysoxic assemblages. A symbiotic life mode allows for symbiotic trilobites to inhabit oxic waters, but not for oxic trilobites to inhabit dysoxic waters (after Gaines and Droser, 2003).

The difference in morphology between olenimorphic and non-olenimorphic trilobites should be even more pronounced in the later dataset (the Alum Shale) because olenimorphy represents more primitive character states. For example, olenimorphic trilobites have more segments, broad flat pleurae, unattached hypostome and a thin exoskeleton, which are primitive characters (Fortey and Owens, 1990; Fortey, 2000). Oxic trilobites should evolve away from these primitive character states given the absence of selective pressures to retain that morphology (i.e., dysoxia). Thus, trilobites

from later periods should show a more distinct difference between oxic and dysoxic morphologies, if olenimorphy is tied to symbiosis.

If the link between morphology and environment is confirmed, then symbiotic trilobites can be identified in other assemblages. If this link is not confirmed, then Fortey's characters have a strong phylogenetic component, indicating that members of a taxonomic group have similar morphologies regardless of environment.

Methods

Lagerstätten localities, assessment of relative oxygen levels and construction of datasets

We focused on fossil Lagerstätten that had well-preserved trilobites, complete taxonomic descriptions, and adequate geochemical or sedimentary data that could be binned into oxic and dysoxic environments. Both high and low diversity Lagerstätten (suggestive of oxic and dysoxic assemblages, respectively) were considered if well described.

Benthic conditions were not always persistently dysoxic, but could fluctuate between dysoxic and oxic as oxyclines rose and fell (Gaines and Droser, 2003). While some paleontological studies have discerned trilobite assemblages at bed-by-bed resolution (e.g., Speyer and Brett, 1986, Gaines and Droser, 2003), most others do not link trilobite occurrences with sedimentological or geochemical conditions at specific horizons. Thus, a faunal list for a given locality may represent an amalgamation of discrete oxic and dysoxic communities.

Because the majority of trilobites in our study could not be linked to specific geochemical horizons, it was necessary to make assumptions about habitat based on the

general character of the Lagerstätten in which they occurred. Therefore, Lagerstätten were classified as "mixed" or "mostly oxic" to describe their relative oxygen levels. "Mixed" Lagerstätten contained regular intervals of dysoxic conditions as identified by dark organic-rich sediment, sedimentary sulfide, lack of bioturbation, and/or monospecific fossil horizons. Mixed localities were not exclusively dysoxic and contained periodic oxic horizons, but can be generalized as more dysoxic relative to the other Lagerstätten. "Mostly oxic" localities contained irregular intervals of dysoxia, or had geochemical evidence that indicated that the water column was fully oxic above the sediment-water interface. Euxinia was impossible to definitively ascertain for all localities. An assumption was made that non-ephemeral periods of dysoxic deposition would be accompanied by some euxinia at or just below the sediment-water interface, which would allow sulfur-oxidizing bacterial symbionts to flourish.

Two datasets were constructed. The first dataset had trilobite taxa prior to olenid evolution, representing eight Lagerstätten spanning the early-to-middle Cambrian from sites worldwide (Fig. 2.1). Mostly oxic and mixed sites were each represented by four Lagerstätten (Table 2.1, Appendix 2.1). The second dataset was constructed from the Alum Shale Lagerstätte of Scandinavia, representing the middle Cambrian-Early Ordovician. This locality, cited as an excellent example for studying evolutionary processes (Clarkson and Taylor, 1995), contains the original olenids used to propose symbiotic morphology (Fortey, 2000), as well as co-occurring non-olenids. The Alum Shale has two distinct assemblages: a diverse middle Cambrian assemblage associated with mostly oxic conditions and a late Cambrian-Early Ordovician olenid-dominated

assemblage associated with mixed conditions (Clarkson and Taylor, 1995 ; Appendix 2.2).

Selecting and classifying trilobite genera

Trilobites were selected for which all morphological characters could be identified. The early-to-middle Cambrian dataset had 66 trilobite genera representing three trilobite orders: 15 corynexochids (22.7%), 14 redlichiids (21.2%), and 37 ptychopariids (56.1%) (Appendix 2.1; see *Symbiotic Character Matrix* for descriptions of morphological characters). The Ordovician olenid *Hypermecaspis*, an example from Fortey (2000) of a symbiotically well-suited olenimorph, was added to the early-to-middle Cambrian dataset to provide a point for comparison. Within the Alum Shale dataset, 24 genera were identified including six asaphids (25%), three redlichiids (12.5%), and 15 ptychopariids (62.5%), 11 of which were olenids (Appendix 2.2). Ptychopariida and Redlichiida are considered paraphyletic groups, and the relationship of the ptychopariids to post-Cambrian orders is not fully established (Lieberman and Karim, 2010). However, while widespread polyphyly has been suggested at the family level within the ptychopariids (Cotton, 2001), the distinction between ptychopariids and non-ptychopariids at the ordinal level is sufficient to recognize broad morphological differences.

Trilobite genera were classified by environment as belonging to mostly oxic or mixed sites (Table 2.1; Appendices 1-2). Because dysoxic trilobites could potentially inhabit oxic waters, while oxic trilobites could not inhabit dysoxic waters, a trilobite was considered “mixed” if it occurred within any mixed environment, or considered “mostly

oxic" if it occurred only within oxic environments. Within the early-to-middle Cambrian dataset, 32 genera were classified as belonging to mixed and 34 to mostly oxic environments, with *Hypermecaspis* also classified among the mixed trilobites. For the Alum Shale, eight genera were from the mostly oxic middle Cambrian and 16 spanned the mixed interval from the late Cambrian through the Early Ordovician.

The potential for under- and overrepresentation with respect to taxonomy (ptychopariids versus non-ptychopariids) and environmental type (mixed versus mostly oxic) was addressed for both datasets. No significant sample bias was detected in the early-to-middle Cambrian dataset (Pearson's chi-squared test: $\chi 2 = 0.926$, df = 1, and $p = 0.336$) or the Alum Shale dataset (Fisher's exact test: $p = 0.099$). R was used for all statistical tests (R Core Team, 2012), which were run at a significance level of $\alpha = 0.05$, except where otherwise stated.

Symbiotic character matrix

Fortey's characters

Fortey's (2000) descriptive characters for an ideal symbiotic trilobite include a broad, flat, thin exoskeleton with abundant thoracic appendages, which would provide a large surface area for symbiont cultivation. A symbiotic trilobite should also lack complex feeding structures such as a carnivorous hypostome, because nutrition was mostly derived from symbionts. Such a trilobite, like *Hypermecaspis*, would be considered well-suited for symbiosis, whereas a trilobite without these characteristics would be poorly-suited. Exoskeletal ornamentation was used as a substitute for carapace thickness, because thickness could not be readily determined from published descriptions.

Fortey argued that a thick cuticle would have an unnecessary metabolic cost for a symbiotic trilobite living in dysoxic conditions where predation was unlikely. Likewise, an ornate exoskeleton would be unnecessary.

Character matrix: Character state rankings and normalization

Fortey's descriptive characters were converted into five quantitative characters with ranked character states (Table 2.2), producing a character matrix for the 66 early-to-middle Cambrian genera plus *Hypermecaspis* and for the 24 Alum Shale genera. The morphological characters for generic descriptions were drawn from the Paleobiology Database (Landing et al., 2008) and the Treatise on Invertebrate Paleontology (Harrington, 1959; Whittington et al., 1997). Genera for which all characters could not be determined were not used in either dataset. All ranked character state values were normalized to fall between 0 (least suitable for symbiosis) and 1 (most suitable), so that all characters were equally weighted, as some characters were binary and others ternary. A trilobite with character state values closer to 1 matched Fortey's description for symbiosis and has high symbiotic suitability, while a trilobite with character state values closer to 0 does not, and has low symbiotic suitability. For example, *Hypermecaspis* would have character state values of 1, indicating high suitability (Appendices 1-2).

NMDS analyses

NMDS for early-to-middle Cambrian and Alum Shale trilobites

The character matrix quantitatively describes the variation in morphology among Fortey's five characters across five dimensions. To simplify the character matrix to a

single dimension that describes overall symbiotic suitability for each trilobite, non-metric multidimensional scaling (NMDS) was performed using Euclidean distance and the metaMDS function of the R vegan library (Oksanen et al., 2013). As the data were equally weighted for each character, Euclidean distance was an appropriate distance measurement and should provide similar results to dissimilarity matrices such as Bray-Curtis, which are less conservative as they do not satisfy triangle inequality (Anderson, 2006).

Twenty random starts were used to find the solution with the minimum stress. Stress decreases substantially from one to two dimensions, and yields an acceptable level of stress (Fig. 2.2; level of stress < 0.20; Rohlf 1970; Eallonardo and Leopold, 2014). Therefore, a two-dimensional NMDS analysis was used to best reduce the data without compromising its structure. The NMDS analysis generates an ordinated model that describes the patterns within the dataset, and produces a metric that can be tested using quantitative statistical methods. Comparison of these morphological data to independent observations such as environmental and phylogenetic data can yield information about the extrinsic factors potentially controlling morphology .

The major axis of the NMDS analysis (NMDS1) describes the majority of variation within character state values, because variability in NMDS scores was greatest along NMDS1 for both the early-to-middle Cambrian and Alum Shale datasets. If a common factor such as phylogeny or environment is controlling suitability, NMDS1 scores would be a proxy for that factor's effect. More positive NMDS1 scores indicate trilobites more well-suited for symbiosis and more negative scores indicate trilobites poorly-suited for symbiosis. For the early-to-middle Cambrian dataset, *Hypermecaspis*

should score high on NMDS1 and confirm that higher scores correspond to more symbiotically-suitable morphologies. Likewise, *Elrathia kingii*, previously described as potentially symbiotic, should also have high NMDS1 scores. Conversely, the redlichiid *Olenellus*, whose spinose, tapering thorax and well-developed mouthparts would be particularly maladapted for symbiotic cultivation and feeding, respectively, should score low on NMDS1. For the Alum Shale, the olenids should score high on NMDS1. These expectations would confirm the general effectiveness of NMDS for describing symbiotic morphology.

Test for independence of characters in NMDS1 for early-to-middle Cambrian trilobites

Because symbiosis could affect all characters equally, if any character was more strongly related to another character than to the NMDS axis, that would suggest those characters were not sufficiently independent, and are describing much of the same variation in the data, thus over-representing that variation. Therefore, a Spearman's rank correlation test was performed on each pairwise combination of characters and between each character and NMDS1. Three of the ten pairwise relationships in the early-to-middle Cambrian showed a significant correlation: segments with hypostome attachment and exoskeletal ornamentation with both pleural morphology and hypostome attachment. However, none of those relationships was stronger than the characters' relationships to NMDS1 (Table 2.3), and all characters were retained in the analysis.

If only some of the characters were influenced by environment, that might suggest that those characters were being controlled by an environmental parameter other than symbiosis. To test the strength of the relationship of each ranked character to

environmental conditions (mostly oxic or mixed), a Kruskal-Wallis rank-sum test was performed for each character, and no significant relationships were found in the early-to-middle Cambrian dataset, indicating none of the characters were strongly associated with mostly oxic or mixed environments (Table 2.3).

Test for independence of characters in NMDS1 for Alum Shale trilobites

Similar to the early-to-middle Cambrian trilobites, pairwise relationships between each character and between characters and NMDS1 were tested for the Alum Shale trilobites using a Spearman's rank correlation test. Within the Alum Shale, the only significantly related characters were hypostome attachment and segmentation (Spearman's rho = -0.490, $p = 0.02$), and the only character not significantly correlated to NMDS1 was segmentation (Table 2.3). Segmentation appears to be an anomalous character in the Alum Shale, possibly driven by a trend in trilobites beginning in the late Cambrian towards an overall reduction in number of segments; however, segmentation does not appear to be introducing any significant bias on the overall NMDS analysis, and thus was retained (see *Testing for segmentation bias*). All other characters were more strongly correlated with NMDS1 than with any other character, indicating they were adequately described by NMDS1. Exoskeletal ornamentation was not tested because all trilobites in the Alum Shale had only one state, unornamented.

A Kruskal-Wallis rank-sum test revealed that hypostome attachment was significantly related to environment (Table 2.3). This is likely because only redlichiids had a conterminant hypostome, and redlichiids were exclusive to mostly oxic environments. Because the control on hypostome attachment appears to be phylogenetic,

and because phylogeny is relevant to the analysis, hypostome attachment was retained in the Alum Shale analysis.

Identifying morphologically distinct groups in NMDS

Plots of NMDS1 scores for all trilobites were generated for each of the five characters. The score for each genus on NMDS1 and NMDS2 was given as a point. Each genus was plotted with a symbol that corresponded to its character state and centroids for each character were indicated with larger bold black symbols. The overall significant correlation of character states to NMDS1 suggest that scores would be expected to adequately express any patterns that might have existed within both datasets.

Because NMDS describes relative differences in morphology, any group of morphologically distinct trilobites (such as symbiotic trilobites) should generate distinct NMDS scores and plot similarly. To identify groups, k-means cluster analyses were performed on NMDS scores for both datasets. The clusters were identified using 20 random starts of up to 100 iterations each. If clusters were identified, the utility of those clusters for identifying distinct groups of symbiotically suitable trilobites was tested against NMDS1 scores using one-sample *t*-tests. The 95% confidence intervals (95% CIs) generated by the *t*-tests were used to define upper and lower NMDS1 thresholds, with trilobites scoring above the upper threshold considered “moderately-suited" for symbiosis. If any trilobites were identified as moderately-suited, another one-sample *t*-test was done on that new group to identify trilobites scoring above that group’s 95% CI, and those trilobites were considered “well-suited” for symbiosis. Because the data were repartitioned for this second *t*-test, a new alpha level was used ($\alpha = 0.025$) based on a

Bonferroni correction for multiple comparisons. Any cluster that contained entirely well-suited trilobites was examined to determine if its members were from solely mixed environments. If the trilobites were morphologically well-suited, but came from both mostly oxic and mixed environments, then that would suggest they are not symbiotic, because symbiosis is an adaptation specifically for low-oxygen conditions.

Testing for environmental and phylogenetic effects

Plots of overall NMDS1 scores for mostly oxic and mixed trilobite genera were generated to examine whether trilobites from mixed localities had higher symbiotic suitability. If NMDS1 describes suitability for symbiosis under more dysoxic conditions, then trilobites from mixed localities should exhibit a higher average suitability than those from mostly oxic localities. A two-sample *t*-test with a Welch correction was performed to determine if the two environmental types were significantly different from each other. The size of each sample (n = 34 mostly oxic, n = 33 mixed for early-to-middle Cambrian trilobites; n = 8 mostly oxic, n = 16 mixed for Alum Shale trilobites) was sufficient for a *t*-test (valid for $n \geq 5$, de Winter, 2013). A non-parametric Wilcoxon rank sum test was also performed, which confirmed the *t*-test results.

To assess whether there was any difference between mostly oxic and mixed environments within each taxonomic order, NMDS scores for each trilobite order were plotted separately, distinguishing between mixed and mostly oxic members. If mixed trilobites had significantly higher NMDS1 scores than mostly oxic trilobites within any one order, that might suggest symbiosis occurs only within that order. To gauge the difference between mostly oxic and mixed members within each trilobite order, the

frequency distributions and average values of NMDS1 scores were plotted for genera from each environment. The significance of those differences was assessed using a two-sample *t*-test with a Welch correction and checked with a non-parametric Wilcoxon rank-sum test. If the results from both tests were the same, only the *t*-test results were reported, but if sample size was < 5, then Wilcoxon results were reported.

To test if phylogeny influenced NMDS scores, NMDS plots were generated for each taxonomic order. If phylogeny is the main control on morphology, then NMDS scores should be closer within each taxonomic order and farther apart between orders.

Testing for segmentation bias

Thoracic segmentation was more numerous and more variable in the early evolution of trilobites (Hughes et al., 1999). Therefore, the number of segments for early and middle Cambrian trilobites is expected to be greater than in later trilobites, potentially inflating NMDS1 scores for the earlier groups and thereby potentially increasing the number of seemingly symbiotic trilobites. Conversely, a reduction in segments could skew the Alum Shale toward deflated NMDS1 scores and a decrease in the apparent symbiotic suitability of later trilobites. We therefore did two tests to determine if segmentation affected our analyses.

First, to determine if our data were affected by changes in the number of thoracic segments, the mean and standard deviation for segment number was determined for each taxonomic order from each of the three time periods (i.e., early Cambrian, middle Cambrian, and late Cambrian-Early Ordovician) and for the combined assemblage from each time period. If there was a trend towards reduced numbers of segments and reduced

variability in the number of segments, then the mean and standard deviations for the number of segments should be lower by the late Cambrian-Early Ordovician. If such a trend occurs, then its effects may be imparting a bias on the NMDS analyses for both datasets. To determine the trend in segmentation for all trilobites across the three time periods and test its significance, a generalized linear model (GLM) was fitted between segmentation and time.

Second, to test how thoracic segmentation affected NMDS1 scores, the two datasets were reduced in NMDS again without thoracic segmentation to generate a second set of NMDS scores. The net shift in NMDS1 scores between the first and second set of scores represents the overall direction of change, either positive or negative. This was calculated in R as the sum of all positive and negative shifts in NMDS1 scores (i.e., NMDS1 scores without segmentation minus NMDS1 with segmentation for all genera in each dataset). For the early-to-middle Cambrian dataset, if trilobites have more segments overall and this is inflating NMDS scores, then removing segmentation should drive overall NMDS1 scores lower. For the late Cambrian-Early Ordovician trilobites of the Alum Shale, with putatively fewer segments, segmentation could potentially be deflating NMDS scores. If so, removing segmentation should make NMDS1 scores increase for the Alum Shale. The overall amount of change was determined through the mean absolute shift in NMDS1 scores. This was calculated in R as the mean of the absolute difference in NMDS scores for all genera in each dataset before and after segmentation was removed from the analysis. A stronger effect of segmentation on NMDS scores would generate larger shifts in both directions when segmentation was removed. If a secular reduction in segmentation is biasing the analysis, then the effect of segmentation should be weaker in

the later Alum Shale dataset, when variability in segmentation is reduced and less of the variation explained by NMDS is due to differences in segmentation. The significance of the average change before and after removing segmentation was determined using a two-sample *t*-test. If the distributions were not significantly different, this would suggest that segmentation was not significantly biasing the analyses and that the NMDS analyses were robust against any trend in segmentation.

Results

NMDS for early-to-middle Cambrian trilobites

Characters and morphologically-distinct groups generated by NMDS

In general, all five characters in the early-to-middle Cambrian trilobites became monotonically more suitable along NMDS1 as scores increased (Fig. 2.3, refer to centroids), indicating that all characters were adequately represented by NMDS1. The number of thoracic segments increased from the least-suitable state to the most-suitable state as scores increased (Fig. 2.3A). Carapace morphology also became more suitable with greater NMDS1 scores, though arched and flat character states scored similarly (Fig. 2.3B). Pleural morphology (Fig. 2.3C), hypostome attachment (Fig. 2.3D) and exoskeletal ornamentation (Fig. 2.3E) also increased in suitability with increased NMDS1 scores. The variations within each character along NMDS1 were all greater than along NMDS2, indicating NMDS1 explained the majority of variation for each character. Although possible, no individual character was described more strongly on NMDS2 than on NMDS1.

NMDS1 scores met expectations for symbiotic suitability (Fig. 2.4). The two previously proposed symbiotic trilobites *Hypermecaspis* and *Elrathia* scored high (0.777) and moderately high (0.535) on NMDS1, respectively, while the spiny, tapering and carnivorous redlichiid *Olenellus* scored much lower (-1.202).

Six clusters were identified by k-means cluster analysis for early-to-middle Cambrian trilobites (Fig. 2.5). Three clusters represented trilobites with attached hypostomes, having relatively low NMDS1 scores ≤ 0.034, and three clusters contained trilobites with non-attached hypostomes, having, in general, higher NMDS1 scores ≥ -0.148. All but two genera in the low-scoring clusters were corynexochids and redlichiids, while all but three genera in the higher-scoring clusters were ptychopariids. The ptychopariid-dominated clusters correspond closely (but not perfectly) with differences in pleural morphology. These were segregated along NMDS2 by flat pleurae in the uppermost cluster and arched pleurae in the central cluster, with the lowermost cluster containing all the arched and spiny pleurae genera along with two arched pleurae.

A one-sample *t*-test indicated that NMDS1 scores ≥ 0.490 fall in the uppermost 5% of all ptychopariids ($t = 9.63$, df = 37, $\alpha = 0.05$, upper 95% CI = 0.490), which include genera from the two highest-scoring k-means clusters on NMDS1 (Fig. 2.5). The uppermost 5% group contained 17 genera, all ptychopariids, including *Elrathia* and *Hypermecaspis* (refer to Appendix 2.1 for NMDS1 scores). Ten genera were from mostly oxic environments and eight from mixed. These trilobites could be considered moderately suited for symbiosis. Within this moderately-suited group, 95% CIs generated by a *t*-test identified a very high scoring group with NMDS1 ≥ 0.673 ($t = 24.49$, df = 17, $\alpha = 0.025$). Trilobites in this group all belong to the uppermost cluster from the k-means analysis.

This group contained six genera including *Hypermecaspis* and could be considered well-suited for symbiosis. If these ptychopariids occur within mixed environments, they meet all expectations to be symbiotic. However, one of the five (i.e., *Germaropyge*) comes from a mostly oxic locality; the other four from mixed. Segmentation bias could affect the outcome of this early-to-middle Cambrian NMDS analysis, which we address in

Testing for segmentation bias in both datasets.

Environmental tests

Early-to-middle Cambrian trilobites were from an even mix of mostly oxic and mixed environments, with centroids for both groups around zero on NMDS1 (Fig. 2.6A). Both environmental groups were not significantly different from each other (t = 0.736, df = 63.901, p = 0.465). Ptychopariids were evenly distributed between mostly oxic and mixed assemblages with their centroids near 0.5 (Fig. 2.6B), and those environmental groups were not significantly different from each other (t = 0.335, df = 29.123, p = 0.740). In contrast to ptychopariids, corynexochids and redlichiids were more environment-specific and lower scoring. Most corynexochids were from mixed localities. Corynexochids from mixed environments had a centroid near -0.5 that was lower than the mostly oxic corynexochids with a centroid near zero. This was counter to expectations that trilobites from mixed environments should have higher NMDS1 scores if environment is controlling morphology (Fig. 2.6C). Importantly, corynexochid NMDS1 scores were not significantly different between environment groups (W = 5; p = 0.126). In contrast to corynexochids, redlichiids occurred chiefly in mostly oxic localities. Their NMDS1 scores for mostly oxic members were low, as expected, though scores for the

few mixed members were also low, with centroids both near -0.5 (Fig. 2.6D), and were not significantly different (W = 3.5, $p = 0.216$).

Phylogenetic tests

There is a strong phylogenetic signal on NMDS1 scores for ptychopariid and non-ptychopariid trilobites. All but three ptychopariid trilobites had positive NMDS1 scores, while all but two each of corynexochids and redlichiids had negative scores (Fig. 2.7A). NMDS1 scores for ptychopariids varied from slightly below average (i.e., zero) to relatively high (Fig. 2.7B). Corynexochids and redlichiids scored lower than ptychopariids, having very low to slightly above average NMDS1 scores (Fig. 2.7C-D). Ptychopariid NMDS1 scores were significantly different from corynexochids ($t = -6.416$, df = 16.846, $p < 0.0001$) and redlichiids ($t = 7.3545$, df = 16.005, $p < 0.0001$), indicating ptychopariids were morphologically distinct from non-ptychopariids. However, there was no significant difference between NMDS1 scores for corynexochids and redlichiids ($t = -0.411$, df = 26.984, $p = 0.684$), indicating that low NMDS1 scores were associated with non-ptychopariids in general.

NMDS for Alum Shale trilobites

Characters and morphologically-distinct groups generated by NMDS

For the Alum Shale trilobites, the five character states generally align uniformly with NMDS1 scores: while one character is anomalous, three increase monotonically with higher NMDS1 scores, and one has no comparative data (Fig. 2.8). Thoracic segmentation did not increase monotonically, with a high number of segments

corresponding to the lowest NMDS1 score (Fig. 2.8A). Only one trilobite, the middle Cambrian redlichiid *Paradoxides*, had a high number of thoracic segments, but it had a spiny, tapering body with an attached hypostome that contributed to its low NMDS1 score (-1.160). Removing *Paradoxides* from the NMDS analysis did not change the pattern for segmentation in the remaining genera, indicating that it is not biasing the rest of the data. Medium and low numbers of thoracic segments corresponded to scores with centroids both near zero and showing no unequivocal trend along NMDS1. Carapace morphology and pleural morphology increased in suitability along NMDS1 (Fig. 2.8B–C, respectively). Trilobites with attached hypostomes have more negative NMDS scores, while those with non-attached hypostomes have more positive scores, as expected (Fig. 2.8D).Only unornamented trilobites occurred in the Alum Shale (Fig. 2.8E).

A k-means cluster analysis identified six clusters in the Alum Shale trilobites (Fig. 2.9). Two of the clusters (the lowest-scoring, with NMDS1 ≤ -0.906, and a moderately-scoring cluster containing a single trilobite at NMDS = -0.298) contained the three redlichiids in the Alum Shale. Three clusters also scored moderately on NMDS1 (between -0.490 and 0.303) and contained a mix of ptychopariids and asaphids. The highest-scoring cluster (NMDS1 ≥ 0.610) contained two trilobites, the olenid ptychopariid *Parabolinella* and the asaphid *Anomocarina* (refer to Appendix 2.2). A one-sample *t*-test on all trilobites in the Alum Shale indicated that NMDS1 scores ≥ 0.188 fall above the upper 95% CI ($t = 0.057$, df = 23, $\alpha = 0.05$; Fig. 2.9). Based on morphology, these trilobites are moderately suited for symbiosis. Six asaphids and four ptychopariids fall within this group (Appendix 2.2), representing four mostly oxic and six mixed genera. This moderately-suited group includes the two highest-scoring clusters,

except for one genus that falls below the 95% CI, *Agraulos* (NMDS1 = 0.130). Another one-sample *t*-test on the moderately-suited group indicated that NMDS1 scores ≥ 0.362 identified by the upper 95% CI could be considered a group well-suited for symbiosis (t = 8.552, df = 9, α = 0.025). This group contained two trilobites, *Parabolinella* and *Anomocarina*, which correspond to the highest-scoring cluster. These trilobites represent mostly oxic (*Anomocarina*) and mixed (*Parabolinella*) environments within the Alum Shale, and therefore do not match expectations if symbiotic morphology is an adaptation for dysoxic environments.

Environmental tests

Environment does not appear to have a strong influence on NMDS1 scores in the Alum Shale. Trilobites from the middle Cambrian represent mostly oxic environments yet have the lowest and highest NMDS1 scores within the Alum Shale and a centroid slightly below zero (Fig. 2.10). The late Cambrian-Early Ordovician trilobites that represent chiefly mixed environments overlap with the middle Cambrian trilobites, and have moderately low to high NMDS1 scores with a centroid slightly above zero (Fig. 2.10). Importantly, centroids for mixed and mostly oxic genera were near zero and the environmental groups were not significantly different from each other based on NMDS1 scores (t = 0.601, df = 8.605, p = 0.563).

Environment also does not exert a strong control over individual taxonomic orders. NMDS1 centroids for mostly oxic and mixed ptychopariids were near zero and the environmental groups were not significantly different from each other (Fig. 2.11A; t = -1.870, df = 11.939, p = 0.086). The few mostly oxic ptychopariids actually had higher

NMDS1 scores than mixed ptychopariids, contrary to expectations (based on centroids, Fig. 2.11A). Within the ptychopariids, olenids represented mixed and non-olenids mostly oxic environments, with the exception of *Irvingella*, a non-olenid that co-occurred with olenids in mixed environments (Fig. 2.11A-B) . Olenids had slightly lower NMDS1 scores than non-olenids (based on centroids, Fig. 2.11B) and this was weakly significant (t = -2.233, df = 12.528, p = 0.045). Mixed and mostly oxic asaphids had centroids above zero, and the two environmental groups were not significantly different from each other (Fig. 2.11C; t = -1.750, df = 2.320, p = 0.205). Mostly oxic asaphids had higher NMDS1 scores than mixed, contrary to expectations (based on centroids, Fig. 2.11C). Conversely, redlichiids occurred entirely within the mostly oxic interval of the Alum Shale, and scored low, as expected (based on centroid, Fig. 2.11D). Olenids, the exemplars for olenimorphy, should be among the best-fit for symbiosis within ptychopariids and all other trilobites, yet they surprisingly scored lower than non-olenid ptychopariids and asaphids.

Phylogenetic tests

Phylogeny has a strong signal on NMDS1 scores in the Alum Shale. Three orders (Ptychopariida, Asaphida, and Redlichiida) are represented, with redlichiids scoring low, and asaphids and ptychopariids scoring generally at or above zero (based on centroids; Fig. 2.12A). Within taxonomic groups, frequencies of NMDS1 scores for ptychopariids score near average (i.e., zero; Fig. 2.12B). Asaphids scored slightly higher than average (Fig. 2.12C), while redlichiids scored much lower than average (Fig. 2.12D). Ptychopariids and asaphids are distinct from redlichiids, though not from each other.

Based on NMDS1 scores, ptychopariids were not significantly different from asaphids ($W = 28.5$, $p = 0.212$), but were significantly different from redlichiids ($W = 43$, $p = 0.018$). Asaphids also had a significantly different distribution than redlichiids ($W = 0$, $p = 0.028$).

Testing for segmentation bias in both datasets

Overall, there was little variation in the number of segments over time for both datasets combined, with a mean of 12.38 segments in the early Cambrian, 12.37 segments in the middle Cambrian, and 10.88 segments for the late Cambrian-Early Ordovician (Table 2.4). The net change in the number of segments between the early Cambrian and late Cambrian-Early Ordovician trilobites was 1.5 segments. However, standard deviations increase from the early Cambrian to middle Cambrian, indicating increased variability in segment number. This could be related to the higher taxonomic diversity in the middle Cambrian datasets, where all four orders are represented. By the late Cambrian-Early Ordovician, the total mean and standard deviation for the number of segments was slightly lower than in the early Cambrian (Table 2.4).

Within groups, there was also little difference in the number of segments between time periods (Table 2.4). Only three groups (i.e., the ptychopariids, redlichiids, and asaphids) appear in more than one time period across both datasets to make meaningful comparisons for trends in thoracic segmentation. Mean thoracic segmentation in ptychopariids increased slightly from the early Cambrian (12.67) to the middle Cambrian (13.83) and then decreased in late Cambrian-Early Ordovician (11.50). The standard deviation for number of thoracic segments in ptychopariids rises from the early Cambrian

(2.52) to middle Cambrian (4.12), but then falls back to slightly below early Cambrian levels in the late Cambrian-Early Ordovician (2.15). It appears that ptychopariids have more variability in segment number in the middle Cambrian than other periods. In contrast to ptychopariids, mean segmentation for redlichiids increases from the early Cambrian (12.30) to middle Cambrian (16.43), but standard deviations remain roughly similar (Table 2.4). Asaphid mean segmentation is nearly the same from the middle Cambrian (10.00) to the late Cambrian-Early Ordovician (9.00), with little variability (Table 2.4). A GLM for overall trilobite segmentation through time found a slightly decreasing trend in segmentation (-0.081), but this trend was not significant (df = 85, p = 0.126). Therefore, it appears that segmentation does not vary through time in a way that would bias the results of the NMDS analyses.

Additionally, if thoracic segmentation was biasing the analyses, then removing this character should have a significant effect on NMDS scores. However, when segmentation was removed from both the early-to-middle Cambrian and Alum Shale NMDS analyses, scores hardly changed (Fig. 2.13A-B; Appendix 2.3). In the early-to-middle Cambrian, the mean absolute shift in values was 0.038, and for the Alum Shale, 0.046, indicating that the individual effect of segmentation on NMDS scores was comparable in both datasets. The net shift in NMDS1 values was nearly zero for both, indicating that scores did not shift uniformly lower or higher when segmentation was removed, and thus scores were not inflated or deflated in either analysis. Further, NMDS1 scores generated before and after segmentation was removed from the analyses were not significantly different from each other (early-to-middle Cambrian: t = 0, df = 133, p = 1.000; Alum Shale: t = 0, df = 47, p = 1.000).

Discussion

Testing Fortey's symbiotic morphology using NMDS

Fortey (2000) suggested that olenimorphic trilobites had morphological adaptations that facilitated symbiosis with sulfur-oxidizing bacteria as a response to living in low-oxygen conditions. Dysoxic conditions were prevalent through the Cambrian and Early Ordovician period, which would have created dysoxic and euxinic conditions (herein referred to as mixed environments) for symbiotic trilobites to thrive within. We tested Fortey's morphological characters using NMDS to determine if symbiotic morphology was indicative of trilobites living in mixed environments or was a phylogenetic signal and not related to adaptation to environmental conditions. Character states that are indicative of symbiotic morphology in trilobites as described by Fortey (collectively referred to as olenimorphy) were synthesized into a single numerical metric, NMDS1, using data from two sets of trilobites, with and without olenids. Higher scores on NMDS1 would indicate overall greater symbiotic suitability: moderately high scores represent moderately-suited trilobites, while distinctly high scores represent well-suited trilobites.

We found that NMDS1 was a robust proxy that could describe overall suitability for symbiosis in trilobites. In the early-to-middle Cambrian, individual character suitability for symbiosis increased with higher values on NMDS1. The characters mostly varied independently of each other, and every character was more closely correlated to NMDS1 than to any other characters. This increase in suitability, however, does not mean that symbiosis is controlling the distribution along NMDS1, as we discuss below.

In the Alum Shale, three of the five characters increased with higher values on NMDS1. The two exceptions were exoskeletal ornamentation, which had only one state represented, and segmentation, which had no trend in either direction along NMDS1 except for one outlier, *Paradoxides*, with a low NMDS1 score. However, the individual effects of segmentation on the Alum Shale were small (see discussion on *Segmentation*) and the inclusion of segmentation did not bias the analysis against the other characters. The remaining three characters in the Alum Shale had low pairwise correlations, and varied independently.

The independence of most characters in both datasets and their overall correlation with the NMDS1 metric suggested that there was a common factor connecting the characters that determined overall symbiotic suitability. Therefore, NMDS1 did not appear to be simply modeling statistical noise and random variation. NMDS1 scores, as a proxy for overall symbiotic suitability, were compared to environmental occurrence and phylogenetic affinity. This served to determine the relative effects of environment and phylogeny as common factors driving symbiotic morphology.

Identifying groups

Cluster and confidence interval analysis within both datasets failed to identify a clear group of trilobites from exclusively mixed environments with significantly higher NMDS1 scores, as would be expected if there was a population of morphologically-distinct symbiotic trilobites that tracked dysoxic conditions. In the early-to-middle Cambrian dataset, five high-NMDS1 scoring ptychopariids could potentially be symbiotic, but one of those five represented an oxic environment, suggesting that the

common factor governing their distinct morphology was not likely environmentally driven. Moderately-suited trilobites also represented a mix of mostly oxic and mixed environments in the early-to-middle Cambrian. In the Alum Shale, two well-suited trilobites were identified, an asaphid and a ptychopariid, but they represented mostly oxic and mixed environments, respectively. Moderately-suited trilobites in the Alum Shale were not exclusively dysoxic either.

Olenimorphy does not appear to describe a special adaptation for symbiosis. Symbiosis itself is a binary character: organisms either are symbiotic or are not, and morphologies dependent on symbiosis would be expected to show a binary pattern as well, which should be manifest in the NMDS1 scores for trilobites. The 95% CI analysis does not support this, with neither well-suited nor moderately-suited groups in either dataset showing a dominance of mixed genera. Overall symbiotic suitability appears continuous from "less olenimorphic" to "more olenimorphic", rather than showing a distinction between discrete "symbiotic" and "non-symbiotic" morphologies, which strongly indicates a phylogenetic influence, rather than an environmental adaptation, for so-called symbiotic morphology.

Environment

Environment did not appear to exert an influence on morphology at any point in the analyses. No individual character was significantly correlated to environmental conditions in both data sets, suggesting even before any NMDS results that an environmental control on morphology was unlikely. For the early-to-middle Cambrian, redlichiids from mostly oxic environments and corynexochids from mixed environments

scored similarly low on NMDS1, suggesting environment was not driving any difference in their morphologies, while ptychopariids representing both environments scored uniformly higher than the other orders. Redlichiids in the Alum Shale, represented by mostly oxic environments, scored low on NMDS1, as expected. However, asaphids and ptychopariids from mixed environments scored similarly to their counterparts in mostly oxic environments, counter to expectations. The lack of any distinct environmental gradient in NMDS1 scores indicates that environment (i.e., mostly oxic vs. mixed) is not a major factor driving changes in trilobite morphology.

The difference in morphology between oxic and dysoxic assemblages should increase through time, because the character states associated with olenimorphy are primitive states for those characters. Therefore, trilobites would evolve towards progressively more derived (i.e., less olenimorphic) character states, in the absence of a factor such as symbiosis favoring retention of the primitive states. However, no difference in NMDS1 scores between oxic and dysoxic assemblages was detected in either data set, suggesting symbiosis was not driving changes in morphology.

It is worth nothing that, in the absence of a single common factor (i.e., symbiosis) holistically controlling morphology, individual characters would be free to independently respond to environment. For example, having a wide thorax with numerous thoracic segments would increase gill surface area, thus improving suitability for dysoxic conditions even without symbiosis. However, other features associated with symbiotic morphology, such as a natant hypostome, would not affect dysoxic suitability. The lack of a strong pairwise correlation between any one character and environmental conditions indicates that environment is not a major factor governing morphology, even outside a

symbiotic hypothesis. This suggests that trilobite adaptive strategies for dysoxia did not have a strong morphological component.

Phylogeny

Phylogeny appears to be the primary factor that controlled morphology, not environmental pressure from dysoxic conditions. NMDS1 scores were primarily linked to phylogenetic affiliation, irrespective of environment. In the early-to-middle Cambrian, ptychopariids scored significantly higher than corynexochids and redlichiids on NMDS1, regardless of environment. Corynexochids and redlichiid NMDS1 scores were not significantly different from each other, despite strong environmental differences. In the Alum Shale, asaphids and ptychopariids scored significantly higher than redlichiids, but they were not significantly different from each other. Asaphids are descended from ptychopariids (Fortey and Chatterton, 1988), suggesting that their phylogenetic similarity is expressed in similar NMDS scores. In general, asaphids score higher than ptychopariids, and olenids in particular, despite occurring in mostly oxic and mixed intervals in the Alum Shale. The asaphids indicated that morphological characters interpreted as symbiotic (i.e., a broad flat thorax with flat, wide pleurae and numerous thoracic segments) can be expressed even more strongly in non-olenids than in the olenids themselves, including in trilobites from mostly oxic environments. While olenids (representing mixed environments) were distinct from non-olenid ptychopariids (representing mostly oxic environments), the non-olenid ptychopariids scored higher, contrary to expectations. Thus, it appears that olenimorphy is much more strongly related to phylogeny than environment.

Segmentation

The number of thoracic segments is one of the characters incorporated into NMDS1 scores. Because Lower Paleozoic trilobites have an evolutionary trend toward a decrease in thoracic segmentation over time, this character could bias our analyses and recognition of putatively symbiotic trilobites. Hughes et al. (1999) suggested that variability in segmentation was highest during the Cambrian, and then stabilized toward a decrease in average segmentation in later periods. Therefore, more symbiotically suitable trilobites could be identified in the early-to-middle Cambrian dataset than in the Alum Shale if this trend in the number of segments was affecting the outcome of our analyses. However, when trilobites from both datasets were compared to time, overall number and variability of thoracic segments did not show any trends, though ptychopariids did have higher variability in the number of thoracic segments in the middle Cambrian, in accordance with the findings of Hughes et al. (1999). The GLM likewise found only a small and non-significant decrease in segmentation through time.

Segmentation did not bias the outcome of the NMDS analyses. When segmentation was removed from both data sets, NMDS1 scores shifted minimally, but in no particular direction, and the shifts were not significant. Removal of segmentation did not shift NMDS1 scores lower in the early-to-middle Cambrian trilobites or higher for the Alum Shale trilobites, as expected if segmentation was artificially inflating or deflating NMDS1 scores. Therefore, segmentation did not have a disproportionately strong influence on overall NMDS scores in either dataset, which validates the inclusion of segmentation in the analyses.

Implications for modern arthropods

Based on our analyses, trilobites demonstrated low morphological response to environmental change, which raises the question of how modern arthropods might cope with the loss of suitable habitat as dysoxia potentially spreads in warming oceans. It is possible that trilobites adapted physiologically without major morphological change, which could explain why some trilobites are found in dysoxic conditions despite their morphological similarity to more oxic genera.

In modern icehouse oceans, dysoxia occurs intermittently with seasonal blooms of phytoplankton and eutrophication, or more permanently over nutrient-upwelling zones (Diaz, 2001). These dysoxic areas are limited in size, because robust deep-water circulation promotes thorough mixing of oxygenated waters (Toggweiler and Russell, 2008). Modern fauna have adapted to avoid dysoxic waters and to quickly recolonize the benthos after reoxygenation, rather than persevere through intermittent dysoxia (Lu and Wu, 2000). In contrast, hothouse dysoxic conditions, like those in the Cambrian, are larger and more prolonged because the circulation and solubility of oxygen in the oceans decreases with increased temperature (Slomp, 2013). In particular, fossil arthropods in persistently dysoxic conditions that were not able to migrate to more oxic waters went extinct (Williams et al., 2011). Arthropods appear inherently poorly-suited to adapt to persistent dysoxia. An increase in persistently dysoxic zones could occur over the next century, as global ocean circulation weakens and oxygen solubility decreases with rising global temperatures, which does not bode well for marine arthropods.

Such a prolonged change in oxygenation would represent a new challenge for modern arthropods. Symbiotic arthropods are not a major part of modern dysoxic

communities (Levin, 2003), making symbiosis an unlikely adaptation. Where they do occur, modern symbiotic arthropods do not significantly modify their hard parts. For example, chemosynthetically symbiotic shrimp at sulfur-rich vents only modify the internal surface of their mouthparts for cultivation of symbionts (Petersen et al., 2010), suggesting low morphological flexibility similar to trilobites. Furthermore, it is unlikely that trilobites shared symbiosis as a common behavior at the family level (i.e., olenids) or higher (i.e., olenimorphs). Where modern arthropod ectosymbiotic relationships do occur, they tend to occur at the generic level, with different symbiotic assemblages associated with different genera of hosts (Ott et al., 2004). The variety of symbiotic relationships suggests that symbiosis is a highly-derived evolutionary behavior tied to specific, and perhaps, extreme environments like deep-sea hydrothermal vents, and not deeply intrinsic to any group of arthropod. If symbiosis did occur, it may have been ectosymbiosis, which is not easy to identify purely from hard part morphology.

The lack of adaptive responses to dysoxia for arthropods, aside from migration, raises the possibility for significant faunal turnover in the Anthropocene. Arthropod species could become extirpated from growing dysoxic environments because they are unable to adapt, even under relatively mild dysoxia. An analogue for future oceans might be the final extinction of trilobites at the end-Permian, which has been associated with a global spread of persistent dysoxic to euxinic environments, linked at least partially to global warming (Bond and Wignall, 2010; Liao et al., 2010). Given the economic importance of many benthic arthropods as food stocks, and their ecological importance as predators and scavengers, this could lead to noticeable effects on human and environmental sustainability.

References

Anderson, M. J., 2006. Distance-based tests for homogeneity of multivariate dispersions. Biometrics, 62(1), 245-253.

Berner, R.A., 2006. GEOCARBSULF: A combined model for Phanerozoic atmospheric O_2 and CO_2. Geochimica et Cosmochimica Acta, 70, 5653-5664.

Bond, D.P., Wignall, P.B., 2010. Pyrite framboid study of marine Permian–Triassic boundary sections: a complex anoxic event and its relationship to contemporaneous mass extinction. Geological Society of America Bulletin, 122(7-8), 1265-1279.

Brett, C.E., Allison, P.A., DeSantis, M.K., Liddell, W.D., Kramer, A., 2009. Sequence stratigraphy, cyclic facies, and *lagerstätten* in the Middle Cambrian Wheeler and Marjum Formations, Great Basin, Utah. Palaeogeography, Palaeoclimatology, Palaeoecology, 277, 9-33.

Canfield, D.E. 1989. Sulfate reduction and oxic respiration in marine sediments: implications for organic carbon preservation in euxinic environments. Deep Sea Research Part A. Oceanographic Research Papers, 36(1), 121-138.

Caron, J., Jackson, D, 2008. Paleoecology of the Greater Phyllopod Bed community, Burgess Shale. Paleogeography, Paleoclimatology, Paleoecology, 258, 222-256.

Chlupac, I., Kordule, V., 2002. Arthropods of Burgess Shale type from the Middle Cambrian of Bohemia (Czech Republic). Bulletin of the Czech Geologic Survey, 77(3), 167-182.

Clarkson, E.N.K., Taylor, C. M., 1995. The lost world of the olenid trilobites. Geology Today, 11(4), 147-154.

Conway Morris, S., 1986. The community structure of the Middle Cambrian phyllopod bed (Burgess Shale). Paleontology, 29, 423-467.

Cotton, T.J., 2001. The phylogeny and systematics of blind Cambrian ptychoparioid trilobites. Palaeontology, 44(1), 167-207.

De Winter, J.C.F., 2013. Using the Student's *t*-test with extremely small sample sizes. Practical Assessment, Research & Evaluation, 18(10), 1-12.

Diaz, R.J., 2001. Overview of hypoxia around the world. Journal of Environmental Quality, 30(2), 275-281.

Eallonardo Jr., A.S., Leopold, D.J., 2014. Inland salt marshes of the northeastern United States: stress, disturbance, and compositional stability. Wetlands, 34(1), 155-166.

Fatka, O., Kordule, V., Szabad, M., 2004. Stratigraphical distribution of Cambrian fossils in the Pribram-Jince Basin (Barrandian area, Czech Republic). Senckenbergiana Lethaea, 84, 367-381.

Feng, L., Li, C., Huang, J., Chang, H., Chu, X., 2014. A sulfate control on marine mid-depth euxinia on the early Cambrian (ca. 529-521 Ma) Yangtze platform, South China. Precambrian Research, 246, 123-133.

Fortey, R., 2000. Olenid trilobites: The oldest known chemoautotrophic symbionts? Proceedings of the National Academy of Sciences, 97, 6574-6578.

Fortey, R. A. Chatterton, B. D. E., 1988. Classification of the Trilobite Suborder Asaphina. Palaeontology 31(1), 165-222.

Fortey, R., Owens, R.M., 1990. Trilobites. Pp. 121-142 *in* K.J. McNamara, ed. Evolutionary trends. University of Arizona Press, Tucson.

Frakes, L.A., Francis, J.E., Syktus, J.I., 1992. Climate modes of the Phanerozoic. Cambridge University Press, 288 pp.

Gaines, R.R., Droser, M. L., 2003. Paleoecology of the familiar trilobite *Elrathia kingii*: an early exaerobic zone inhabitant. Geology, 31, 941-944.

Gaines, R.R., Droser, M.L., 2010. The paleoredox setting of Burgess Shale-type deposits. Palaeogeography, Palaeoclimatology, Palaeoecology, 297, 649-661.

Garson, D.E., Gaines, R.R., Droser, M.L., Liddell, W.D., Sappenfield, A., 2012. Dynamic palaeoredox and exceptional preservation in the Cambrian Spence Shale of Utah. Lethaia, 45(2), 164-177.

Gehling, J.G., Jago, J.B., Paterson, J.R., García-Bellido, D.C., Edgecombe, G.D., 2011. The geological context of the lower Cambrian (Series 2) Emu Bay Shale Lagerstätte and adjacent stratigraphic units, Kangaroo Island, South Australia. Australian Journal of Earth Sciences, 58(3), 243-257.

Gill, B.C., Lyons, T.W., Young, S.A., Kump, L.R., Knoll, A.H., Saltzman, M.R., 2011. Geochemical evidence for widespread euxinia in the Later Cambrian ocean. Nature, 469, 80-83.

Harrington, H.J, 1959. Systematic Descriptions. Pp. O170-O590 *in* Part O – Arthropoda 1 of R.C. Moore, ed. Treatise on invertebrate paleontology. Geological Society of America, New York, and University of Kansas Press, Lawrence.

Hintze, L.F., and Robison, R.R., 1975. Middle Cambrian stratigraphy of the House, Wah Wah, and Adjacent Ranges in Western Utah. Geological Society of America Bulletin, 86, 881-891.

Hughes, N. C., Chapman, R. E., and Adrain, J. M., 1999, The stability of thoracic segmentation in trilobites: a case study in developmental and ecological constraints, Evolution & Development, 1(1):24-35.

Landing, E., Johnson, S.C., Geyer, G., 2008. Faunas and Cambrian volcanism on the Avalonian marginal platform, southern New Brunswick. Journal of Paleontology, 82(5), 884-905.

Lehmann, D., Brett, C.E., Cole, R., Baird, G., 1995. Distal sedimentation in a peripheral foreland basin: Ordovician black shales and associated flysch of the western Taconic foreland, New York State and Ontario. Geological Society of America Bulletin, 107, 708-724.

Levin, L.A., Gage, J.D., Martin, C., and Lamont, P.A., 2000. Macrobenthic community structure within and beneath the oxygen minimum zone, NW Arabian Sea. Deep Sea Research II, 47, 189-226.

Levin, L.A., 2003. Oxygen minimum zone benthos: adaptation and community response to hypoxia. Oceanic and Marine Biology: an Annual Review, 41, 1-45.

Liao, W., Wang, Y., Kershaw, S., Weng, Z., Yang, H., 2010. Shallow-marine dysoxia across the Permian–Triassic boundary: evidence from pyrite framboids in the microbialite in South China. Sedimentary Geology, 232(1), 77-83.

Lieberman, B. S., and Karim, T. S., 2010. Tracing the trilobite tree from the root to the tips: A model marriage of fossils and phylogeny. Arthropod Structure & Development, 39, 111-123.

Lu, L., Wu, R.S.S., 2000. An experimental study on recolonization and succession of marine macrobenthos in defaunated sediment. Marine Biology, 136, 291-302.

Nägler, T.F., Neubert, N., Böttcher, M.E., Dellwig, O., Schnetger, B., 2011. Molybdenum isotope fractionation in pelagic euxinia: Evidence from the modern Black and Baltic Seas. Chemical Geology, 289(1), 1-11.

Nedin, C., 1995. The Emu Bay Shale, a Lower Cambrian fossil Lagerstätte, Kangaroo Island, South Australia. Memoirs of the Association of Australian Palaeontologists, 18, 31-40.

Oksanen, J., Blanchet, F.G., Kindt, R., Legendre, P., Minchin, P.R., O'Hara, R.B., Simpson, G.L., Solymos, P., Stevens, M.H.H., Wagner, H., 2013. Vegan: Community Ecology Package, R package version 2.0-9. http://CRAN.R-project.org/package=vegan.

Ott, J., Bright, M., Bulgheresi, S., 2004. Marine microbial thiotrophic ectosymbioses. Oceanography and Marine Biology: An Annual Review, 42:95-118.

Palmer, A. R., Halley, R. B., 1979. Physical stratigraphy and trilobite biostratigraphy of the Carrara Formation (Lower and Middle Cambrian) in the southern Great Basin (No. 1047). US Govt. Printing Office.

Petersen, J.M., Ramette, A., Lott, C., Cambon-Bonavita, M.A., Zbinden, M., Dubilier, N., 2010. Dual symbiosis of the vent shrimp *Rimicaris exoculata* with filamentous gamma- and epsilonproteobacteria at four Mid-Atlantic Ridge hydrothermal vent fields. Environmental Microbiology, 12, 2204-2218.

R Core Team, 2012. R: A language and environment for statistical computing. R Foundation for Statistical Computing, Vienna, Austria, http://www.R-project.org/.

Rabalais, N.N., Turner, R.E., Wiseman, Jr., W.J., 2002. Gulf of Mexico Hypoxia, AKA "The Dead Zone". Annual Review of Ecology and Systematics, 33, 235-263.

Retallack, G., 2011. Exceptional fossil preservation during CO_2 greenhouse crises? Paleogeography, Paleoclimatology, Paleoecology, 307, 59-74.

Rohlf, F.J., 1970. Adaptive hierarchical clustering schemes. Systematic Zoology, 18, 58-82.

Sellanes, J., Neira, C., Quiroga, E.. Teixido, N., 2010. Diversity patterns along and across the Chilean margin: a continental slope encompassing oxygen gradients and methane seep benthic habitats. Marine Ecology, 31(1), 111-124.

Shu, D., Vannier, J., Luo, H., Chen, L., Zhang, X., Hu, S., 1999. Anatomy and lifestyle of Kunmingella (Arthropoda, Bradoriida) from the Chengjiang fossil Lagerstätte (lower Cambrian; southwest China). Lethaia, 32(4), 279-298.

Slomp, C.P., 2013. Reconstructing the history of euxinia in a coastal sea. Geology, 41, 523-524.

Speyer, S.E., Brett, C.E., 1986. Trilobite taphonomy and Middle Devonian taphofacies. Palaios, 1(3), 312-327.

Steiner, M., Zhu, M.Y., Weber, B., Geyer, G., 2001. The Lower Cambrian of eastern Yunnan: trilobite-based biostratigraphy and related faunas. Acta Palaeontologica Sinica, 40(suppl.), 63-79.

Taylor, J.D., Glover, E.A., 2010. Chemosymbiotic bivalves. Pp. 107-135, *in* The vent and seep biota. Springer Netherlands.

Toggweiler, J.R., Russell, J., 2008. Ocean circulation in a warming climate. Nature, 451(7176), 286-288.

Vaquer-Sunyer, R., Duarte, C.M., 2008. Thresholds of hypoxia for marine biodiversity. Proceedings of the National Academy of Sciences, 105, 15452-15457.

Webster, M., Sadler, P.M., Kooser, M.A., Fowler, E., 2008. Combining stratigraphic sections and museum collections to increase biostratigraphic resolution. Pp. 95-128 *in* P.J. Harries, ed. High-Resolution Approaches in Stratigraphic Paleontology. Springer Netherlands.

Whittington, H.B., Chatterton, B.D.E., Speyer, S.E., Fortey, R.A., Owens, R.M., Chang, W.T., Dean, W.T., Jell, P.A., Laurie, J.R., Palmer, A.R., Repina, L.N., Rushton, A.W.A., Shergold, J.H., Clarkson, E.N.K., Wilmot, N.V., Kelly, S.R.A., 1997. Part O, Revised. Arthropoda 1: Trilobita: Introduction, order Agnostida and order Redlichiida. *in* R.L. Kaesler, ed. Treatise on invertebrate paleontology. Geological Society of America, Boulder, Co., and University of Kansas Press, Lawrence, 530 pp.

Williams, M., Vannier, J., Corbari, L., Massabau, J.C., 2011. Oxygen as a driver of early arthropod micro-benthos evolution. PLoS ONE, 6(12), e28183.

Xu, L., Lehmann, B., Mao, J., Nägler, T.F., Neubert, N., Böttcher, M.E., Escher, P., 2012. Mo isotope and trace element patterns of Lower Cambrian black shales in South China: Multi-proxy constraints on the paleoenvironment. Chemical Geology, 318, 45-59.

Zhao, F., Caron, J.B., Hu, S., Zhu, M., 2009. Quantitative analysis of taphofacies and paleocommunities in the Early Cambrian Chengjiang Lagerstätte. Palaios, 24(12), 826-839.

Figures and Tables

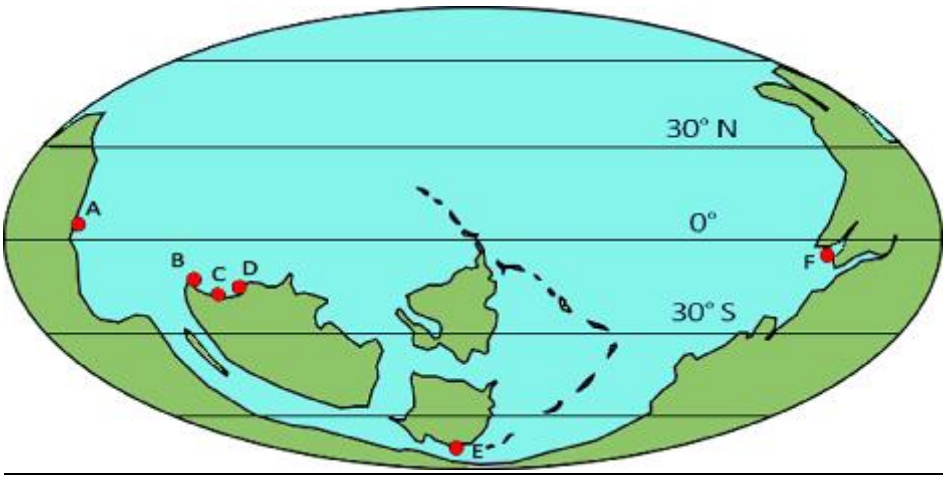

Fig. 2.1. Map of localities for Cambrian paleogeography. From west to east: A, Chengjiang. B, Latham and Spence Shales. C, Wheeler and Marjum Shales. D, Burgess Shale. E, Jince. F, Emu Bay. Map modified from Ron Blakey, NAU Geology, early Cambrian paleogeography.

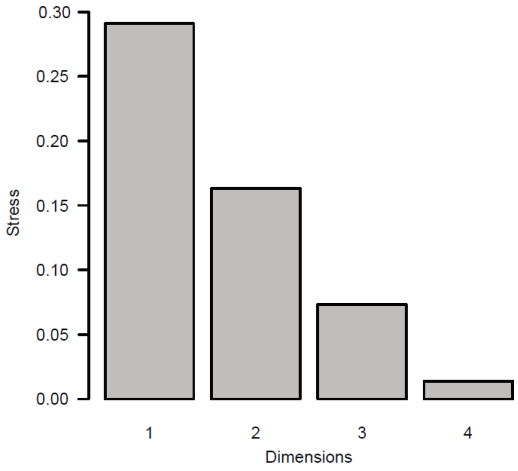

Fig. 2.2. Stress of NMDS model from one to four dimensions for the early-to-middle Cambrian dataset. A two-dimensional model best describes the variation in the character matrix (i.e., stress below 0.2) while minimizing dimensions. The model was iterated 20 times to achieve the best solution, but reached a minimum after ten.

Fig. 2.3. Results of NMDS for trilobites of the early-to-middle Cambrian, including *Hypermecaspis,* symbolically coded by character state. Centroids for each character state are coded with bold black symbols. Higher positive scores on NMDS1 correspond to greater symbiotic suitability. A, Character states for number of segments, with a trend toward higher number of segments asNMDS1 scores increase. B, Carapace morphology increases along with NMDS1 scores from highly arched through arched to flat morphologies. C, Pleural morphology, with a trend toward flatter pleurae with increased NMDS1 scores. D, Hypostome attachment has two distinct groupings: non-attached hypostomes correspond to higher NMDS1 scores, attached hypostomes to lower scores. E, Exoskeletal ornamentation has two groups, with ornamented trilobites scoring lower onNMDS1 than non-ornamented trilobites. Ornamented trilobites were the lowest-scoring on NMDS1 of all character-state groups.

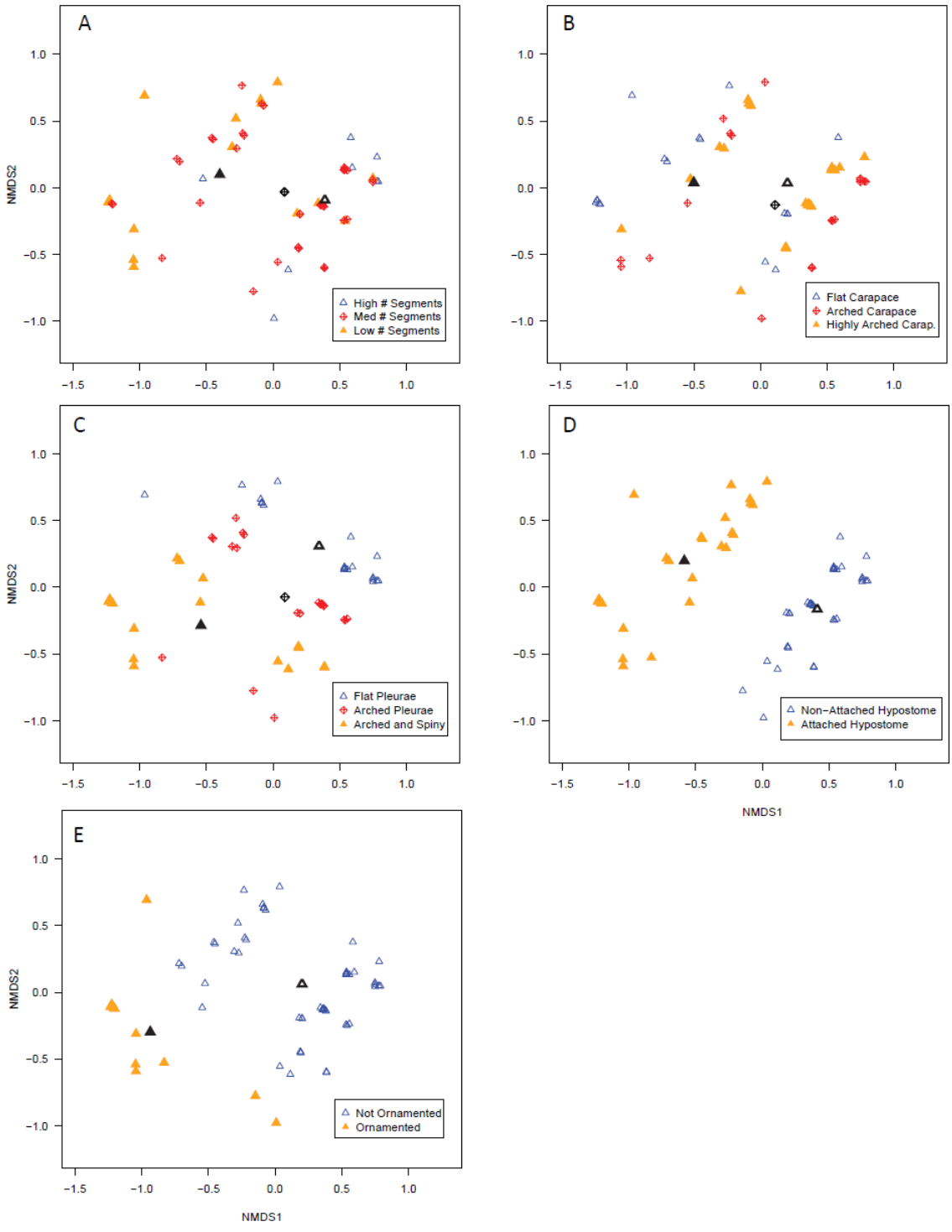
A
High # Segments
Med # Segments
Low # Segments
B
Flat Carapace
Arched Carapace
Highly Arched Carap.
C
Flat Pleurae
Arched Pleurae
Arched and Spiny
D
Non−Attached Hypostome
Attached Hypostome
E
Not Ornamented
Ornamented
NMDS1
NMDS2

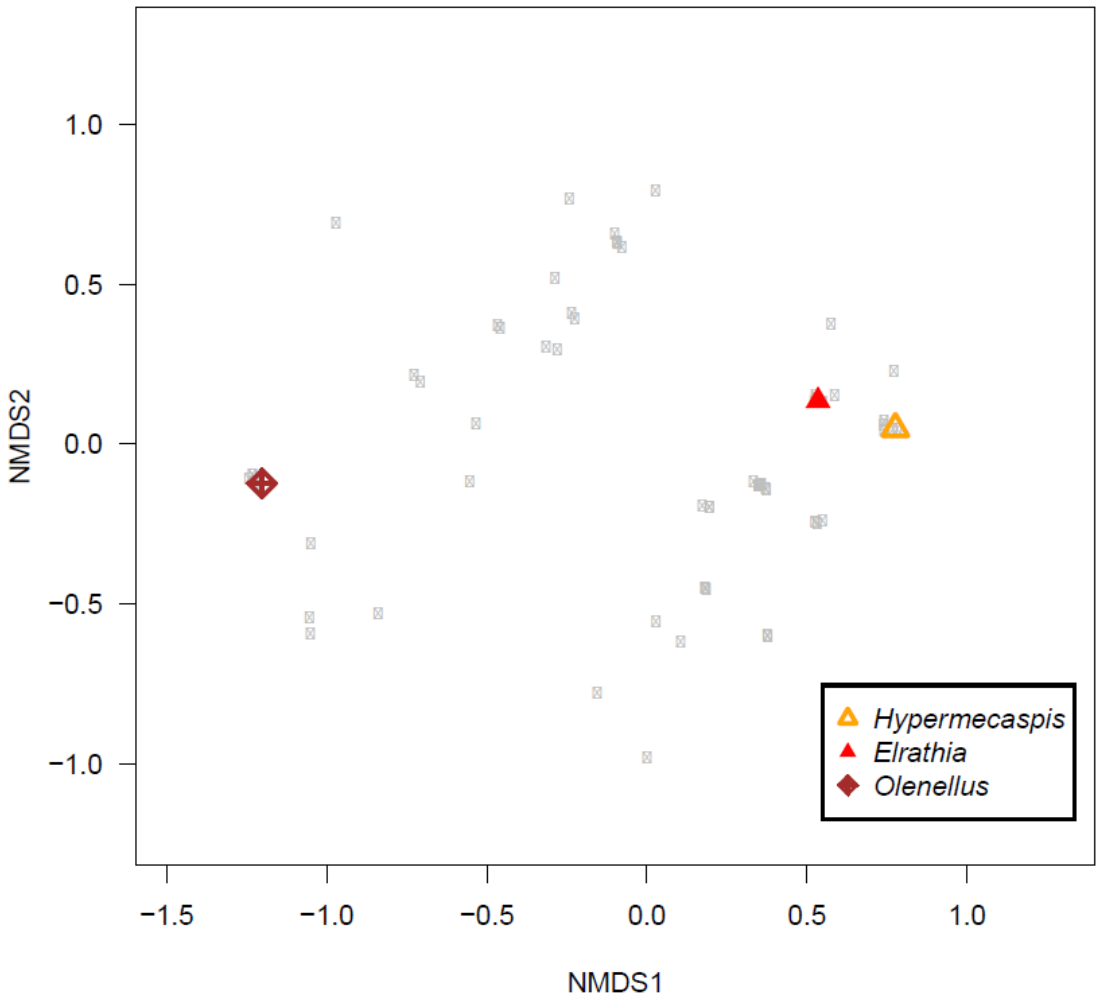

Fig. 2.4. Taxa used to orient the early-to-middle Cambrian NMDS analysis, plotted relative to all trilobite NMDS1 scores. NMDS1 scores for two trilobite genera considered well suited for symbiosis (*Hypermecaspis* and *Elrathia*) and one poorly suited for symbiosis (*Olenellus*) show overall match of results to expectations.

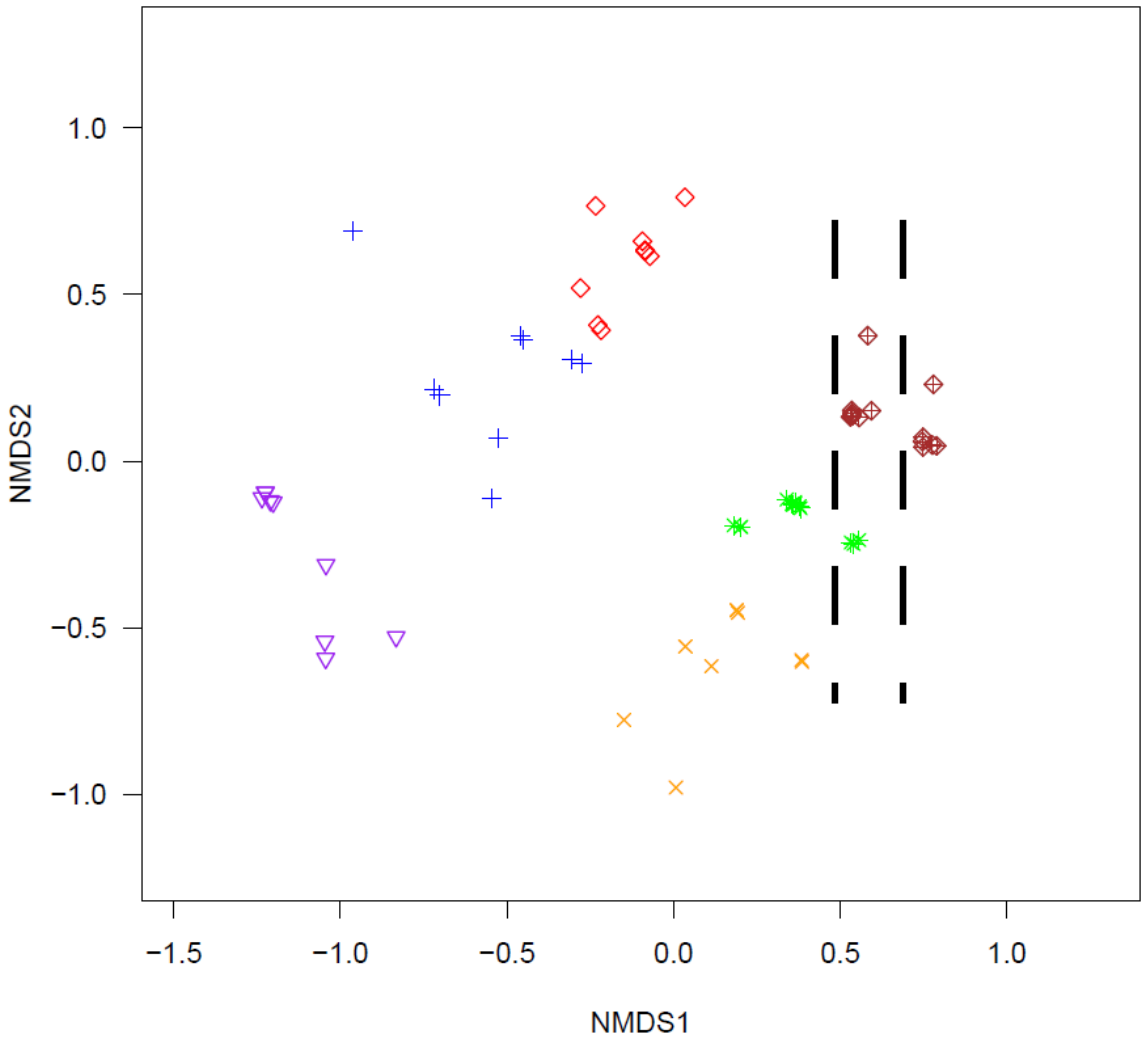

Fig. 2.5. K-means cluster analysis for NMDS scores for trilobites from the early-to-middle Cambrian. Six clusters were identified (see text). Upper cutoff thresholds for 95% confidence intervals from single-sample *t*-tests of ptychopariids are indicated with dashed lines. NMDS1 scores above 0.490 (left dashed line) represent potentially moderately suited genera; scores above 0.673 (right dashed line) represent potentially well-suited genera.

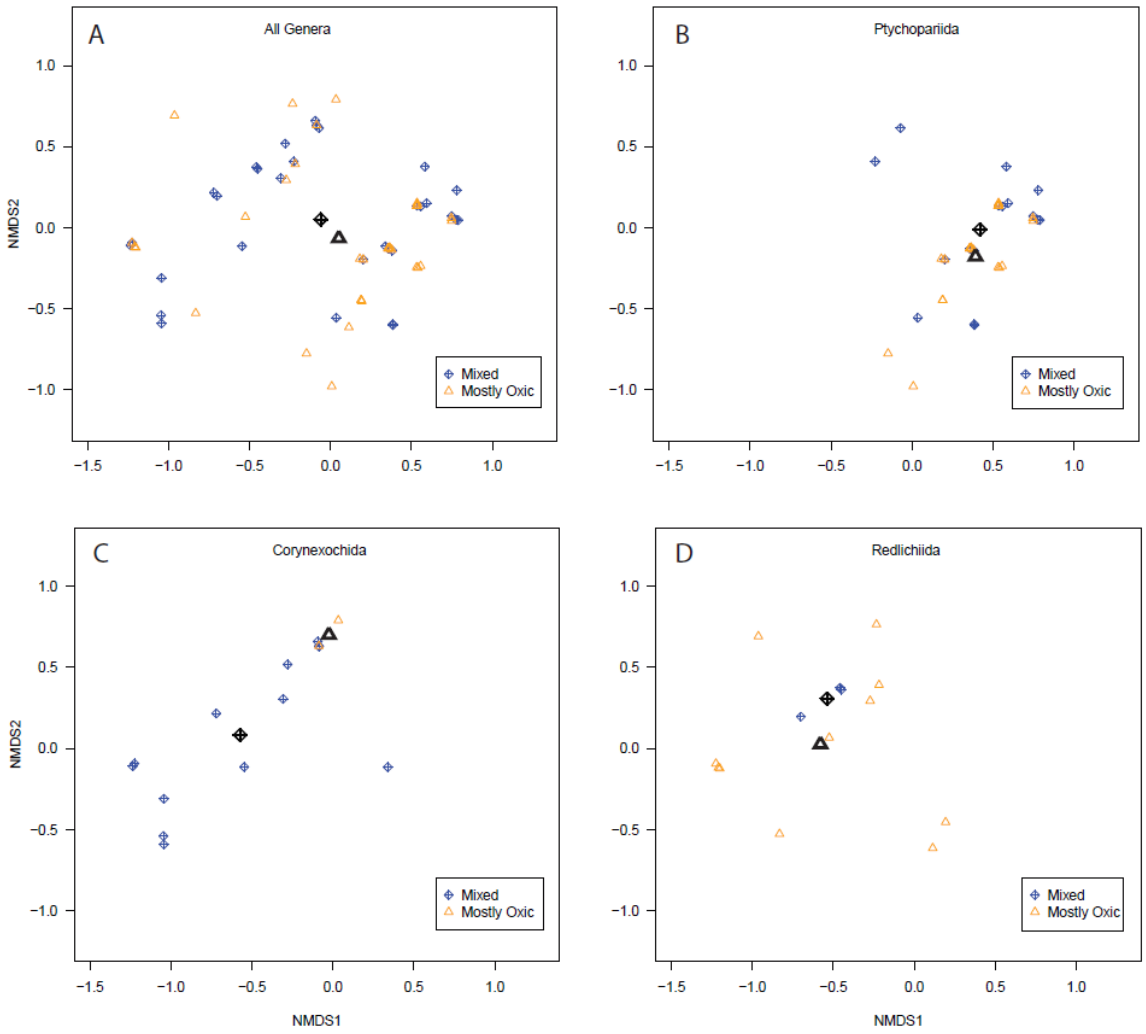

Fig. 2.6. Results of NMDS for mixed and mostly oxic genera in the early-to-middle Cambrian, sorted by taxonomic order. Centroids coded with bold black symbols. A, Combined trilobite genera indicate an even mix of mostly oxic and mixed environments. B, Ptychopariida represent both mostly oxic and mixed environments, and score consistently above zero for both environments. C, Corynexochida represent mainly mixed environments, but score consistently below zero. Mostly oxic corynexochids score higher on average, counter to expectations. D, Redlichiida represent mainly mostly oxic environments, with low average scores, as expected.

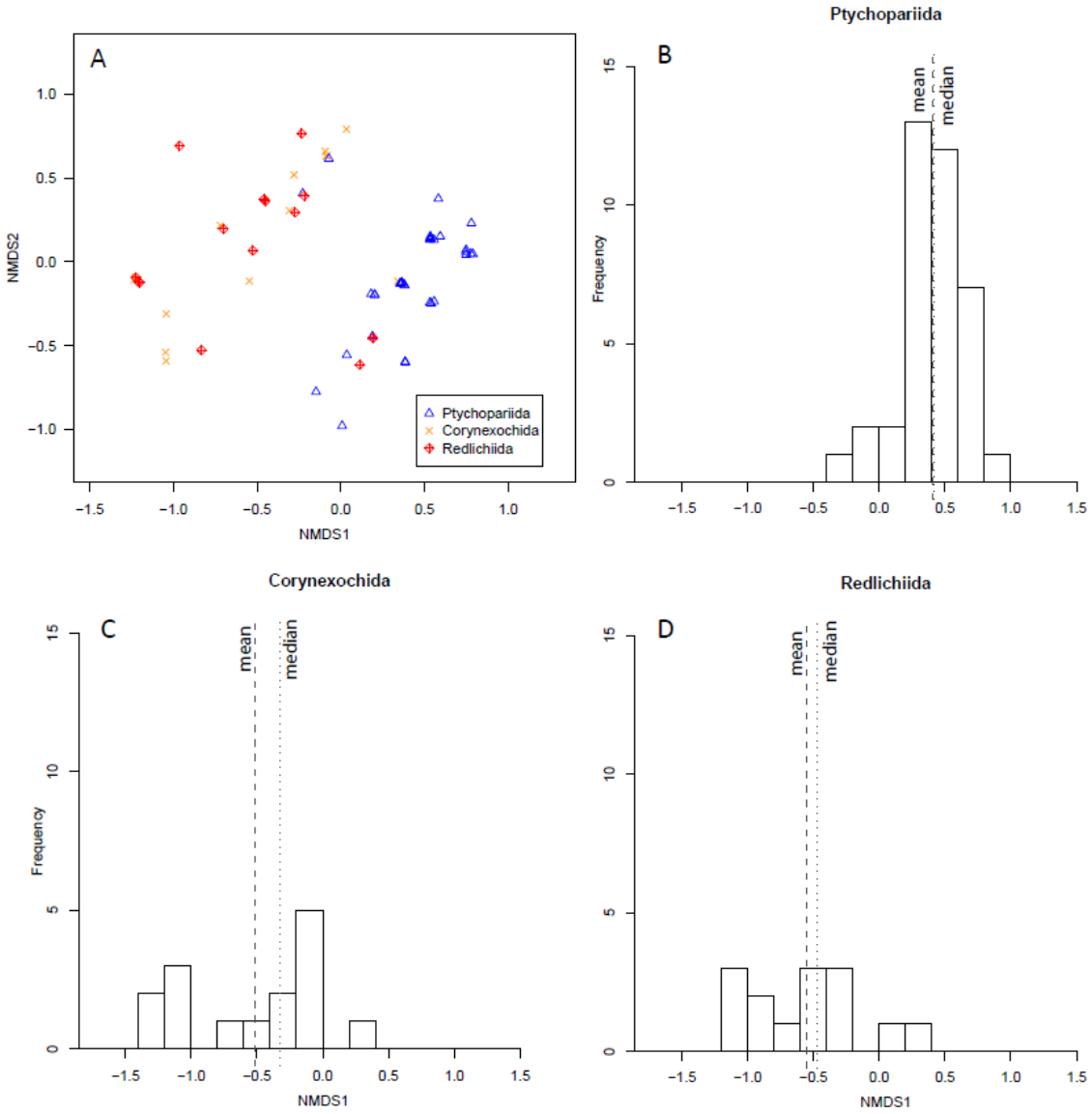

Fig. 2.7. NMDS scores by taxonomic order for the early-to-middle Cambrian trilobites. A, NMDS scores for all trilobite genera coded by order. B, Frequency of NMDS1 scores for ptychopariids, with a mean above zero. C, Frequency of NMDS1 scores for corynexochids, with a mean below zero. D, Frequency of NMDS1 scores for redlichiids, with a mean below zero. Means are indicated with dashed lines, medians with dotted lines.

Fig. 2.8. Results of NMDS for trilobites of the Alum Shale, symbolically coded by character state. Centroids for each character state are coded with bold black symbols. Higher scores on NMDS1 correspond to greater symbiotic suitability. A, Character states for number of segments, with NMDS1 increasing slightly from low to medium number of segments; only one trilobite represented a high number of segments, and scored very low on NMDS1. B, Carapace morphology increases in symbiotic suitability from highly arched, to arched then flat at higher NMDS1 scores. The centroid for flat carapace was omitted to not obscure the two closely-scoring individuals in that group. C, Pleural morphology becomes flatter with higher NMDS1 scores. D, NMDS1 scores for hypostomes define a distinct low-scoring group characterized by attached hypostomes; trilobites with non-attached hypostomes score higher, as expected. E, All trilobites in the Alum Shale have non-ornamented exoskeletons, with a centroid around zero.

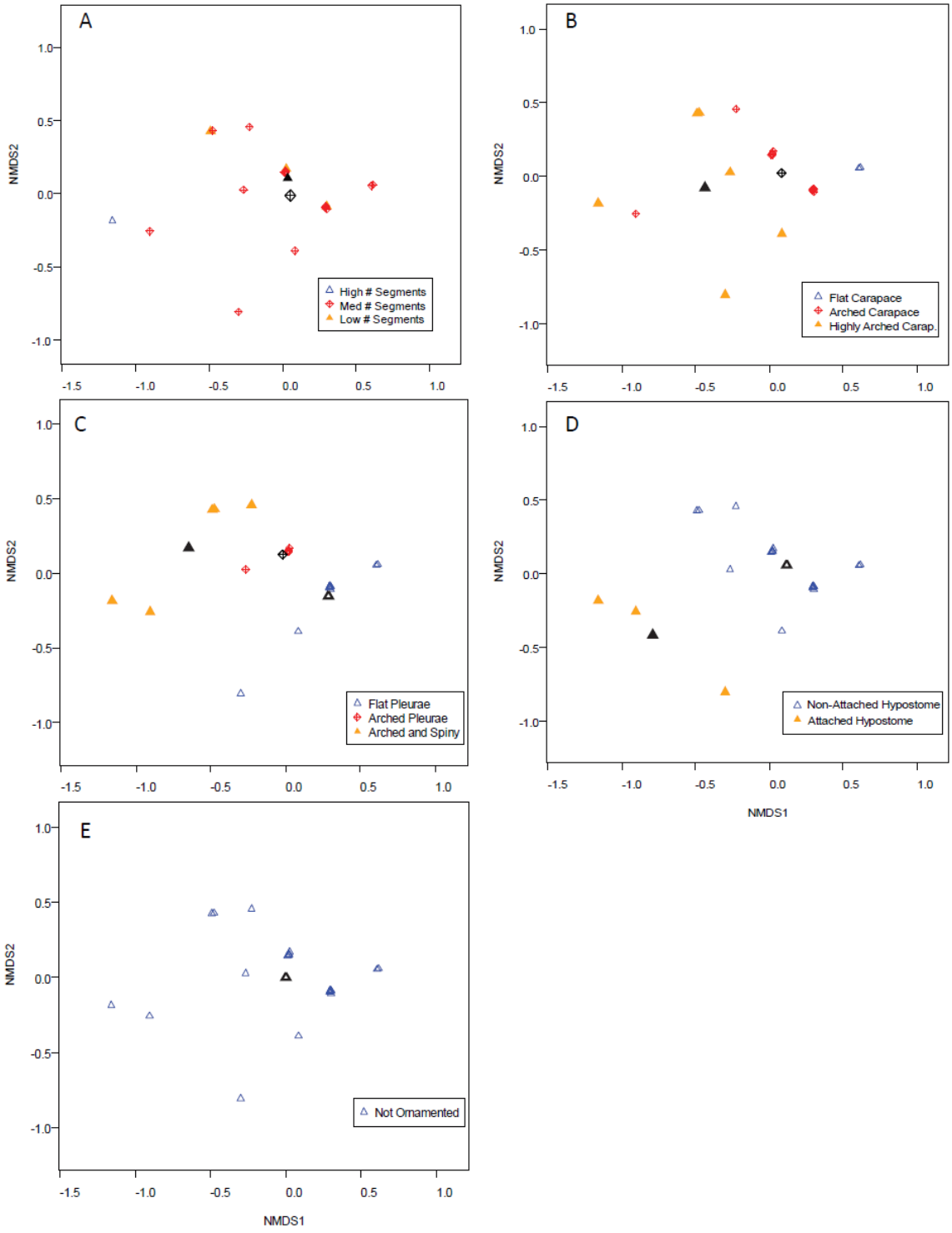
A
NMDS2
High # Segments
Med # Segments
Low # Segments
B
Flat Carapace
Arched Carapace
Highly Arched Carap.
C
Flat Pleurae
Arched Pleurae
Arched and Spiny
D
Non-Attached Hypostome
Attached Hypostome
NMDS1
E
Not Ornamented

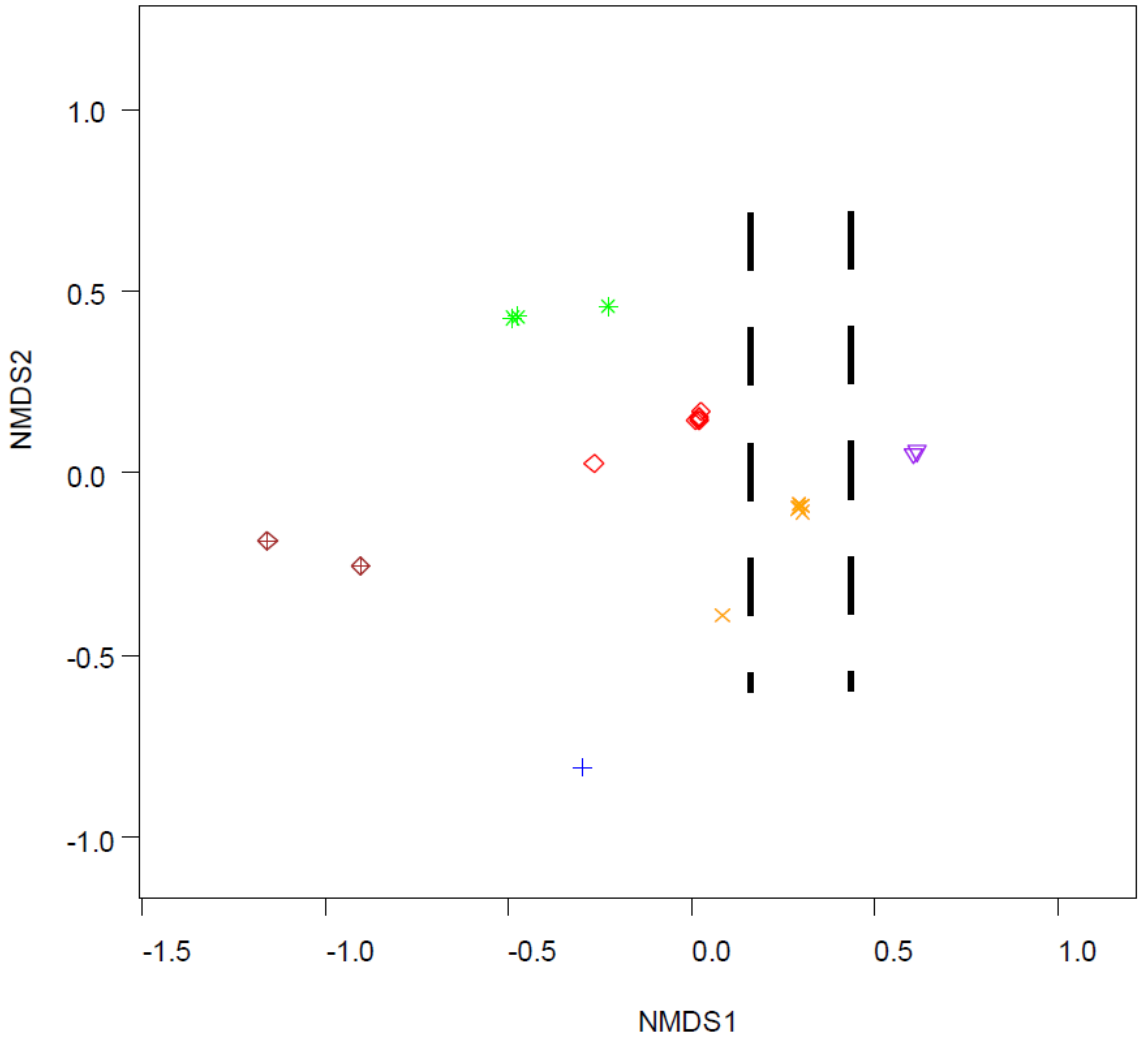

Fig. 2.9. K-means cluster analysis for Alum Shale trilobites based on NMDS. Six clusters were identified (see text). Upper cutoff threshold for 95% confidence intervals from single-sample *t*-tests are indicated with dashed lines. NMDS1 scores above 0.188 (left dashed line) represent genera that are potentially moderately suited for symbiosis. Scores above 0.457 (right dashed line) represent taxa that are potentially well suited for symbiosis.

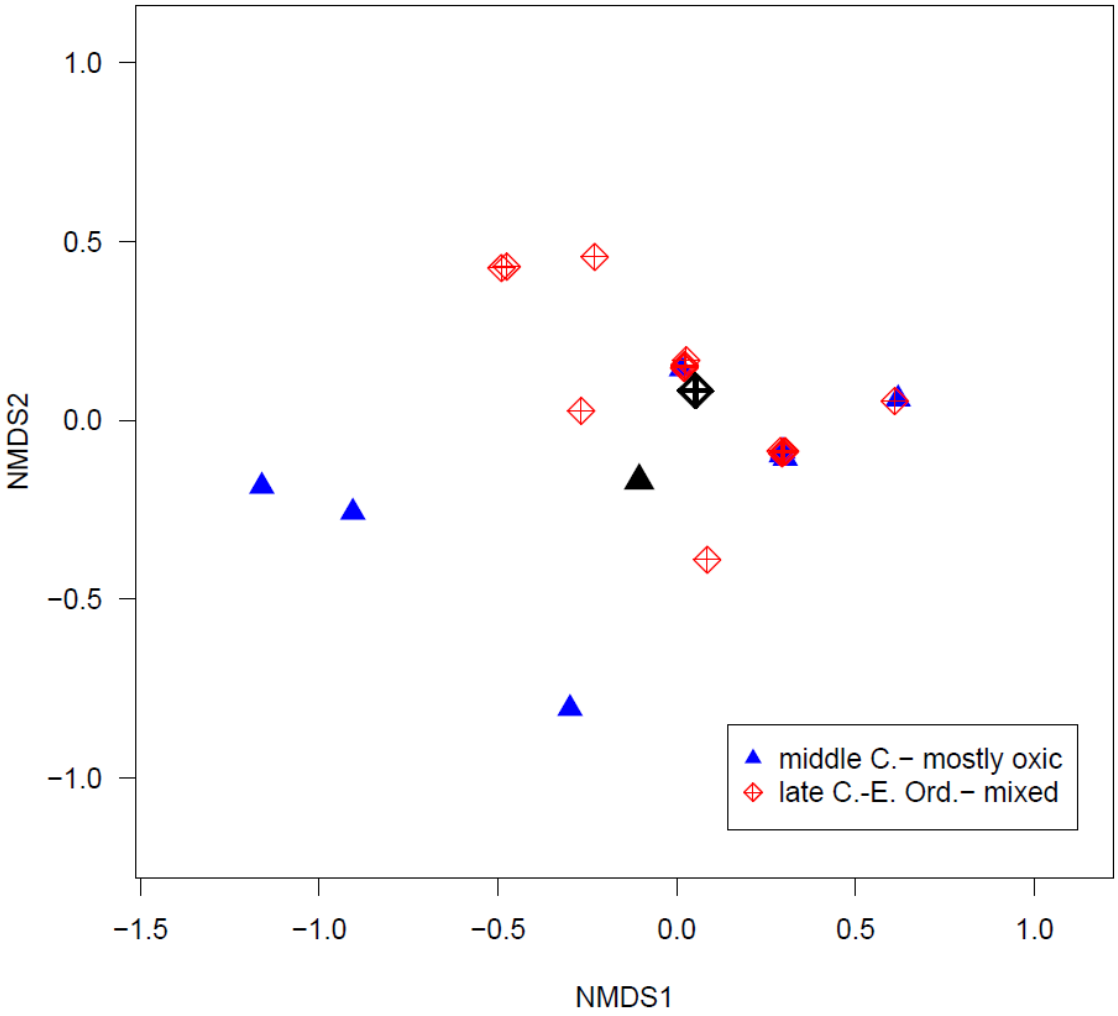

Fig. 2.10. NMDS analysis for trilobites of the Alum Shale, comparing middle Cambrian mostly oxic assemblages to late Cambrian–Early Ordovician mixed assemblages. Middle Cambrian scores have a centroid slightly below zero on NMDS1, while late Cambrian–Early Ordovician centroid is slightly above zero.

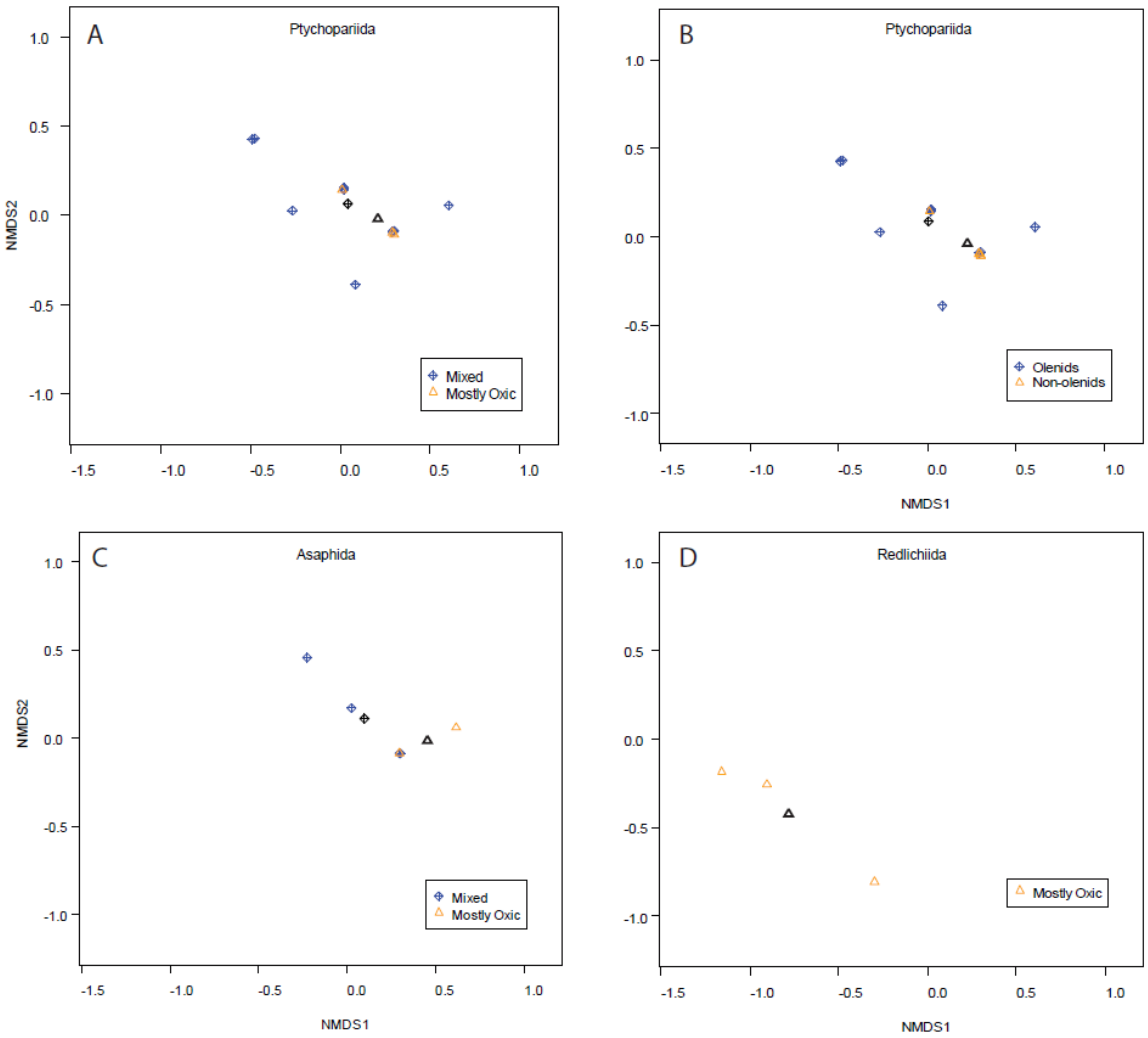

Fig. 2.11. NMDS for mixed and mostly oxic genera in the Alum Shale, separated by taxonomic order. Centroids coded with bold black symbols. A, Ptychopariids are predominately from mixed environments, but mostly oxic ptychopariids score slightly higher, counter to the expectation that symbiotic morphology would be more common in mixed environments. B, Olenids, solely from mixed environments, score lower than non-olenid ptychopariids, from both mixed and mostly oxic environments, counter to expectation. C, Asaphids score consistently high, despite representing both environmental types. D, Redlichiids were solely from mostly oxic environments, and score consistently low on NMDS1, as expected.

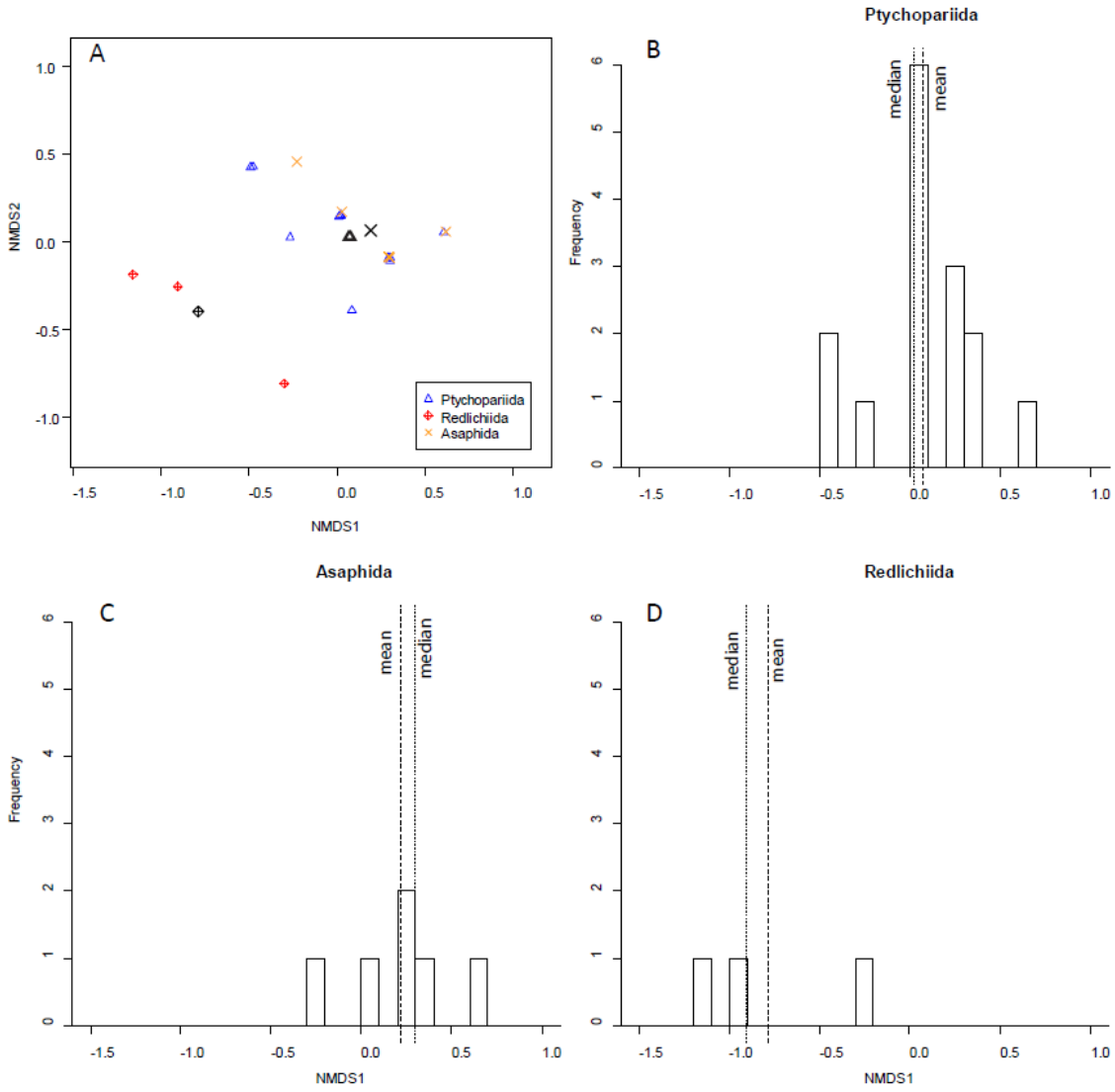

Fig. 2.12. NMDS by taxonomic order for the Alum Shale. Centroids coded with black symbols. A, NMDS scores for all trilobite genera, coded by order. Redlichiids score distinctly lower than asaphids and ptychopariids, which score similarly. B, Frequency of NMDS1 scores for ptychopariids, with a mean around zero. C, Frequency of NMDS1 scores for asaphids, which score slightly higher than ptychopariids (including olenids). D, Frequency of NMDS1 scores for redlichiids, which score entirely below zero. Means indicated by dashed lines, medians by dotted lines.

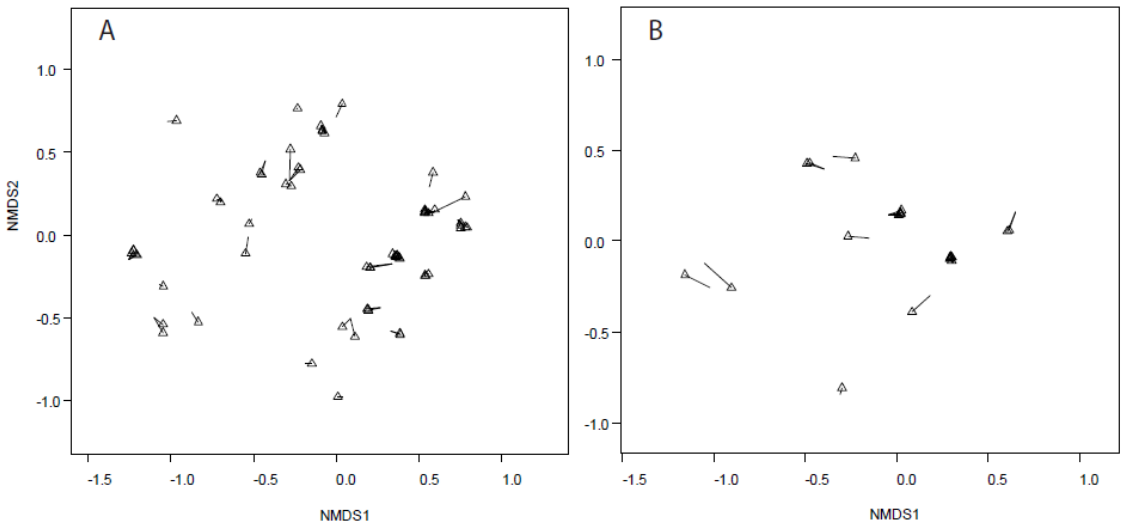

Fig. 2.13. Effects of removing segmentation as a character for both trilobite NMDS analyses. Original NMDS points plotted as triangles (with segments),with direction and magnitude of shift indicated with lines after segmentation was removed from the analysis. A, Shift in NMDS scores for the early-to-middle Cambrian trilobites. Shifts were small, and scores did not shift uniformly negative, as expected if segments were inflating original NMDS1 scores. B, Shift in NMDS scores for the middle Cambrian to early Ordovician Alum Shale trilobites. Shifts were slightly larger than in A, but still minor, and scores do not shift uniformly positive, as expected if segments were deflating original NMDS1 scores.

Table 2.1. Locality information for eight published early-to-middle Cambrian Lagerstätten, with ages, descriptions of paleoenvironments, and number of trilobites from each locality.

Locality	Age	Environment	Genera	References
Emu Bay	e. Camb. (525 Ma)	Mixed: Subsiding basin with anoxic water below sediment-water interface, reduced oxygen above	4	Nedin 1995; Gehling et al. 2011
Chengjiang	e. Camb. (525 Ma)	Mostly oxic: interbedded non-bioturbated but oxic mudstones and storm event horizons	5	Shu et al. 1999; Steiner et al. 2001; Zhao et al. 2009
Latham	e. Camb. (515 Ma)	Mostly oxic: primarily gray-green shales, some cross-laminated sandstone; rare horizons of well-preserved trilobites	4	Palmer and Halley 1979; Gaines and Droser 2003; Webster et al. 2008
Spence	m. Camb.	Mixed: centimeter-scale low-bioturbation claystones and interbedded oxic beds, similar to Wheeler	14	Garson et al. 2011
Jince	m. Camb. (510 Ma)	Mostly oxic: shallow-water marine basinal shales, with few horizons of monospecific trilobites	20	Fatka et al. 2004; Chlupac and Kordule 2002; Retallack 2011
Wheeler	m. Camb. (507 Ma)	Mixed: interbedded dysoxic and oxic beds	12	Gaines and Droser 2003, 2010
Burgess	m. Camb. (505 Ma)	Mixed: allochthonous oxic benthos mixed with autochthonous dysoxic benthos	15	Conway Morris 1986; Caron and Jackson 2008
Marjum	m. Camb. (504 Ma)	Mostly oxic: mostly bioturbated carbonates, few black shale horizons at bottom of unit	16	Hintze and Robison 1975; Brett et al. 2009; Gaines and Droser 2010

Note: mixed environments represent localities with more prevalent, recurring dysoxic intervals. Mostly oxic environments have fewer, more sporadic dysoxic intervals.

Table 2.2. **The five morphological characters**, their character states, and a description of how each might have facilitated symbiosis.

Character	States	Description
Thoracic segments	High: 17 or greater Medium: 9 to 16 Low: 8 or fewer	Estimated number of thoracic segments. Each thoracic segment corresponds to a pair of gill appendages, which would be specialized for cultivating symbiotic bacteria; more segmentation would yield greater surface area for symbionts
Carapace morphology	1: Wide and flat, low axial lobe 0.5: Wide and flat, raised axial lobe 0: Narrow or convex	A wide, flat morphology maximizes surface for symbionts and minimizes unnecessary musculature. A raised axial lobe indicates a more developed thoracic musculature. A more convex overall morphology (commonly manifest as a downward deflection in the angle of pleural lobes from axis to margin) indicates more developed musculature with longer legs, maladapted for symbiont cultivation. A thorax that is narrow, or narrows posteriorly, reduces the surface area available and is also maladapted
Pleural morphology	1: Broad and flat 0.5: Narrow and arched 0: Narrow, arched, and spiny	Broad and flat pleurae have little to no extraneous structure and thus maximize the surface area available for symbiont growth. Narrow, arched pleurae are more convex and may have some structure such as transverse ridges or grooves. Spiny pleurae are separated from adjacent segments at their abaxial end and elongated to form spines. Specialization of pleurae for muscle attachment, predatory defense, substrate support, etc., decreases the surface area available for symbionts
Hypostome attachment	1: Natant 0: Conterminant or impendent	Attachment of hypostome to cephalic doublure. State is inferred from family affiliation; hypostome attachment is conservative at family level (Fortey 1990). Attached hypostomes are more rigid for complex feeding, and would be unnecessary for deriving nutrients from symbionts. Ptychopariids (detritivores) have an unattached (natant) hypostome while

		corynexochids and redlichiids (carnivores) have attached (conterminant or impendent) hypostomes
Exoskeletal ornamentation	1: No ornamentation 0: Spines or pustules	Cuticle thickness was not directly observable for this study. Exoskeletal ornamentation, when observed, was used as a substitute. Ornamentation for predatory defense would be unnecessary in sparsely-inhabited dysoxic environments and would increase metabolic costs during molting. Fortey argued a thin cuticle decreased metabolic costs, thereby making trilobites more symbiotically optimized

Table 2.3. Tests for independence of characters and relation of characters to NMDS1 and to low oxygen conditions for both datasets. Pairwise correlations and statistical significance for relationships of the five character-state values between each other, between characters and NMDS1 scores, and strength of relationship between character states and environmental conditions.

	Character State Pairwise Correlations (Spearman's rho)					
Character	**CM**	**PM**	**HA**	**EO**	**Corr. with NMDS1**	**Relation to oxic/mixed conditions (Kruskal-Wallis chi-squared)**
Early-to-middle Cambrian						
Segments						
Statistic	0.03	0.05	0.41	0.23	0.42	15.328
***p*-value**	0.82	0.67	<0.01	0.06	0.001	0.572
Carapace morphology (CM)						
Statistic		0.17	0.16	0.12	0.36	0.381
***p*-value**		0.17	0.21	0.32	0.003	0.827
Pleural morphology (PM)						
Statistic			0.21	0.38	0.57	1.480
***p*-value**			0.08	<0.01	<0.0001	0.477
Hypostome attachment (HA)						
Statistic				0.39	0.84	2.490
***p*-value**				<0.01	<0.0001	0.115
Exoskeletal ornamentation (EO)						
Statistic					0.61	0.332
***p*-value**					<0.0001	0.565

Alum Shale						
Segments						
Statistic	-0.04	-0.04	-0.49	-	-0.23	7.906
***p*-value**	0.83	0.84	0.02	-	0.287	0.341
Carapace morphology (CM)						
Statistic		0.37	0.35	-	0.70	0.270
***p*-value**		0.07	0.09	-	0.0001	0.874
Pleural morphology (PM)						
Statistic			0.26	-	0.83	1.550
***p*-value**			0.22	-	<0.0001	0.461
Hypostome attachment (HA)						
Statistic				-	0.54	6.571
***p*-value**				-	0.006	0.010
Exoskeletal ornamentation (EO)						
Statistic				-	-	-
***p*-value**				-	-	-

Note: pairwise correlations for the five character states determined via Spearman's rank correlation; correlation (corr.) of each character to the primary NMDS axis, with a *p*-value for the statistical significance of the correlation; n=66 unique genera plus *Hypermecaspis* for early-to-middle Cambrian dataset, n=24 for Alum Shale dataset. Values of Spearman's rho closer to 1 indicate a more monotonic correlation between two variables. Relationship between characters and mostly oxic or mixed localities determined by Kruskal-Wallis rank-sum test (K-W). Higher values indicate a closer relationship. Exoskeletal ornamentation was not comparable in the Alum Shale because all trilobites had the same character state.

Table 2.4. Number of thoracic segments by time and taxonomic order for Cambrian through Early Ordovician trilobites (both datasets combined). Sample size, minimum (Min), mean, maximum (Max) values, and standard deviations (SD) for thoracic segmentation are given for each trilobite order. Total sample size, mean and standard deviation for each time period is also given (Combined).

Time Period	Taxonomic Order	Sample Size	Min	Mean	Max	SD
early Cambrian	Ptychopariids	3	10	12.67	15	2.52
	Redlichiids	10	8	12.30	16	2.87
	Combined	13	-	12.38	-	2.69
middle Cambrian	Corynexochids	15	2	7.33	11	2.02
	Ptychopariids	36	8	13.83	31	4.12
	Redlichiids	5	13	16.43	19	2.55
	Asaphids	2	10	10.00	10	0.00
	Combined	58	-	12.37	-	4.61
late Cambrian-Early Ordovician	Ptychopariids	12	8	11.50	14	2.15
	Asaphids	4	8	9.00	10	1.15
	Combined	16	-	10.88	-	2.22

Note: Data represent 66 genera in the early-to-middle Cambrian data set and 24 genera in the Alum Shale data set. Three genera were represented in both data sets, and these duplicates were not included in this table.

CHAPTER 3

CAMBRIAN TRILOBITES AS ARCHIVES FOR ANTHROPOCENE BIOMARKERS AND OTHER CHEMICAL COMPOUNDS[1]

[1] John, D. J., Medeiros, P. M., Babcock-Adams, L. C., and Walker, S. E. Submitted to *Anthropocene,* April 18 2016.

Abstract

Molecular biomarkers reveal insights into biotic diversity in ancient ecosystems, yet most biomarker analyses target only specific compounds. We used a multibiomarker approach to examine a wide spectrum of organic molecules contained within exceptionally well-preserved middle Cambrian trilobites and associated sediments from the Wheeler Shale. We found an abundance of modern biomarkers, representing algal and plant sources, with evidence of biomass burning. Additionally, anthropogenic compounds comprised up to 96% of all compounds present and included plasticizers, flame retardants, petroleum by-products, and insect repellent. These compounds are usually discarded from analyses, but we argue that they are essential for understanding the entire fossilization process. The pervasiveness of terrestrial and anthropogenic chemicals suggests that these fossils reveal more about Anthropocene-altered terrestrial landscapes than Cambrian oceans.

Introduction

Molecular biomarkers are a widely adopted biogeochemical tool to explore the presence of ancient organisms that otherwise have no macro- or microscopic preservation (Brocks and Summons, 2005; Brocks et al., 2005; Grice et al., 2005; Olcott et al;. 2005; Pawlowska et al., 2012). Refractory biomolecules (and their derivatives) are used to identify early Proterozoic microbial life, bacterial metabolic pathways and taxonomic affinities (Brocks et al., 2005; Olcott et al., 2005; Brocks and Schaeffer, 2008; O'Malley et al., 2013). Biomarkers characteristic of sulfur-oxidizing bacteria such as 16:1ω7c/t and 18:1ω7c phospholipid fatty acids (Zhang et al., 2005) found in association with trilobites could be used to support hypotheses of symbiosis with these organisms (Fortey,

2000). However, even if well preserved for millions of years, rocks and fossils collected at or near the surface are exposed to modern compounds that could overprint the original chemical fossil record (Wischmann et al., 2002; Rasmussen et al., 2008; French et al., 2015). Those compounds are usually discarded from analyses, but we argue that they are essential for understanding the fossilization process. Importantly, conventional biomarker analyses target only specific compounds chosen a priori, but a multibiomarker approach characterizes a wide range of molecular compound classes in an ecosystem (Simoneit et al., 2014). This approach allows for a comprehensive characterization of the biomarker record, with the potential to recognize unexpected signals that would be lost in targeted biomarker analysis.

After a rigorous solvent cleansing regime to eliminate surficial contaminants, we found extensive remaining chemical overprints from modern biomarkers and chemical compounds in Cambrian trilobites and their associated sediments. These chemical compounds reveal a dominantly terrestrial landscape altered by anthropogenic chemicals, and little if anything about the Cambrian seas in which these trilobites lived. Effectively, Anthropocene disturbance is not just at the landscape level, but also permeates through groundwater, overprinting the original chemicals preserved in fossil exoskeletons. Such overprints affect not only what we can discover about ancient ecosystems, but also reveal perturbations concerning the modern environment under which calcareous fossils are buried.

Methods

Trilobites were quarried commercially from the middle Cambrian Wheeler Shale by professional collectors (West Desert Collectors and Terra Trilobites, Delta UT) from rock depths up to 5 meters representing rock with little, if any, visible weathering. Two specimens of *Elrathia* and 16 *Peronopsis* with robust and complete exoskeletons were used (Fig. 3.1). The trilobites and their associated cone-in-cone encrustations were separated from the underlying sediment, with both fossils and sediment being used for analysis (Fig. 3.2). The 16 *Peronopsis* were combined into two sets of eight for analysis, to yield a comparable sample mass to the *Elrathia* and ensure sufficient material for analysis. Because compounds from anthropogenic polymers are particularly pervasive, to minimize plastic contamination, two additional *Elrathia kingii* and five *Peronopsis*, both with associated sediment, were collected and protected from contact with any type of plastics during extraction, shipping, and handling. The five protected *Peronopsis* were combined for analysis, but did not yield any compounds above the detection limit, despite repeated tests on the sample material, and thus these samples could not be interpreted.

Total carbon for sediments was determined by powdering sediment samples associated with both trilobite species in a Spex 8000 ball mill to produce approximately 20 ml of powdered sediment. 100 mg of these powders were weighed into a crucible boat and fired on an Eltra furnace to 1350°C under a pure oxygen atmosphere. The resultant carbon dioxide was measured by infrared absorption on an Eltra CS500 determinator to yield the total weight percent carbon in the sample. Total inorganic carbon was then determined by weighing another 100 mg of the same sample powder into a 250 ml flask and mixing with 10 ml of ethanol, then connecting the flask to an Eltra

CS500 determinator, adding 10 ml of 20% HCl and heating to 50°C, and measuring the resultant carbon dioxide as above. Total organic carbon was determined by subtracting the inorganic carbon from the total carbon for each sample, and averaging values by species. Carbon and inorganic carbon analysis was performed at the Lyons Lab at UC Riverside.

Sediment and exoskeletal samples were prepared for multibiomarker analysis by GC-MS, yielding a profile of individual biomarkers present in each sample, following a multibiomarker method established by Medeiros and Simoneit (2007; 2008a; 2008b) and Simoneit et al. (2014). This method allows for a simultaneous characterization of the different chemical classes spanning a wide range of polarities, without a need to isolate certain chemical classes before analysis. Protected samples were rinsed with Milli-Q water upon arrival, and after drying, they were gently rinsed with dichloromethane followed by methanol and left to dry again at room temperature. All samples were powdered in a solvent pre-cleaned ball mill and then weighed in a pre-combusted (450°C for 5 h) beaker. Samples were then sonicated twice for 15 min in a 30 mL mixture of dichloromethane:methanol (2:1, v/v). The extract aliquots were combined and filtered using a Gelman Swinney filtration unit containing an annealed pre-combusted glass fiber filter (42.5 mm, Whatman) for the removal of insoluble particles. The filtrate was first concentrated in a RapidVap (solvent evaporation system) to about 1.5 mL, then further to 500 μL using a stream of high-purity nitrogen. Aliquots of the total extracts were evaporated completely using a stream of filtered nitrogen gas, and then converted to their trimethylsilyl derivatives using BSTFA containing 1% TMCS and pyridine for 3 h at

70°C. Immediately before GC-MS analysis, derivatized extracts were evaporated to dryness using nitrogen gas and redissolved in hexane for injection.

Aliquots of 1 μL of silylated total extracts were analyzed within 24 hours using a HP 6890 gas chromatograph interfaced with a HP 5975 mass selective detector (GC-MS). A DB5-MS capillary column (30 m x 0.25 mm I.D. and film thickness of 0.25 μm) was used with helium as the carrier gas at a constant flow rate of 1.3 mL min-1. The injector and MS source temperatures were maintained at 280°C and 230°C, respectively. The column temperature program consisted of injection at 65°C and hold for 2 min, temperature increase of 6°C min-1 to 300°C, followed by an isothermal hold at 300°C for 15 min. The MS was operated in the electron impact mode with an ionization energy of 70 eV. The scan range was set from 50 to 650 Da and the samples were analyzed in splitless mode.

Data were acquired and processed with the HP-Chemstation software. Individual compounds were identified by comparison of mass spectra with literature and library data, comparison of mass spectra and GC retention times with those of authentic standards and/or interpretation of mass spectrometric fragmentation patterns. Compounds were quantified using the total ion current (TIC) peak area, and converted to compound mass using calibration curves of external standards: n-eicosene for n-alkanes, isoprenoids, UCM, and phthalates; n-hexadecanoic acid for n-alkanoic acids, n-alkanols and glyceride derivatives; lupeol for diterpenoids, sterols and lignin derivatives; glucose for monosaccharides; sucrose for disaccharides. A procedural blank was run in sequence to samples, presenting no significant background interferences.

There was a higher percentage of natural biogenic compounds among protected (65.84%) than unprotected (23.58%) exoskeletons and sediments, and anthropogenic concentrations were likewise lower among protected specimens (Table 3.1; Appendix 3.1), indicating that collection protocols were successful in eliminating anthropogenic contaminants introduced during or after collection. Therefore, remaining anthropogenic compounds represent mainly those introduced to samples in situ.

Results and Discussion

Biogenic compounds in ancient trilobites

Our exoskeletal and sediment samples contained more than 50 molecular biomarkers and anthropogenic organic compounds representing twelve chemical classes (Appendix 3.1). Nine of the classes indicate biogenic input from either microorganism biomass or terrestrial vegetation. Three classes were anthropogenic and in most samples constituted the preponderance of the biomarkers by concentration (Fig. 3.3; Table 3.1).

Total carbon and organic carbon in the sediment were measured to quantify the overall proportion of organic material from which biomarkers could be identified; total carbon ranged from 3.69% by weight (*Elrathia* sediment) to 4.48% (*Peronopsis* sediment), with total organic carbon comprising 0.35% and 0.33% by weight, respectively. The similarity in organic carbon suggests that biomarker records between species should be directly comparable.

Microorganism-derived biomarkers were abundant in sediments and particularly in protected *Elrathia* exoskeletons, but nearly absent from unprotected exoskeletons (Table 3.1). The presence of a low molecular-weight ($\leq C_{20}$) homologous series,

especially n-alkanoic acids with a nearly total even-to-odd carbon preference ($C_{14:0}$, $C_{16:0}$, $C_{18:0}$), and to a lesser degree n-alkanes, n-alkanols, and glyceride derivatives are indicative of microorganisms (Simoneit, 1977; Medeiros and Simoneit, 2008a). The phytosterols stigmasterol and sitosterol were minor in our samples; whereas cholesterol was found in slightly higher concentrations, especially in protected samples (Table 3.1). Phytosterols are components of plant lipid membranes, but are also detected in microalgae (Volkmann et al., 1998). Cholesterol is considered a major animal sterol (Puglisi et al., 2003), but it is also a predominant compound in algal detritus (Goad, 1978; Medeiros and Simoneit, 2008a), suggesting algae is the most likely source for all three sterols.

Terrestrial plant biomarkers were present in protected and unprotected trilobites (Figs. 3.4, 3.5; Table 1) and in sediments (Figs. 3.6, 3.7). The diterpenoid dehydroabietic acid, a conifer-specific biomarker (Otto and Wilde, 2001), was detected in protected and unprotected sediment and protected *Elrathia* exoskeletons (Table 3.1). Lignin derivatives (vanillin and 3-methoxy-benzaldehyde; Opsahl and Benner, 1995) were also detected in protected *Peronopsis* sediment, with vanillin occurring in unprotected sediments (Table 3.1). Because our methods do not include the oxidation/hydrolysis of biopolymers such as lignin and cellulose, their detection in solvent-extractable samples indicates that biomass burning may have released the monomer derivative products of biopolymers (Medeiros and Simoneit, 2008b). Indeed, the anhydrosaccharide levoglucosan, a product of burning cellulose from general plant biomass (Simoneit et al., 1999), was detected in most of the samples, indicating that plant biomarkers may have been released by forest wildfires overlying the buried fossils.

The carbon preference of n-alkanes suggests that the terrestrial plant record is overprinted by another source. High molecular weight n-alkanes (> C_{20}) with an odd-to-even carbon preference indicate terrestrial biogenic input. However, an even-to-odd carbon preference would point to plastic contamination (Simoneit et al., 2005). The lack of a strong carbon number preference among the unprotected trilobites (Carbon Preference Index, CPI = 0.7 – 0.8), combined with the abundant presence of plasticizers (discussed below) suggests a mixture of both terrestrial and plastic inputs for the n-alkanes (Table 3.1). The presence of C_{24}, C_{26} and C_{28} n-alkanols (with an even-to-odd carbon preference) indicate input from plant wax (Medeiros and Simoneit, 2008a).

Protected exoskeletons of *Elrathia* had saccharides, but not their unprotected skeletons (Table 3.1). Especially, protected *Elrathia* sediment had the highest saccharides present. This finding is unexpected, as sugars are readily consumed by microbes and are generally not preserved in the rock record, suggesting the sugars are modern (Swain et al., 1970; Chao et al., 2000). Saccharides were present in protected *Elrathia* exoskeletons, though less abundantly than in sediments, and were absent in unprotected exoskeletons (Fig. 3.4; Table 3.1). Glucose is the most common saccharide present in the sediment and is the most abundant single component in protected *Elrathia* sediment (Fig. 3.6; Table 3.1). Glucose is ubiquitous to all life and not diagnostic of any source (Medeiros and Simoneit, 2007). Sucrose, indicative of general plant input, and mycose, indicative of fungal input, occurred primarily in unprotected sediments (Table 1). It is likely that the saccharides were emplaced by groundwater before collection.

Anthropogenic compounds in ancient trilobites

Anthropogenic compounds represent the highest concentration of any compound class overall, and was the predominant class in all exoskeletons (Fig. 3.3; Table 3.1). Unprotected trilobites had more anthropogenic compounds (91.71% and 96.16% by weight for *Elrathia* and *Peronopsis*, respectively) than protected *Elrathia* (44.72% by weight). This difference indicates that protection protocols had some effect on limiting anthropogenic contamination, but protected specimens still contained substantial amounts of human-derived chemicals. The remaining anthropogenic compounds in protected specimens represent *in situ* contamination before collection, indicating synthetic chemicals are pervasive in the groundwater. Additionally, some contamination after collection through airborne particles or incidental contact may have occurred despite precautions.

Unprotected trilobites and protected *Elrathia* exoskeletons were generally enriched in anthropogenic organophosphines and plasticizers relative to their associated sediments (Table 3.1). Phthalates, which are plasticizers used in the plastic industry (Wittasek et al., 2011), and triphenylphosphine oxide (TPPO), a flame retardant additive in plastics (Weil and Levchik, 2009), were the most common anthropogenic markers among all samples. Phthalates and organophosphines were, in general, also notably higher in trilobite exoskeletons than sediments, with unprotected *Peronopsis* showing a particular affinity for phthalates relative to unprotected *Elrathia* (55,638.2 10^{-9}g g^{-1} to 2400.0 10^{-9}g g^{-1} average concentration, respectively; Table 3.1).

Phthalates adsorb more readily onto microcrystalline calcite and clay particles than on other siliciclastic sediments, mostly as a function of surface area (Sullivan et al., 1982). Sediment, composed of clays and micrometer-scale calcite particles, would be

expected to have a much greater surface area, and therefore a higher concentration of plasticizers, than in exoskeletons; however, that is not what we found. Because trilobites had more organophosphines and plasticizers in their skeletons than in the surrounding sediments, their microstructural properties could be particularly effective adsorbents for organic compounds. *Peronopsis* also had higher concentrations of n-alkanes (probably plastic-derived) relative to *Elrathia*. These results suggest that *Peronopsis* exoskeletons have a greater affinity for organic adsorbates. Perhaps their exoskeletons are microstructurally different from *Elrathia*, but we cannot discount that the difference is related to our methods: we amalgamated five of the much smaller *Peronopsis*, incorporating more surface area to yield equivalent sample mass to *Elrathia*.

Anthropogenic compounds were also found in the sediments, ranging from 73.73% by weight in protected *Peronopsis* sediments to 3.81% by weight in protected *Elrathia* sediments (Fig. 3.3; Table 1). Anthropogenic compounds in unprotected sediments include m-toluamide and benzamide, which may be a degradation product of N,N-Diethyl-meta-toluamide (DEET), an insect repellent (Pellegrino et al., 2011). An unresolved complex mixture (UCM) was found in both unprotected and protected sediments. UCMs are frequently associated with petroleum inputs (White et al., 2013; Fig. 3.7; Supplementary Table 1), suggesting urban atmospheric particulates entrapped in groundwater. Groundwater interaction may account for the introduction of plastics, as phthalates are weakly water soluble when associated with dissolved organic macromolecules such as humic acids and adsorb readily onto particulate surfaces in the sediment, especially calcite and clays (Sullivan et al., 1982; Bauer et al., 1998; Huang et al., 2008).

Conclusion

Our work highlights the potential for the biogeochemical record of fossils to be used as a proxy for modern ecosystem change and Anthropocene alteration. Biomarkers and other chemical compounds preserved in middle Cambrian trilobites revealed a modern history of terrestrial forests and wildfires, petroleum by-products, fire-retardants, and common insect repellants. These compounds can overprint the original biogenic signal and are abundant throughout the environment. Preventative collection protocols and extensive de-contamination of the samples yielded some reduction in anthropogenic compounds, but not a substantial one. The use of multibiomarkers allowed us to capture these additional data that are usually separated by fractionation and discarded from biomarker analyses. We argue that the same preservational potential that makes fossils a source of biomarker data also makes them susceptible to adsorption and accumulation of anthropogenic chemicals. As these chemicals become more pervasive in the environment, they have the potential to inhibit our ability to detect and reconstruct ancient ecosystems, but provide a trove of information about perturbations in modern ecosystems.

References

M. J. Bauer, R. Herrmann, A. Martin, H. Zellmann, Chemodynamics, transport behaviour and treatment of phthalic acid esters in municipal landfill leachates. Water Sci. Tech. **38** 185-192 (1998).

J. J. Brocks, R. E. Summons, Biomarkers for early life. Biogeochemistry **8** 63-115 (2005).

J. J. Brocks, G. D. Love, R. E. Summons, A. H. Knoll, G. A. Logan, S. A. Bowden, Biomarker evidence for green and purple sulphur bacteria in a stratified Palaeoproterozoic sea. Nature **437** 866-870 (2005).

J. J. Brocks, P. Schaeffer, Okenane, a biomarker for purple sulfur bacteria (Chromatiaceae), and other new carotenoid derivatives from the 1640 Ma Barney Creek Formation. Geochim. Cosmochim. Acta **72** 1396-1414 (2008).

L. Chao, P. Peng, G. Sheng, F. Jiamo, Precambrian organic matter. Chin. Sci. Bull. **45** 295-303 (2000).

R. Fortey, Olenid trilobites: the oldest known chemoautotrophic symbionts? PNAS **97** 6574-6578 (2000).

K. L. French, C. Hallmann, J. M. Hope, P. L. Schoon, J. A. Zumberge, Y. Hoshino, C. A. Peters, S. C. George, G. D. Love, J. J. Brocks, R. Buick, Reappraisal of hydrocarbon biomarkers in Archean rocks. Proc. Nat. Acad. Sci. **112** 5915-5920 (2015).

L. J. Goad, The sterols of marine invertebrates: composition, biosynthesis, and metabolites, in Marine Natural Products, P. J. Scheuer, Ed. (Academic Press, London, 1978), pp. 75-172.

K. Grice, R. J. Twitchett, R. Alexander, C. B. Foster, C. Looy, A potential biomarker for the Permian–Triassic ecological crisis. Earth Planet. Sci. Lett. **36** 315-321 (2005).

P. C. Huang, C. J. Tien, Y. M. Sun, C. Y. Hsieh, C. C. Lee, Occurrence of phthalates in sediment and biota: relationship to aquatic factors and the biota-sediment accumulation factor. Chemosphere **73** 539-544 (2008).

P. M. Medeiros, B. R. T. Simoneit, Analysis of sugars in environmental samples by gas chromatography-mass spectrometry. J. Chromatogr. A **1141** 271-278 (2007).

P. M. Medeiros, B. R. T. Simoneit, Multi-biomarker characterization of sedimentary organic carbon in small rivers draining the northwestern United States. Org. Geochem. **39**, 52-74 (2008a).

P. M. Medeiros, B. R. T. Simoneit, Source profiles of organic compounds emitted upon *combustion* of green vegetation from temperate climate forests. Environ. Sci. *Technol.* **42** 8310-8316 (2008b).

A. N. Olcott, A. L. Sessions, F. A. Corsetti, A. J. Kaufman, T. F. de Olivera, Biomarker evidence for photosynthesis during Neoproterozoic glaciation. Science **310** 471-473 (2005).

C. E. O'Malley, W. I. Ausich, Y. Chang, Isolation and characterization of the earliest taxon-specific organic molecules (Mississippian, Crinoidea). Geology **41** 347-350 (2013).

S. Opsahl, R. Benner, Early diagenesis of vascular plant tissues: lignin and cutin decomposition and biogeochemical implications. Geochim. Cosmochim. Acta **59** 4889−4904 (1995).

A. Otto, V. Wilde, Sesqui-, di-, and triterpenoids as chemosystematic markers in extant conifers – a review. Bot. Rev. **67** 141–238 (2001).

M. M. Pawlowska, N. J. Butterfield, J. J. Brocks, Lipid taphonomy in the Proterozoic and the effect of microbial mats on biomarker preservation. Geology **41** 103-106 (2012).

M. Pellegrino, N. Steinbach, M. C. Stensmyr, B. S. Hansson, L. B. Vosshall, A natural polymorphism alters odour and DEET sensitivity in an insect odorant receptor, Nature **478** 511-514 (2011).

E. Puglisi, M. Nicelli, E. Capri, M. Trevisan, A. A. M. Del Re, Cholesterol, β-sitosterol, ergosterol, and coprostanol in agricultural soils. J. Environ. Qual. **32**, 466-471 (2003).

B. Rasmussen, I. R. Fletcher, J. J. Brocks, M. R. Kilburn, Reassessing the first appearance of eukaryotes and cyanobacteria. Nature **45** 1101-1104 (2008).

B. R. T. Simoneit, Diterpenoid compounds and other lipids in deep-sea sediments and their geochemical significance. Geochim. Cosmochim. Acta **41** 463-476 (1977).

B. R. T. Simoneit, J. J. Schauer, C. G. Nolte, D. R. Oros, V. O. Elias, M. P. Fraser, W. F. Rogge, G. R. Cass, Levoglucosan, a tracer for cellulose in biomass burning and atmospheric particles. Atmos. Environ. **33** 173–182 (1999).

B. R. T. Simoneit, D. R. Oros, P. M. Medeiros, Organic matter provenance and paleoenvironment in the Cretaceous on the Manihiki Plateau, South Pacific. Palaeogeogr. Palaeoclimatol. Palaeoecol. **409** 48-56 (2014).

B. R. T. Simoneit, P. M. Medeiros, B. M. Didyk, Combustion products of plastic as indicators for refuse burning in the atmosphere. Environ. Sci. Technol. **39**, 6961-6970 (2005).

K. F. Sullivan, E. L. Atlas, C. S. Giam, Adsorption of phthalic acid esters from seawater. Environ. Sci. Technol. **16** 428-432 (1982).

F. M. Swain, J. M. Bratt, S. Kirkwood, Carbohydrates from Precambrian and Cambrian rocks and fossils. Geol. Soc. Am. Bull. **81** 499-504 (1970).

J. K. Volkman, S. M. Barrett, S. I. Blackburn, M. P. Mansour, E. I. Sikes, F. Gelin, Microalgal biomarkers: a review of recent research developments. Org. Geochem. **29** 1163–1179 (1998).

E. D. Weil, S. V. Levchik, Polystyrenes and Thermoplastic Styrene Copolymers. In *Flame Retardants for Plastics and Textiles* (Carl Hanser Verlag, 2009), pp. 35-57.

H. K. White, L. Xu, P. Hartmann, J. G. Quinn, C. M. Reddy, Unresolved Complex Mixture (UCM) in coastal environments is derived from fossil sources. Environ. Sci. Technol. **47** 726-731 (2013).

H. Wischmann, S. Hummel, M. A. Rothschild, B. Herrmann, Analysis of nicotine in archeological skeletons from the Early Modern Age and from the Bronze Age. Anc. Biomol. **4** 47-52 (2002).

M. Wittassek, H. M. Koch, J. Angerer, T. Bruning, Assessing exposure to phthalates – the human biomonitoring approach. Mol. Nutr. Fo od Res. **55** 7-31 (2011).

C. L. Zhang, Z. Huang, J. Cantu, R. D. Pancost, R. L. Brigmon, T. W. Lyons, R. Sassen, Lipid biomarkers and carbon isotope signatures of a microbial (*Beggiatoa*) mat associated with gas hydrates in the Gulf of Mexico. Appl. Environ. Microbiol. **71** 2106 (2005).

Figures and Tables

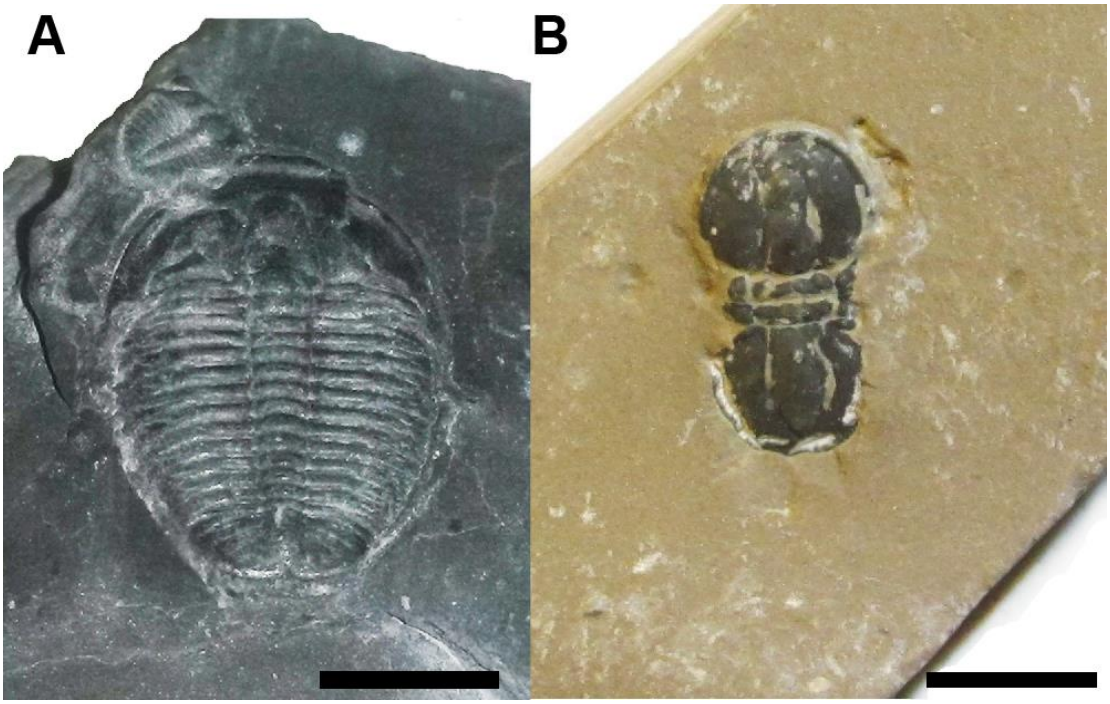

Fig. 3.1. Common Wheeler Shale trilobites used for multibiomarker analyses. (A) The ptychopariid *Elrathia kingii*; (B) the agnostid *Peronopsis*. Scale bar = 0.5 cm.

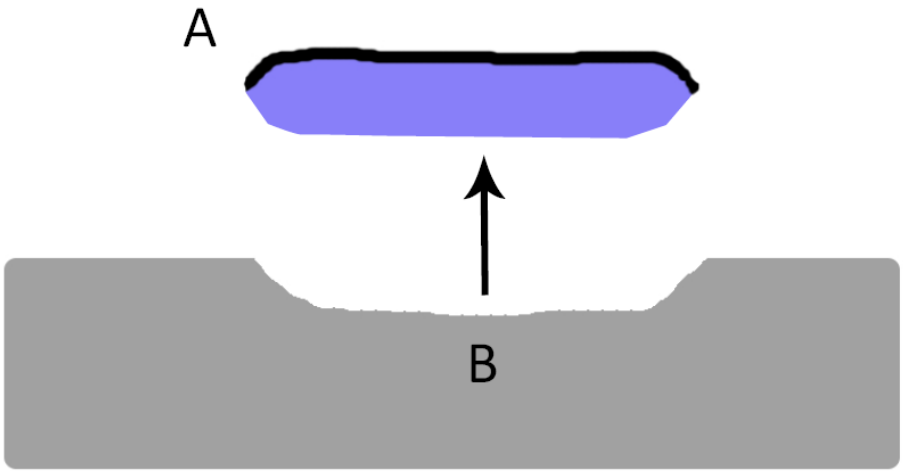

Fig. 3.2. Location of samples. Exoskeleton (black) and cone-in-cone (blue; A) were separated from sediments (B). Exoskeleton and cone-in-cone were pulverized and analyzed together to yield data for *Elrathia* and *Peronopsis*, and sediment underneath cone-in-cone was pulverized and analyzed separately for its data.

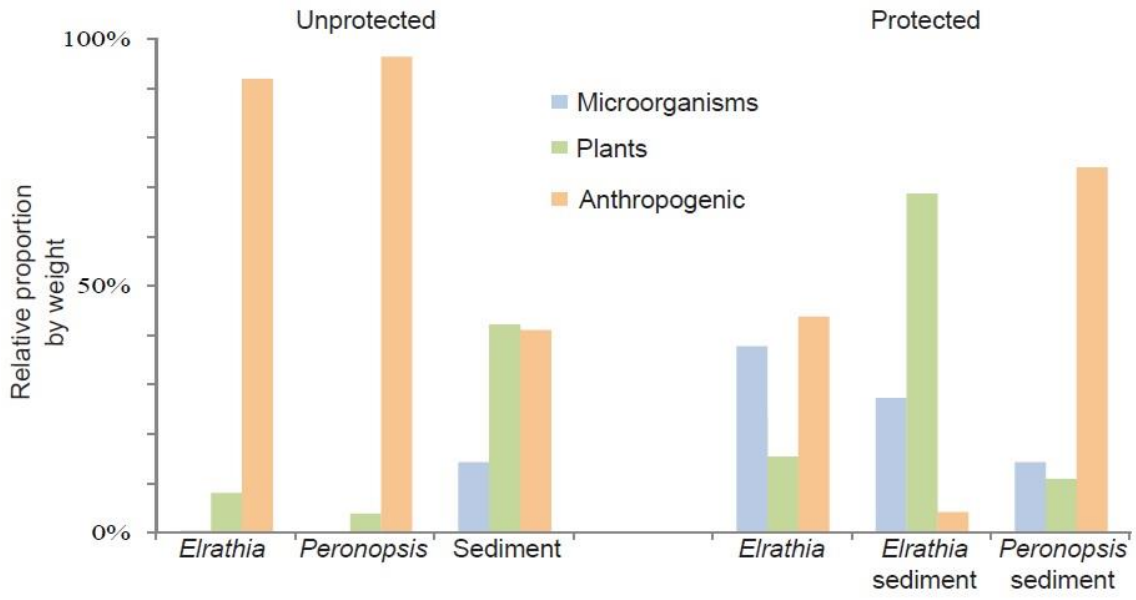

Fig. 3.3. Relative proportions of predominant biogenic and anthropogenic sources. Calculated from mean concentrations by weight of compound classes for protected and unprotected trilobite exoskeletons and associated sediment, and color coded by source type.

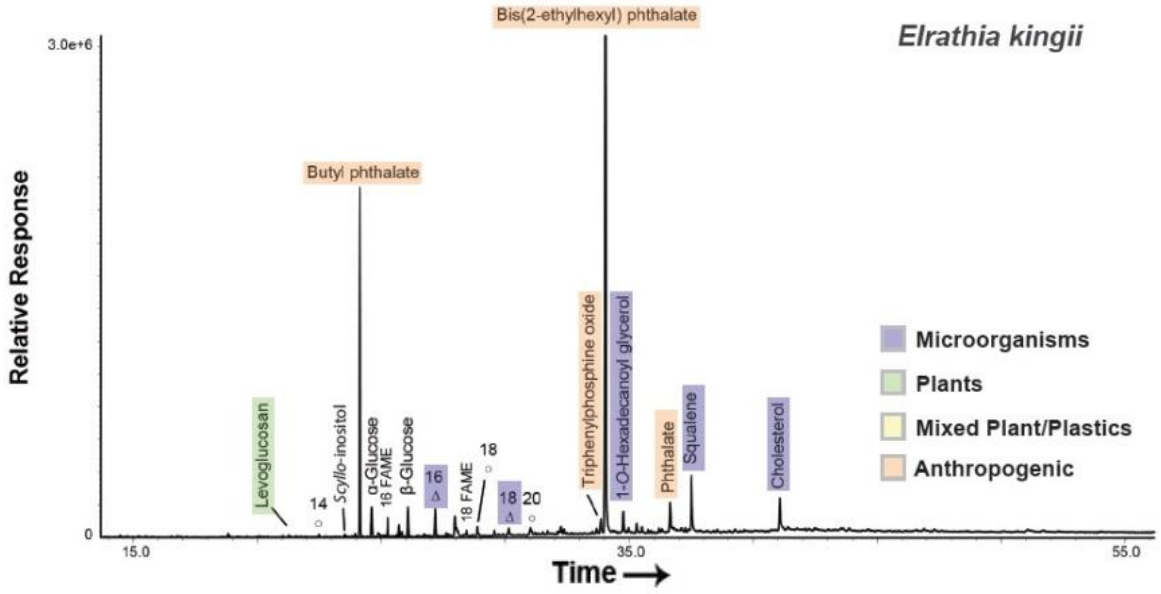

Fig. 3.4. GC-MS data for unprotected *Elrathia*. Total ion current (TIC) traces of extract (trimethylsilyl (TMS) derivatives). Numbers refer to the carbon chain length of homologous series (◦ = *n*-alkanol, Δ = *n*-alkanoic acid, FAME = fatty acid methyl ester).

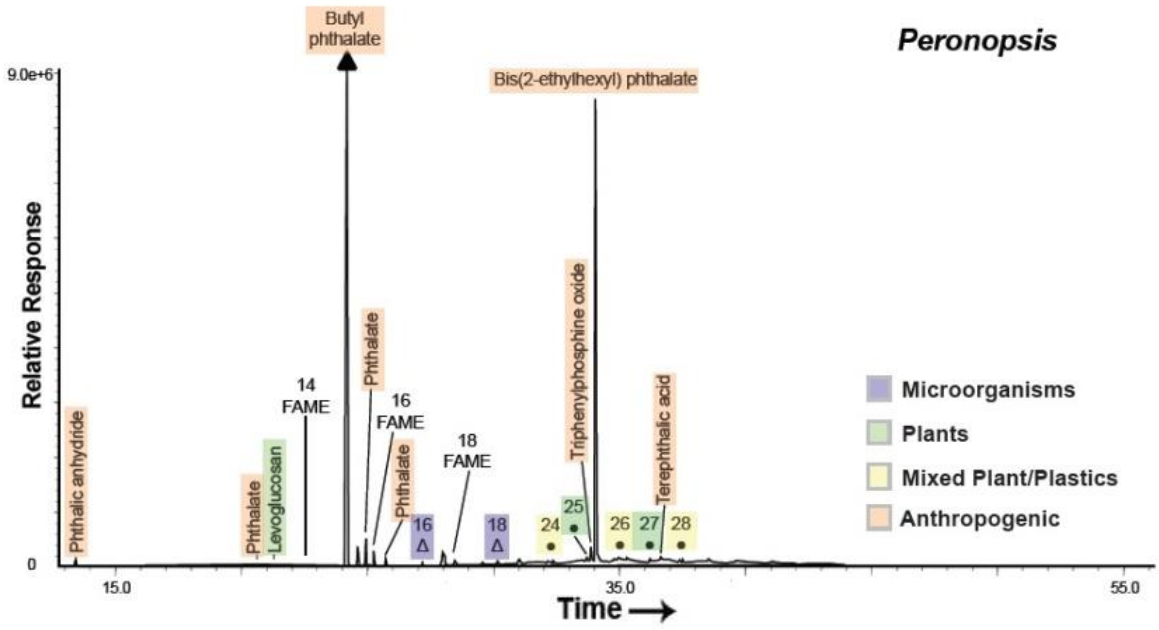

Fig. 3.5. GC-MS data for unprotected *Peronopsis*. Total ion current (TIC) traces of extract (trimethylsilyl (TMS) derivatives). Numbers refer to the carbon chain length of homologous series (• = *n*-alkane, Δ = *n*-alkanoic acid, FAME = fatty acid methyl ester).

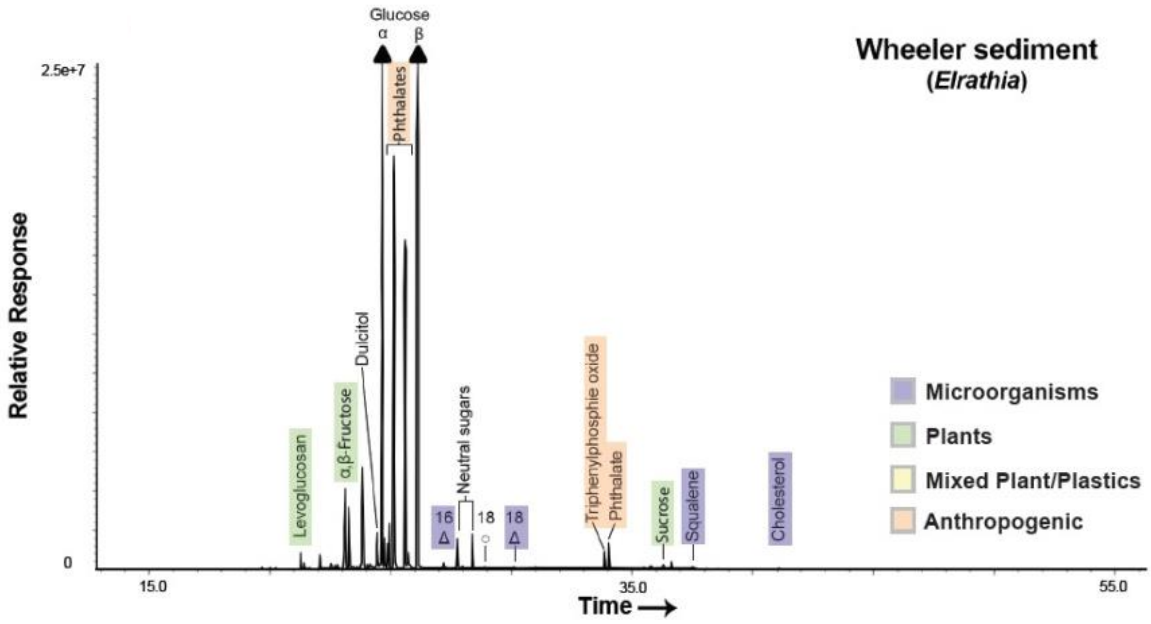

Fig. 3.6. GC-MS data for sediment associated with *Elrathia*. Total ion current (TIC) traces of extract (trimethylsilyl (TMS) derivatives). Numbers refer to the carbon chain length of homologous series (○ = *n*-alkanol, Δ = *n*-alkanoic acid).

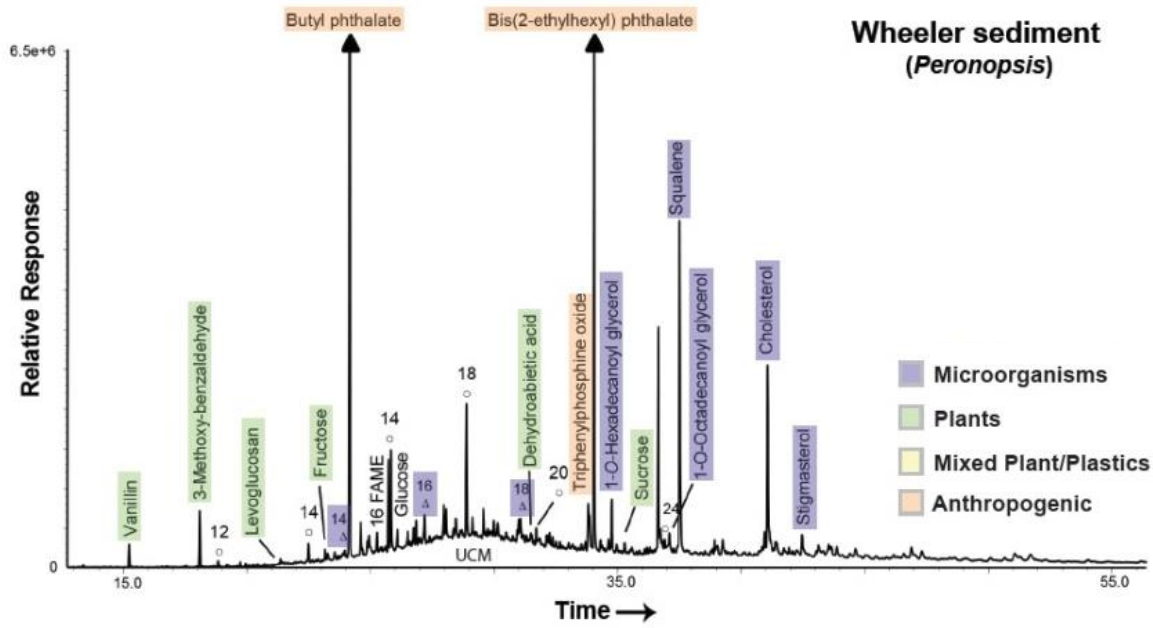

Fig. 3.7. GC-MS data for sediments associated with *Peronopsis*. Total ion current (TIC) traces of extract (trimethylsilyl (TMS) derivatives). Numbers refer to the carbon chain length of homologous series (◦ = *n*-alkanol, Δ = *n*-alkanoic acid, FAME = fatty acid methyl ester, UCM = unresolved complex mixture).

Table 3.1. Average concentrations (10^{-9}g g^{-1}) of chemical compounds for exoskeletons of *Elrathia* and *Peronopsis* and sediments associated with each species from the middle Cambrian, Wheeler Shale, Utah. Compounds are organized by source interpretation, then by chemical class with sum of averages for each class. Blue color indicates microorganism sources, yellow represents predominant plastic sources, green represents terrestrial plant sources, and orange represents anthropogenic compounds. Unprotected samples were collected and stored normally, while protected samples were explicitly collected without plastics or other chemical disturbance.

Chemical compounds	Source Interpretation	Unprotected samples			Protected samples		
		Elrathia	*Peronopsis*	Sediment	*Elrathia*	*Elrathia* sediment	*Peronopsis* sediment
Microorganism							
LMW (C ≤ 20) n-Alkanes							
Heptadecane	Microorganism	0.0	0.0	6.5	0.0	0.0	0.0
Octadecane	Microorganism	0.0	0.0	24.2	7.0	0.0	1.7
Nonadecane	Microorganism	0.0	0.0	24.6	0.0	0.0	0.0
Eicosane	Microorganism	0.0	0.0	5.7	0.0	0.0	4.3
Total Average		*0.0*	*0.0*	*61.0*	*7.0*	*0.0*	*6.0*
LMW (C ≤ 20) n-Alkanols							
Dodecanol	Microorganism	0.0	0.0	4.2	0.0	0.0	0.8
Tetradecanol	Microorganism	0.0	0.0	22.2	1.5	0.0	4.0
Eicosanol	Microorganism	0.0	0.0	0.0	0.0	0.0	2.5
Total Average		*0.0*	*0.0*	*26.4*	*1.5*	*0.0*	*7.3*
LMW (C ≤ 20) n-Alkanoic acids							
Nonanoic acid	Microorganism	0.0	0.0	2.2	0.0	0.0	0.0

Tridecanoic acid	Microorganism	1.3	0.0	0.0	0.0	0.0	0.0
Tetradecanoic acid	Microorganism	0.0	26.4	1.5	5.9	13.1	1.0
Hexadecanoic acid	Microorganism	0.0	0.0	0.0	430.4	1243.2	10.6
Octadecanoic acid	Microorganism	0.0	2.2	0.0	244.7	571.0	3.0
Total Average		*1.3*	*28.6*	*3.7*	*681.0*	*1827.3*	*14.6*
Sterols							
Cholesterol	Fauna/Algae	0.0	0.0	61.0	51.0	7.0	44.2
Stigmasterol	Flora/Algae	0.0	0.0	0.0	0.0	0.0	5.2
Sitosterol	Flora/Algae	0.0	0.0	5.1	0.0	0.0	0.0
Total Average		*0.0*	*0.0*	*66.1*	*51.0*	*7.0*	*49.4*
Glyceride derivatives							
Glycerol	Microorganism	0.0	0.0	4.3	0.0	0.0	0.0
1-*O*-Hexadecanoyl glycerol	Microorganism	0.0	0.0	17.7	15.9	0.0	6.5
1-*O*-Octadecanoyl glycerol	Microorganism	0.0	0.0	2.5	0.0	0.0	1.1
Total Average		*0.0*	*0.0*	*24.5*	*15.9*	*0.0*	*7.6*
Total Average Microorganism		**1.3**	**28.6**	**181.7**	**756.4**	**1834.3**	**84.9**
Plant							
HMW (C > 20) n-Alkanes							
Tetracosane	Plastic mix	48.0	215.1	0.0	0.0	0.0	0.0
Pentacosane	Plant	43.4	342.8	6.0	0.0	0.0	0.0
Hexacosane	Plastic mix	63.6	482.4	0.0	0.0	0.0	0.0
Heptacosane	Plant	45.8	410.4	0.0	0.0	0.0	0.0
Octacosane	Plastic mix	30.6	335.5	0.0	0.0	0.0	0.0
Nonacosane	Plant	25.1	226.6	0.0	0.0	0.0	0.0
Triacontane	Plastic mix	15.1	162.2	0.0	0.0	0.0	0.0
Total Average		*271.6*	*2175.0*	*6.0*	*0.0*	*0.0*	*0.0*
HMW (C > 20) n-Alkanols							
Docosanol	Plant	0.0	0.0	0.0	0.0	0.0	2.8

Tetracosanol	Plant	0.0	0.0	0.0	0.0	0.0	5.4
Hexacosanol	Plant	2.9	0.0	57.1	9.6	0.0	18.4
Octacosanol	Plant	7.1	0.0	26.7	9.9	0.9	23.0
Total Average		*10.0*	*0.0*	*83.8*	*19.5*	*0.9*	*49.6*
Saccharides							
Glucose	General biomass	0.0	0.0	233.0	274.2	3914.1	2.7
Fructose	Plant	0.0	0.0	0.0	0.0	560.3	0.0
Levoglucosan	Plant burning	0.0	48.6	2.4	1.8	15.7	1.2
Sucrose	Plant	0.0	0.0	189.8	14.0	22.5	2.1
Total Average		*0.0*	*48.6*	*425.2*	*290.0*	*4512.6*	*6.0*
Lignin derivatives							
3-Methoxy-benzaldehyde	Plant	0.0	0.0	0.0	0.0	0.0	8.2
Vanillin	Plant	0.0	0.0	1.4	0.0	0.0	3.9
Total Average		*0.0*	*0.0*	*1.4*	*0.0*	*0.0*	*12.1*
Diterpenoids							
Dehydroabietic acid	Conifer	0.0	0.0	3.0	2.8	1.0	2.5
Total Average Plant		**281.6**	**2223.6**	**519.4**	**312.3**	**4514.5**	**70.2**
Anthropogenic							
Amides							
Benzamide	Insect repellent	0.0	0.0	5.2	0.0	0.0	0.0
m-Toluamide	Insect repellent	0.0	0.0	4.2	0.0	0.0	0.0
Total Average		*0.0*	*0.0*	*9.4*	*0.0*	*0.0*	*0.0*
Organophosphines							
Tributylphosphine	Anthropogenic	9.2	23.8	0.0	0.0	0.0	0.0
Triphenylphosphine oxide	Flame retardant	722.3	710.9	10.1	35.0	14.1	15.4
Total Average		*731.5*	*734.7*	*10.1*	*35.0*	*14.1*	*15.4*
Plasticizers							
Terephthalic Acid	Plastics	0.0	58.7	23.1	0.0	0.0	0.0

Butyl phthalate	Plastics	1649.1	41349.9	185.7	197.1	45.1	204.7
Butyl hexyl phthalate	Plastics	36.4	934.3	138.8	48.6	36.1	52.6
Bis(2-ethylhexyl) phthalate	Plastics	714.4	13137.8	127.9	583.8	156.0	162.6
Phthalic Anhydride	Plastics	0.0	157.5	0.0	0.0	0.0	0.0
Total Average		*2399.9*	*55638.2*	*475.5*	*829.5*	*237.2*	*419.9*
Total Average Anthropogenic		**3131.4**	**56372.9**	**495.0**	**864.5**	**251.3**	**435.3**
% biogenic		8.29	3.84	58.62	55.28	96.19	26.27
		All unprotected: 23.58			**All protected: 65.84**		
% anthropogenic		91.71	96.16	41.38	44.72	3.81	73.73
		All unprotected: 71.42			**All protected: 34.16**		
CPI[a] for *n*-alkanes		0.7	0.8	-	-	-	-

[a]Carbon Preference Index: CPI = $(C_{23}+C_{25}+C_{27}+C_{29})/(C_{24}+C_{26}+C_{28}+C_{30})$.
Average values represent the mean of individual concentrations given in Table S1 for each type of protected and unprotected sample.

CHAPTER 4

DIAGENESIS AND ELEMENTAL CHEMISTRY OF EXCEPTIONALLY PRESERVED PUTATIVELY DYSOXIC TRILOBITES FROM THE WHEELER SHALE[1]

[1] John, D. J. and Walker, S. E. To be submitted to *Palaios.*

Abstract

Trilobites from the middle Cambrian Wheeler Shale, Utah, are exceptionally well preserved. A previous sedimentary model suggested that bacterial sulfate reduction acting on decaying trilobites led to cone-in-cone calcite (CIC) precipitation that buttressed the ventral side of the exoskeletons in early diagenesis. In addition to the sediments, it is quite possible that the exoskeletons themselves might hold geochemical and petrographic signatures consistent with this model. We examined two trilobite species, benthic *Elrathia kingii* and putatively pelagic *Peronopsis interstricta* to determine if they had different petrographic and geochemical signatures potentially reflecting their habitats prior to burial or if they had similar signatures indicative of early burial diagenesis. Similarly, we examined whether non-molted trilobites with presumably more organic carbon had different petrographic and geochemical signatures than molts and exoskeletal fragments. We found no textural differences in CIC between species or between molts and non-molted trilobites, but CIC was thinner on exoskeletal fragments, suggesting that organic carbon was diffuse throughout the sediment and exoskeletons acted as nucleation points for CIC. Low-pressure zones between sediment layers also seemed to play a role in governing CIC formation. Cone-in-cone calcite displaced compacted and cohesive sediment, indicating compaction preceded CIC precipitation. Cubic pyrite inclusions within CIC suggest low-organic carbon conditions, which favor cubic pyrite over framboidal, also must have preceded CIC formation. Elemental Ca, Mg, Fe and S compositions of both trilobite species' exoskeletons were similar, despite differences in their ecological habits, suggesting that original calcite compositions have been overprinted by diagenetic recrystallization. Low sulfur content

in all specimens suggests calcites precipitated under euxinic conditions. Calcite twins in the CIC indicate a thermal history between 170 and 200 °C. Our findings support previous interpretations of CIC formation under sulfate-reducing conditions, but suggest that CIC was governed by late diagenetic or low-grade metamorphic processes, in response to localized decreases in overburden pressure, increased temperatures, porewater diffusion transporting alkalinity, and favorable thermodynamics for the nucleation of calcite along exoskeletons.

Introduction

Fossils from the Wheeler Shale of southwestern Utah reveal an unusual taphonomic window into the middle Cambrian of Laurentia (Robison, 1971). In particular, the trilobites are thought to be relatively pristine, are very abundant in certain horizons and usually have characteristic cone-in-cone calcite (CIC) that underplates their exoskeletons (Walcott, 1908; Bright, 1959; Gaines and Droser, 2003; Brett et al., 2009). This unusual preservation is attributed to the physical and geochemical conditions of the Cambrian paleoenvironment. Depositional and preservational conditions of the Wheeler Shale bear similarities to the Burgess Shale (Briggs et al., 2008), which has been interpreted as greenschist-grade metamorphism based on evidence such as the presence of muscovite, lack of clays and reduced organic carbon (Powell, 2003). Gaines and Droser (2003) attribute the clay mineralogy in the Wheeler Shale to processes of burial diagenesis. However, the metamorphic history of the Wheeler Shale has not been examined, and changes in pressure and temperature conditions could play a role in the unique preservation of these trilobites.

Oxygen may also play a role in preservation. The Wheeler Shale environment has long been considered dysoxic (Bright, 1959; Brett et al., 2009). Cambrian atmospheric oxygen levels were slightly below modern averages (~<20% O_2; Berner et al 2003), while CO_2 levels were an order of magnitude higher (~4200 ppm, Bao et al., 2008; ~5000 ppm, Pörtner et al., 2004; cf. modern values ~400 ppm). Increased atmospheric CO_2 would have several effects on Cambrian ocean dynamics, such as increased temperatures that cause reduced seawater circulation and stratification of bottom waters, an increase in terrestrial weathering, particularly carbonate flux to the oceans, and a reduction in oxygen solubility in the ocean. However, fluctuations between anoxic, dysoxic, and fully oxic conditions likely occurred in the Wheeler Shale, affecting both the composition of the benthic community and their preservational pathways (Gaines and Droser, 2003; Gaines et al., 2005; Gaines and Droser, 2010). Throughout its ~100-150m thickness (Robison, 1964), the Wheeler Shale is divided into discrete anoxic, dysoxic, and oxic taphofacies, with different styles of preservation and different characteristic assemblages in each (Gaines et al. 2005). Burgess Shale-type soft body preservation was described in the anoxic facies. The dysoxic facies occurs primarily as thin beds, transitional from oxic to anoxic, abundant with the trilobites *Elrathia kingii* and *Peronopsis interstrictus*. In the dysoxic facies, where we focus in this study, Gaines et al. (2005) suggested that bacterial sulfate reduction of organic carbon in the sediment was constrained within trilobite exoskeletons, thereby facilitating the growth of CIC, enhancing trilobite preservation. Sedimentological and ichnofabric analyses corroborated their preservation model, but the fossils and CIC themselves have not been examined for direct evidence of either bottom-water dysoxia or porewater euxinia.

Petrographic analyses of trilobite exoskeletons can be used to test predictions about their preservational histories. First, Wheeler Shale trilobites are known to have recrystallized calcite (Gaines et al., 2005), consistent with early diagenesis in a carbonate-saturated environment. However, if their exoskeletons or CIC exhibit other diagenetic textures more suggestive of later processes, it might suggest a more complex diagenetic history that changes the interpretation of CIC formation. Associated pyrite can be used as an indicator of diagenetic timing and conditions, with framboidal pyrite representing sulfate-reducing conditions early in diagenesis, while cubic pyrite is more representative of late diagenesis in sediments with low organic carbon contents (Taylor and Macquaker, 2000). Second, if CIC is controlled primarily by the amount of bacterial sulfate-reduction, then it should be thicker on complete specimens (with abundant soft tissues) and thinner on molts or exoskeletal fragments that were buried with presumably less organic carbon. Lastly, CIC typically grows on the ventral surfaces of trilobite exoskeletons (Gaines et al., 2005), putatively in response to limited diffusion of porewaters. Therefore, if CIC grows on the dorsal surface where porewaters are not constrained, some other mechanism for CIC must be invoked.

The geochemistry of the exoskeletons and associated CIC can also reveal similarities and differences in preservation among trilobite species. We examined *Elrathia kingii*, a benthic trilobite, and *Peronopsis interstricta*, a putatively pelagic trilobite (Robison, 1971; the species has also been assigned to the genus *Itagnostus*; Naimark, 2012), to determine if their exoskeletons yielded different elemental geochemistries consistent with their life modes. Conversely, similar geochemistries among species and CIC would be consistent with diagenetic overprint of the original exoskeletal calcite in anoxic

sediments. We examined several elements (Fe, Mg, S, Ca, C and Si) to attempt to constrain their preservational modes. Iron and Mg were measured to constrain oxygenation: Mg is abundant and well-mixed through the oceans (Tipper et al., 2006), whereas Fe is more abundant in dysoxic benthic waters where it can accumulate by flux from dysoxic sediments (Salomons et al., 1987). A higher amount of Fe relative to Mg in exoskeletons would suggest that calcites precipitated in more dysoxic waters. Sulfur was also measured to indicate euxinia. Sulfate is common in oxic waters (Millero, 1974) and becomes incorporated into calcites (Burdett et al. 1989; Marenco et al., 2008), while in euxinic waters sulfate is reduced to sulfide which does not incorporate.

Calcites precipitated under euxinic conditions should show a lack of sulfur relative to oxic calcites (Marenco et al., 2008). Calcium concentrations indicate overall cation substitution, with lower Ca values representing greater cation substitution, a function controlled linearly by temperature and pressure (Stehli and Hower, 1961). Calcites with similar Ca values thus have similar overall substitution rates and their concentrations for other elements can be compared directly to one another. Silicon in calcites represents silicification, indicating diagenetic alteration. Carbon distributions were used to determine if there were regions of the trilobite with more abundant C (possibly representing soft-tissue structures such as the gut) that could influence CIC growth. Our work yields additional understanding of the pathways of preservation in the Wheeler Shale, confirming and expanding upon previous studies.

Methods

Elrathia kingii and *Peronopsis interstricta* and their surrounding sediments were obtained from commercial collectors (following Gaines and Droser, 2003). Samples were collected from fresh exposures in private quarries and represent multiple fossiliferous dysoxic horizons, though no specific stratigraphic context was recorded for specimens. Three whole and three molts (missing librigenae) of *E. kingii* and two whole *P. interstricta* (hereafter referred to as *Elrathia* and *Peronopsis*, respectively) were used for petrographic and geochemical analysis. Uncoated and polished petrographic thin sections representing longitudinal and transverse glabellar sections of *Peronopsis* and longitudinal and transverse glabellar and thoracic sections for *Elrathia* were used in petrographic thin section and geochemical analysis (Fig. 4.1). These sections allow for determination of average geochemical values that account for any heterogeneity in the exoskeletons. Petrographic analysis included observations examining the relationships between exoskeletons, CIC, and the surrounding sediment. Sediments in thin sections also contained fragments of trilobite exoskeletons that were examined where exposed. Thin sections were examined using a Leica DME petrographic microscope at 40-100x magnification. The number of specimens was determined by the best-preserved specimens; because of the lack of stratigraphic resolution, our samples may not be adequately representative of the overall dysoxic taphofacies.

To determine if *Elrathia* and *Peronopsis* exoskeletons preserved signatures of their original seawater chemistries, and thus had different geochemical signatures than associated diagenetic CIC, their elemental chemistry was examined. After petrographic analysis, the thin sections were carbon-coated and analyzed on a JEOL JXA 8600

Superprobe electron microprobe with wavelength-dispersive X-ray spectroscopy (WDS), which yields data to a precision of 0.01 weight percent. Elemental weight percent was determined for Fe, Mg, Ca, and S within the cephalic, thoracic, and pygidial regions of the trilobite exoskeletons, CIC, and associated sediments to constrain seawater oxygenation and possible euxinia. Data were averaged within those three sample types and by species and molt status. Forty-four point sample zones approximately 5-10 μm wide were analyzed for 60 to 90 seconds with one to three analyses performed on each point. Additional analysis time did not substantially increase detection limits. Precisions as measured using a C.M. Taylor Calcite standard were ±0.04 for Ca, ±<0.01 for Mg, ±0.06 for Fe, and ±0.01 for S. Average approximate detection limits were 0.03 weight percent for Ca, 0.03 for Mg, 0.11 for Fe, and 0.01 for S. All data were above detection limits except for S.

Elemental maps provide additional data about distributions of elements in trilobite exoskeletons than point analyses alone provide. Elemental maps were made for S, Si, and Ca on the electron microprobe using energy-dispersive X-ray spectroscopy (EDS), across sections that had sediment, exoskeleton, and CIC in close association, to differentiate between sulfides, siliciclastics, and calcium carbonates, respectively. Relative depletion or enrichment of S between sample groups might suggest those samples formed under differing conditions of euxinia. Silicon in the CIC and exoskeleton would indicate either inclusions of siliceous sediment suggesting deformation of the exoskeleton or silicification of the original calcite indicating diagenetic alteration.

One specimen each of non-molted *Peronopsis* and *Elrathia* were used in carbon elemental mapping using an environmental scanning electron microscope (ESEM), because carbon cannot be examined on the electron microprobe, where specimens are carbon-coated. Carbon concentrations could represent the vestiges of soft tissues associated with microbially-mediated CIC precipitation, or variations in the organic carbon content of the sediment. Trilobites were cleaned of surficial sediment and dried at 70 °C overnight before ESEM analysis. Dorsal exoskeletons were mapped using energy-dispersive X-ray spectroscopy (EDS) on a Zeiss 1450SP ESEM. Elemental maps and SEM backscatter images were obtained for the cephalon, thorax, and pygidium for both species.

Total organic carbon for the sediments was determined by subtracting total inorganic carbon from total carbon. Total carbon was determined by powdering a total of 25 sediment samples associated with both trilobite species in a Spex 8000 ball mill to produce approximately 20 ml of powdered sediment. 100 mg of these powders were weighed into a crucible boat and fired on an Eltra furnace to 1350°C under a pure oxygen atmosphere. The resultant carbon dioxide was measured by infrared absorption on an Eltra CS500 determinator to yield the total weight percent carbon in the sample. Total inorganic carbon was then determined by weighing another 100 mg of the same sample powder into a 250 ml flask and mixing with 10 ml of ethanol, then connecting the flask to an Eltra CS500 determinator, adding 10 ml of 20% HCl and heating to 50°C, and measuring the resultant carbon dioxide as above. Total organic carbon values were averaged by species. Carbon and inorganic carbon analysis was performed at the Lyons Lab at UC Riverside, and are the same as described in Chapters 2 and 5.

Results

Petrographic Analysis of Exoskeletons, Cone-in-cone Calcite and Sediment

Both *Elrathia* and *Peronopsis* exoskeletons had the same basic composition: a thin (~10-25 μm), mostly calcitic exoskeleton (with minor silica replacement, see next section) (Fig. 4.2A). Cone-in-cone calcite projected usually from the ventral surface, but grew also from the upper surface of exoskeletons (Fig. 4.2B-C). Crystals of CIC were often optically continuous on both sides of exoskeletons, indicating the crystals were genetically related and grew outward from the same nucleation site, i.e. the exoskeleton (Fig. 4.2B-C).

Cone-in-cone calcite is also associated with trilobite exoskeletal fragments (Fig. 4.3). These fragments had CIC growth considerably thinner (mean thickness 0.34 mm) than articulated trilobites (mean thickness 2.46 mm). Additionally, CIC growth occurred on either side of the trilobite fragment (Fig. 4.3A–B).

Exoskeletons generally exhibited little deformation, but one *Elrathia* specimen's pleural segments were deflected downward under the adjacent pleurae and into the CIC, suggesting lateral compression (Fig. 4.4A). Separate CIC crystals fill the space above and below the deflected pleurae, and a third also partially separates the exoskeleton from sediments deflected down alongside it.

Microstylolites are also found in some specimens (Fig. 4.4A) These structures form when increased pressure drives dissolution and remobilization of carbonate and concentrates insoluble phases such as clays along irregular wavy margins (Wanless, 1979). Crystals of CIC contained calcite twins (Fig. 4.4B). These twins are typically widely-spaced thin twins, though some cones may have more developed twinning with

densely-packed thick twins. Sparse thin twinning is indicative of lower-temperature deformation of the calcite, with a maximum thermal history of ~170 °C, while thick tabular twins indicate slightly higher temperatures up to 200 °C (Ferrill et al., 2004; Rybacki et al., 2013). Series of bedding-parallel fractures can be found in the CIC (Fig. 4.4).

Cone-in-cone calcite also contained sulfides as cubic crystals that did not interrupt the CIC structure (Figs. 4.5A-B). Elemental analysis of these inclusions using WDS showed a stoichiometry of FeS_2, suggesting they are pyrite or marcasite.

The sediment surrounding both *Peronopsis* and *Elrathia* was a mix of siliciclastic clays and fine-grained carbonates that is foliated roughly parallel to bedding (Fig. 4.6). Sediment was cohesive and responded to stress by deforming plastically, not through brittle fracturing or shearing through layers. Cone-in-cone calcite underneath trilobite exoskeletons deflected nearby sediment and grew laterally outward between the deflected sediment layers (Fig. 4.7). Foliations in the sediment are bedding-parallel except under CIC growth, where foliations were sheared and rotated downward under the CIC crystal (Fig. 4.7A). Foliated layers remained discrete and continuous through the zone of shearing, indicating sediments were coherent but not fully lithified prior to CIC growth. Individual sigmoidal or banded crystals of CIC grew in the shear zone between the rotated sediment horizons (Figs. 4.7A-B). Microstylolites were observed, as previously described for Fig. 4.4A, that indicated pressure dissolution of CIC calcite under vertical strain.

Elemental Geochemistry of Exoskeletons, Cone-in-cone Calcite, and Sediment

The geochemistry of the exoskeletons, CIC, and sediment indicated the similarities and differences in preservational histories. Broadly, the elemental compositions of the exoskeleton and CIC were similar (Table 4.1).

Mean Ca exoskeletal and CIC values for non-molted *Peronopsis*, non-molted *Elrathia,* and molted *Elrathia* were similar. Wilcoxon rank-sum tests revealed that Ca values were not significantly different between exoskeletal groups ($p = 0.965$, df = 18, W=41 between *Peronopsis* and molted *Elrathia*; $p = 0.108$, df = 19, W=64 between *Peronopsis* and non-molted *Elrathia*; $p = 0.223$, df = 21, W=73 between non-molted and molted *Elrathia*; $\alpha = 0.05$). Exoskeleton Ca for all three groups was likewise not significantly different from associated CIC values ($p = 0.267$, df = 10, W=13 for *Peronopsis*; $p = 0.343$, df = 15, W = 30 for non-molted *Elrathia*; $p = 0.121$, df = 12, W = 18 for molted *Elrathia;* $\alpha = 0.05$).

Iron and magnesium were slightly more concentrated in exoskeletons (mean 0.47 wt. % and 0.49 wt. %, respectively) than in CIC (mean 0.27 wt. % and 0.16 wt. %, respectively; Table 4.1; Fig. 4.8). Those differences were not found significant by Wilcoxon rank-sum test for Fe ($p = 0.118$, df = 37, W = 159) but were significantly different for Mg ($p << 0.001$, df = 37, W=221). Sulfur was at or below detection limits (0.01 wt. %) for 32 of the 44 samples, and of the remaining twelve, only six were more than 0.02 wt. % (Fig. 4.8; Appendix 4.1).

Within the exoskeletons, molted *Elrathia* had the most Mg (mean 0.63 wt. %) compared to non-molted *Elrathia* (mean 0.49 wt. %); non-molted *Peronopsis* had the least (mean 0.31 wt. %; Table 4.1). However, Fe had higher values in *Peronopsis* (mean

0.59 wt. %) compared to non-molted *Elrathia* (mean 0.45 wt. %), while molted *Elrathia* had the least Fe (mean 0.38 wt. %; Table 4.1; Fig. 4.8). A Wilcoxon rank-sum test indicated molted *Elrathia* and *Peronopsis* exoskeletons were significantly different for Mg ($p < 0.001$, df = 18, W = 77), while non-molted *Elrathia* and *Peronopsis* exoskeletons were significantly different for Fe ($p = 0.016$, df = 19, W = 73).

Sediment composition was a mix of carbonates and siliciclastics, in contrast to the relatively pure calcite of the CIC and exoskeletons, and thus showed markedly different overall average values for Ca, Fe, and Mg (Fig. 4.8; Table 4.1). However, the heterogeneity of the sediment also suggests that the small sample size may not describe the overall variation of sediment well enough for confident statistical analysis.

Electron microprobe EDS elemental maps of both non-molted *Elrathia* (Fig. 4.9A-B) and *Peronopsis* (Fig. 4.9C-D) exoskeletons indicated partial silicification of the exoskeleton in isolated locations; silicification is uncommon (< 5% of overall exoskeleton calcite of all types within the 8 thin sections examined) and generally restricted to patches of a few hundred μm. Under ESEM mapping, carbon had no zonation that could be attributed to distributions of soft tissue either within or around the exoskeleton, but only followed the difference between the more calcareous exoskeleton and less calcareous sediment (Fig. 4.10)

Total organic carbon (as measured in Ch. 5) was 0.35% and 0.33% by weight, respectively, for sediment associated with *Elrathia* and *Peronopsis*.

Discussion

The exceptional preservation in the Wheeler Shale has been described as a function of its sedimentology, oxygenation, and the chemical changes associated with bacterial sulfate reduction (Gaines and Droser, 2003). Wheeler Shale is described as a fluctuating environment with repeating progressions among anoxic facies with finely laminated sediment with soft-body preservation, dysoxic facies with monotypic, high-density assemblages of *Elrathia* with *Peronopsis* in weakly bioturbated sediment, and fully oxic facies with more diverse but sparse assemblages of trilobites in bioturbated sediments (Gaines and Droser, 2003). After burial, reservoirs of porewater conducive to CIC precipitation formed under trilobite exoskeletons, where sulfate reduction of organic carbon in dysoxic sediments drove changes in the local geochemistry, enhancing the occlusion of surrounding pore space and isolation of the trilobites and leading to CIC formation and exceptional preservation.

We evaluated these sedimentological and paleoecological interpretations with petrographic and geochemical data. We explored how the sedimentary, CIC, and exoskeletal records describe the controls on CIC precipitation and the paleoenvironmental and diagenetic conditions under which the trilobites were preserved.

Controls on Cone-in-Cone Precipitation

Our findings suggest that physical constraint of porewater alone cannot explain all the textures seen in the CIC. Rather, sediment may not have been completely occlusive to porewater flow, and geochemical gradients would not be totally contained by trilobite exoskeletons. This is consistent with experimental results that show tightly packed clays

can still allow ionic diffusion at rates of cm per month (Oscarson, 1994). Tightly-packed, deflocculated clays are part of the Gaines et al. (2005) pore-occlusion model for CIC formation, though diffusion at the rates found by Oscarson (1994) would be sufficient to carry alkalinity away from exoskeletons as it formed. Sediment also demonstrated evidence of plastic deformation where CIC growth deflected it, which suggests intergranular space was not completely sealed with authigenic cements.

While trilobite exoskeletons and sclerites may have provided some partial barrier to upward diffusion, their exoskeletons may have also provided a nucleation template that would have facilitated CIC growth. Such a mechanism has been described experimentally, where calcite crystals provide an effective seed site for nucleation of calcite from solution, and the growth rate from supersaturated fluids is dependent on the degree of supersaturation (Lioliou et al., 2007). In sediments where BSR was ubiquitous, fluids could be somewhat concentrated by retardation of upward diffusion under trilobite exoskeletons, and become more supersaturated. Additionally, the cohesive, laminated sediment and bedding-parallel fractures and microstylolites in the CIC suggest it was formed after compaction, with a component of vertical stress. Microstylolites in particular indicate a vertically oriented stress sufficient to cause calcite to undergo pressure dissolution and loss of CIC material.

Twinning in the CIC indicates thermal stress: thermal alteration as high as 200 °C produced thick twins, though most twins were thin twins that only suggest a thermal maximum of 170°C. The thermal history of the CIC is likely close to the 200 °C threshold, enough to begin partially developing thick twins but not completely lose thin-twinned textures. Additionally, the concentration of twins in the lower part of CIC

structures (which is the oldest CIC, as it expands downward from the precipitation surface along the trilobite carapace; Seilacher, 2001) suggests that CIC may have precipitated under high-temperature conditions. Older CIC near the bottom of encrustations would have more time to develop well-defined twins. Concave-downward exoskeletons could have partially distributed these stresses outward, creating a lower-pressure zone under the carapace more conducive to CIC formation. Combined with a favorable site for nucleation, these factors could generate thicker growth of CIC than on dorsal surfaces (Fig 4.11).

Conversely, thickness of encrustations was similar between molted and non-molted specimens, while those of disarticulated sclerites were markedly thinner. Non-molted trilobites would presumably be buried with abundant soft tissue, though exuviae may still have had some soft-tissue membranes buried along with the carapace, as they do with some modern ecdysozoans (Gaban and Farley, 2002). The similarity between molted and non-molted trilobites suggests that the organic carbon driving bacterial sulfate reduction and CIC formation was ubiquitous in the sediment and not dependent on buried trilobite soft tissue; this supports the interpretation that CIC formation was driven by the mobilization of alkaline fluids throughout the sediment and subsequent precipitation along trilobite exoskeletons that provide a template for nucleation.

Cubic sulfide inclusions suggest a later diagenetic history for the CIC. Cubic pyrite is more typical of porewaters in low-organic carbon sediments with reduced bacterial sulfate reduction, while high-organic carbon sediments in the sulfate reduction zone typically form framboidal pyrite (Taylor and Macquaker, 2000).

Biomarker data suggests that the Wheeler Shale has been weathered by recent oxic groundwater (see Chapter 3), and any sedimentary pyrite likely oxidized, while inclusions in the CIC were protected from weathering. These inclusions preserve a record of conditions during CIC formation that suggests CIC may have formed later in diagenesis, in less organic-rich sediment that was under more compaction, consistent with the interpretation of pressure textures and the low organic carbon content measured in the sediment. Pressure-mediated CIC precipitation between sedimentary beds along CIC margins, stylolites within CIC, and horizontal fracture systems in CIC all suggest that CIC formation occurred under a significant vertical stress component.

Sediment Competence during Cone-in-Cone Formation

The relationships between CIC and sediments were consistent with CIC growth before sediment was fully cemented. Durrance (1964) demonstrated that CIC crystallization could deform surrounding uncemented sediments, a process described for CIC from several locations worldwide by Cobbold et al. (2013). In the Wheeler Shale, deformed-yet-discrete laminations where CIC growth deflected sedimentary layering suggested the sediment was cohesive and compacted prior to CIC nucleation. Bedding-parallel foliations are deflected by CIC, indicating foliation of sediments preceded CIC formation. This is consistent with mechanisms described by Seilacher (2001) for forming sandwich concretions in CIC sulfides. Growth in uncohesive sediments, where strain could not be propagated, would result in cleanly sheared rather than deformed layers. Growth in fully lithified sediments would cause brittle rather than plastic deformation of sedimentary layers. Bedding-parallel fractures in the CIC suggested that compaction

continued to deform the sediment and fossils after CIC precipitation as well. A consistent vertical stress during CIC formation is also suggested by the interbedded sigmoidal CIC between sediment layers in the shear zone along the CIC margin. Shearing and rotation of the sediment beds by CIC growth would lead to vertical extension, rather than compression, where sedimentary layers were rotated, creating a zone of reduced vertical strain. Reduced pressures facilitate CIC nucleation from pore fluids and growth along sediment horizon surfaces.

Cone-in-cone intergrown with laterally compressed and deflected thoracic pleurae of *Elrathia* also supported precipitation of CIC in cohesive, compacted sediments. The CIC crystals are not continuous through the deflected pleural section, suggesting deflection of the exoskeleton occurred first during compaction and CIC subsequently grew both above and below the deflected pleurae (Fig. 4.4A). Cone-in-cone also appears to have grown between the deflected pleurae and part of the sediment originally attached to the exoskeleton. This wedge of CIC matches up optically with the CIC underneath but not above, suggesting the ventral crystal underneath grew upwards on the dorsal side and separated the sediment from the exoskeleton.

Calcite interbedded with sediment along the fossil margins indicated that CIC growth was controlled by pressure shadows between layers of sheared sediment, and indicating some diffusion of alkaline porewaters. A reduction in pressure increases the saturation state of carbonate-rich pore fluids and thus is conducive to CIC formation (Brown, 1954; Cobbold et al., 2013). As the main CIC grew downward and displaced the nearby cohesive sediment, sediment layers directly underlying the CIC would be compressed vertically, while the layers lying to either side of the CIC would be rotated

and sheared donwards by the corners of the CIC, deforming plastically and extending parallel to bedding. The decreased vertical pressure in these areas could trigger CIC formation along bedding planes, as is seen in the sediments near the CIC margins.

Interpreting Differences in Elemental Chemistry

The elemental chemistry of the exoskeletons was more consistent with diagenetic calcites than with original exoskeletal material. If skeletons were original, benthic *Elrathia* should originally reflect bottom-water conditions, which are interpreted as dysoxic to euxinic in the Wheeler Shale (Gaines and Droser, 2003; Brett et al., 2009). Conversely, *Peronopsis* has traditionally been associated with a pelagic mode of life in shallow waters (Jago, 1973), though recent work has questioned if some agnostids had a benthic mode of life (Esteve and Zamora, 2014). In the Wheeler Shale, the occurrence of *Peronopsis* across multiple benthic taphofacies is consistent with a pelagic interpretation for the agnostids (Robison 1971; Gaines and Droser 2003). *Peronopsis* thus should reflect more oxic water-column conditions, if exoskeletons were original. However, our data suggest that there were no major differences in chemistries between either species of trilobite and CIC. This suggests that trilobite exoskeletons are diagenetically altered and no longer reflect original seawater compositions, but rather reflect diagenetic porewater chemistry; this interpretation is also supported by the partial silicification seen in some exoskeletons and partial dolomitization of the sedimentary calcite reported previously (Gaines et al., 2005). The minor elemental differences seen between CIC, *Elrathia* and *Peronopsis* could reflect small-scale variations in porewater chemistry, or variations in

recrystallization during diagenesis. Thus, both exoskeletal and CIC chemistry indicates diagenetic porewater conditions.

Sulfur likewise was consistent with the anoxic, sulfate-reducing conditions that were expected during CIC formation. Sulfur was below detectable limits on the electron microprobe point analyses for most sites measured. Anoxic or euxinic conditions in the sulfate reduction zone would be expected to decrease dissolved free sulfate as it reduces and drives precipitation of sulfidic phases such as authigenic pyrite. Calcites precipitated under euxinic conditions (i.e., diagenetic calcites) should thus have less associated sulfate. The overall low concentrations of sulfur, below detection limits for both trilobites and CIC, meet those predictions. Oxidation of sedimentary sulfides to iron oxides (as evident by Recent meteoric groundwater alteration; see Ch. 3) might account for a loss of sulfur in the sediment, though sulfur associated with fossil calcite would be more protected from oxidation, as the sulfide inclusions were, suggesting the lack of sulfur seen in exoskeletons and CIC is original and reflective of anoxic porewater conditions.

Conclusion

Trilobites in the Wheeler Shale exhibit excellent preservation, due in part to CIC encrustations formed under exoskeletons (Bright, 1959). This CIC was generated by a combination of concentrating supersaturated fluids, creating negative pressure zones and providing sites on exoskeletons conducive to calcite nucleation. Cone-in-cone deformed and grew within surrounding sediments, indicating precipitation of structures in unlithified but cohesive and compacted sediment under vertical stress. It was less well-

developed under trilobite fragments, suggesting complete trilobites created conditions more favorable for CIC development, possibly through more pronounced supersaturation of alkalinity. Conversely, CIC was found on both molted and complete specimens, indicating that abundant associated soft tissue was not prerequisite for CIC generation, as supposed by previous work (Bright, 1959; Gaines et al., 2005). Rather, CIC was generated from alkaline fluids that diffused under carapaces, generated by sulfate reduction throughout the sediments. Elemental compositions suggested that exoskeletal calcite has been replaced and represents subsurface diagenetic conditions, rather than preserving original seawater conditions. Geochemical signals from diagenetic calcites are consistent with anoxic conditions conducive to bacterial sulfate reduction within the sediment. However, inclusions of cubic pyrite in CIC suggest sulfate reduction driving CIC precipitation was not extremely active and localized under trilobite exoskeletons early after burial. Rather, sulfate reduction was diffuse in the sediment and created alkaline pore fluid that nucleated CIC along trilobite exoskeletons. Textures and structures in the CIC such as stylolites, pressure-mediated precipitation zones, and thick and thin twinning suggest that CIC formed under elevated temperature and pressure conditions more consistent with late diagenesis or low-grade metamorphism.

References

Bao, H., Lyons, J.R., and Zhou, C., 2008, Triple oxygen isotope evidence for elevated CO_2 levels after a Neoproterozoic glaciation: Nature, v. 453, p. 504-506.

Berner, R.A., Beerling, D.J., Dudley, R., Robinson, J.M., and Wildman, R.A. Jr., 2003, Phanerozoic atmospheric oxygen: Annual Review of Earth and Planetary Sciences, v. 31, p. 105-34.

Brett, C.E., Allison, P.A., DeSantis, M.K., Liddell, W.D., and Kramer, A., 2009, Sequence stratigraphy, cyclic facies, and lagerstätten in the Middle Cambrian Wheeler and Marjum formations, Great Basin, Utah: Palaeogeography, Palaeoclimatology, Palaeoecology, v. 277, p. 9-33.

Briggs, D.E., Lieberman, B.S., Hendricks, J.R., Halgedahl, S.L., and Jarrard, R.D., 2008, Middle Cambrian arthropods from Utah: Journal of Paleontology, v. 82, p. 238-254.

Bright, R.C., 1959, A paleoecologic and biometric study of the Middle Cambrian trilobite *Elrathia kingii* (Meek): Journal of Paleontology, v. 33, p. 83-98.

Brown, R.W., 1954, How does cone-in-cone material become emplaced?: American Journal of Science, v. 252, p. 372-376.

Burdett, J.W., Arthur, M.A., and Richardson, M., 1989, A Neogene seawater sulfur isotope age curve from calcareous pelagic microfossils: Earth and Planetary Science Letters, v. 94, p. 189-198.

Cobbold, P.R., Zanella, A., Rodrigues, N., and Løseth, H., 2013, Bedding-parallel fibrous veins (beef and cone-in-cone): worldwide occurrence and possible significance in terms of fluid overpressure, hydrocarbon generation and mineralization: Marine and Petroleum Geology, v. 43, p. 1-20.

Durrance, E.M., 1967, Photoelastic stress studies and their application to a mechanical analysis of the tertiary ring-complex of Ardnamurchan, Argyllshire: Proceedings of the Geologists' Association, v. 78, p. 289-318.

Esteve, J. and Zamora, S., 2014, Enrolled agnostids from the Cambrian of Spain provide new insights about the mode of life in these forms: Bulletin of Geosciences, v. 89, p. 283-291.

Gaban, R.D. and Farley, R.D., 2002, Ecdysis in scorpions: supine behavior and exuvial ultrastructure: Invertebrate Biology, v. 121, p. 136-147.

Gaines, R.R. and Droser, M.L., 2003, Paleoecology of the familiar trilobite *Elrathia kingii*: an early exaerobic zone inhabitant: Geology, v. 31, p. 941-944.

Gaines, R.R. and Droser, M.L., 2010, The paleoredox settings of Burgess Shale-type deposits: Palaeogeography, Palaeoclimatology, Palaeoecology, v. 297, p. 649-661.

Gaines, R.R., Kennedy, M.J., and Droser, M.L., 2005, A new hypothesis for organic preservation of Burgess Shale taxa in the middle Cambrian Wheeler Formation, House Range, Utah: Palaeogeography, Palaeoclimatology, Palaeoecology, v. 220, p. 193-205.

Jago, J.B., 1973, Cambrian agnostid communities in Tasmania: Lethaia, v. 6, p. 405-421.

Lioliou, M.G., Paraskeva, C.A., Koutsoukos, P.G., and Payatakes, A.C., 2007, Heterogeneous nucleation and growth of calcium carbonate on calcite and quartz: Journal of Colloidal and Interface Science, v. 308, p. 421-428.

Marenco, P.J., Corsetti, F.A., Kaufman, A.J., and Bottjer, D.J., 2008, Environmental and diagenetic variations in carbonate associated sulfate: an investigation of CAS in the

Lower Triassic of the western USA: Geochimica et Cosmochimica Acta, v. 72, p. 1570-1582.

Millero, F.J., 1974, The physical chemistry of seawater: Annual Review of Earth and Planetary Sciences, v. 2, p. 101-150.

Naimark, E.B., 2012, Hundred species of the genus *Peronopsis* Hawle et Corda, 1847: Paleontological Journal, v. 46, p. 945-1057.

Oscarson, D.W., 1994, Surface diffusion: is it an important transport mechanism in compacted clays?: Clays and Clay Minerals, v. 42, p. 534-543.

Pörtner, H.O., Langenbuch, M., and Reipschläger, A., 2004, Biological impact of elevated ocean CO_2 concentrations: lessons from animal physiology and Earth history: Journal of Oceanography, v. 60, p. 705-718

Powell, W., 2003, Greenschist-facies metarmorphism of the Burgess Shale and its implications for models of fossil formation and preservation: Canadian Journal of Science, v. 40, p. 13-25.

Robison, R.A., 1971, Additional Middle Cambrian trilobites from the Wheeler Shale of Utah: Journal of Paleontology, v. 45, p. 796-804.

Rybacki, E., Evans, B., Janssen, C., Wirth, R., and Dresen, G., 2013, Influence of stress, temperature, and strain on calcite twins constrained by deformation experiments: Tectonophysics, v. 601, p. 20-36.

Salomons, W., De Rooij, N.M., Kerdijk, H., and Bril, J., 1987, Sediments as a source for contaminants?: Hydrobiologia, v. 149, p. 13-30.

Seilacher, A., 2001, Concretion morphologies reflecting diagenetic and epigenetic pathways: Sedimentary Geology, v. 143, p. 41-57.

Stehli, F.G. and Hower, J., 1961, Mineralogy and early diagenesis of carbonate sediments: Journal of Sedimentary Petrology, v. 31, p. 358-371.

Taylor, K.G., and Macquaker, J.H.S., 2000, Early diagenetic pyrite morphology in a mudstone-dominated succession: the Lower Jurassic Cleveland Ironstone Formation, eastern England: Sedimentary Geology, v. 131, p. 77-86.

Tipper, E.T., Galy, A., Gaillardet, J., Bickle, M.J., Elderfield, H., and Carder, E.A., 2006, The magnesium isotope budget of the modern ocean: constraints from riverine magnesium isotope ratios: Earth and Planetary Science Letters, v. 250, p. 241-253.

Walcott, C.D., 1908, Cambrian Geology and Paleontology: Cambrian Sections of the Cordilleran Area with Ten Plates: Smithsonian Miscellaneous Publications, v. 53, p. 107-130.

Wanless, H.R., 1979, Limestone response to stress: pressure solution and dolomitization: Journal of Sedimentary Petrology, v. 49, p. 437-462.

Figures and Tables

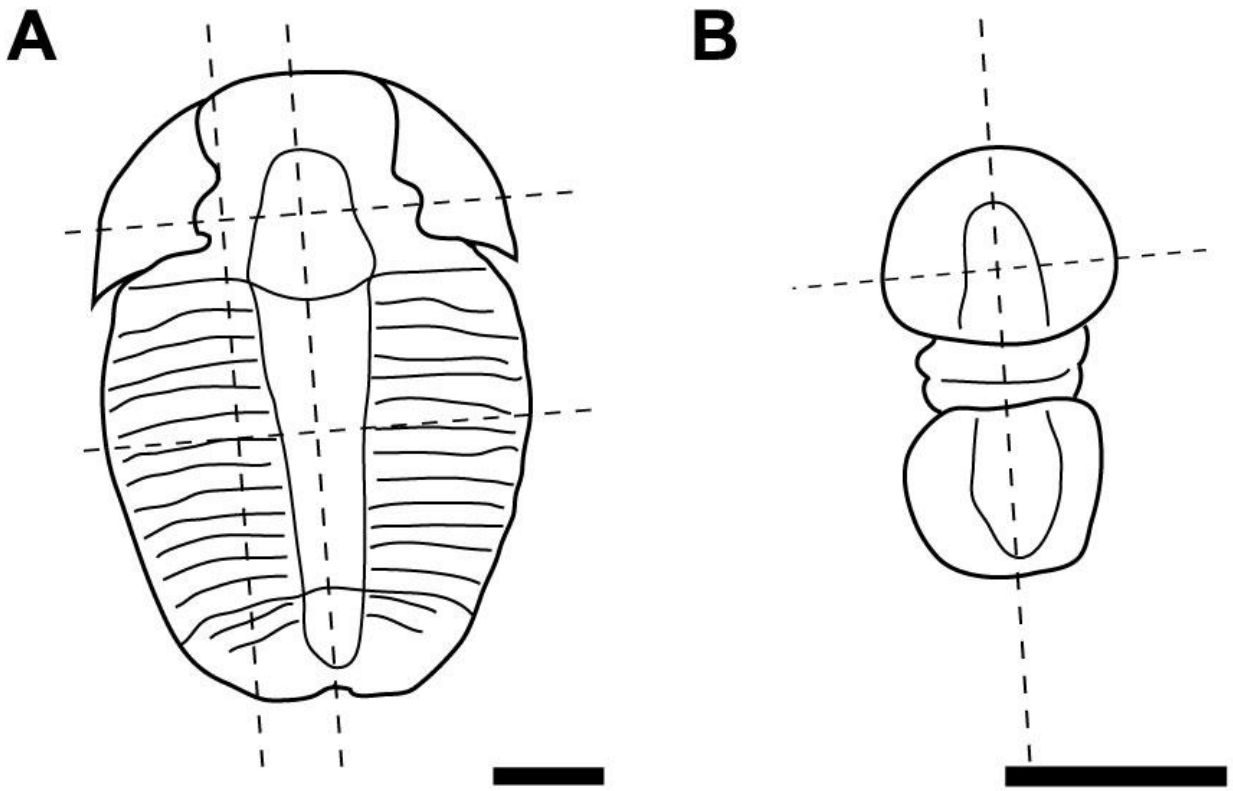

Figure 4.1. Diagrams of cross sections through trilobites for petrographic analysis. A) *Elrathia kingii*, showing longitudinal axial and abaxial sections, and transverse glabellar and thoracic sections. B) *Peronopsis*, showing longitudinal and transverse glabellar sections. Scale bars = 0.5 cm.

Figure 4.2. Cross sections of non-molted trilobites with CIC under petrographic microscope. A) *Peronopsis* longitudinal section along central axis showing exoskeleton with CIC projecting from the ventral surface and uninterrupted growth of cones (crossed polars, composite image). B) *Peronopsis,* transverse glabellar section. Arrows indicate position of glabellar furrows where CIC is growing on the dorsal surfaces. C) *Elrathia*, pleural section, with calcite cones projecting from concave ventral surfaces. Arrows indicate interpleural furrows where CIC also grows on the dorsal surface.

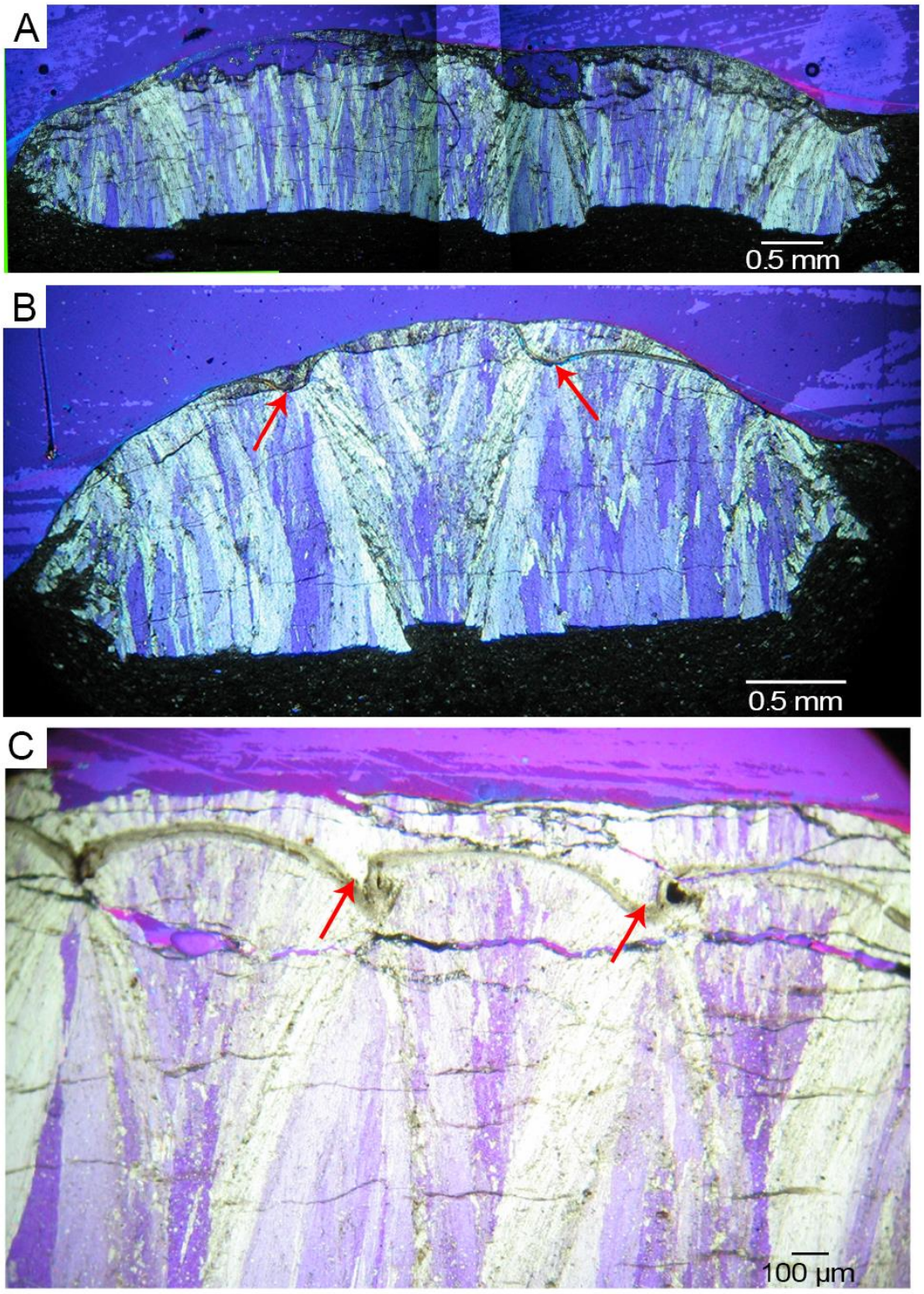
A
0.5 mm
B
0.5 mm
C
100 µm

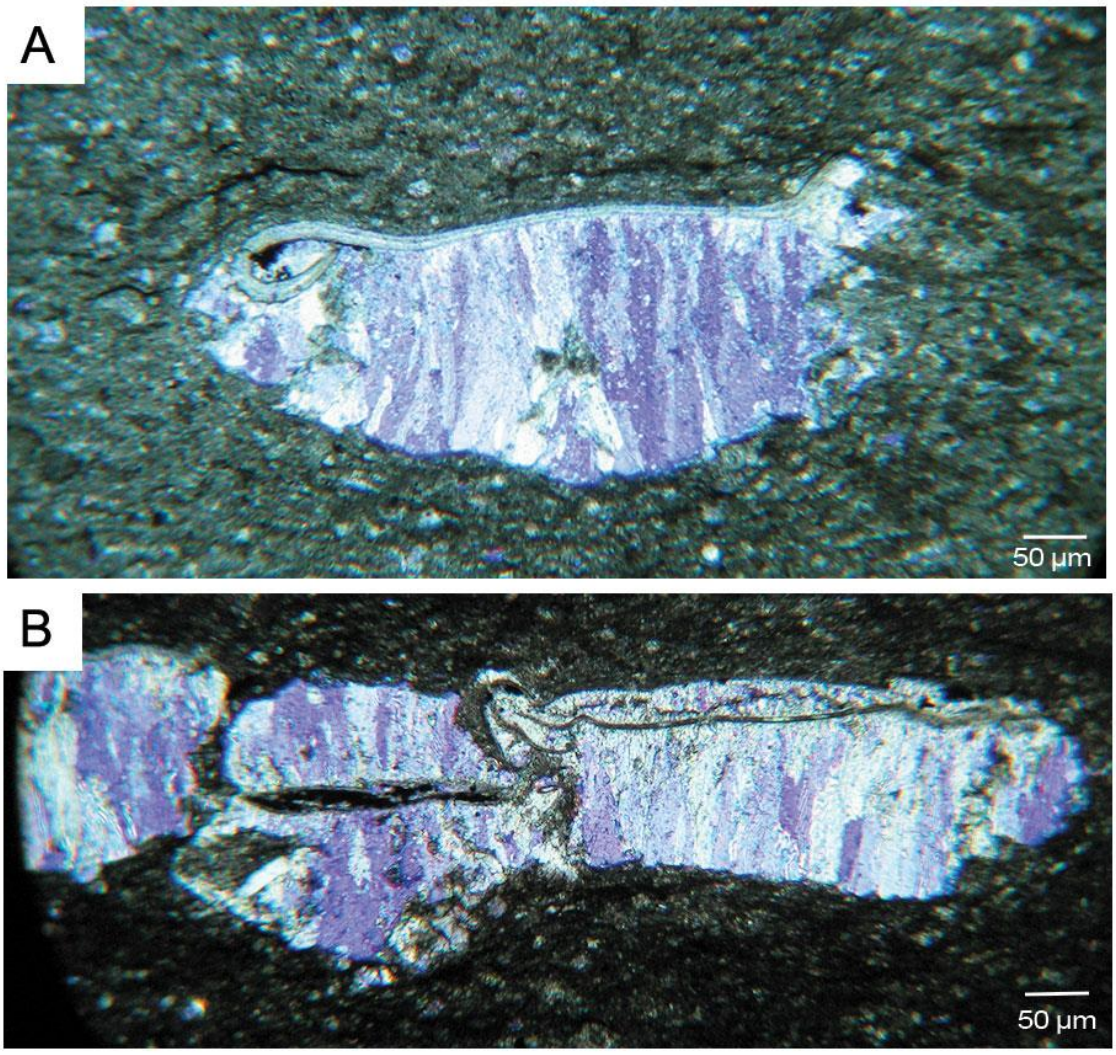

Figure 4.3. Disarticulated sclerite fragments buried alongside *Peronopsis* under petrographic microscope. Cone-in-cone growth is considerably thinner than non-molted trilobites. A) Sclerite with bottom-only CIC growth. B) Sclerite with top-and-bottom CIC growth.

4

Figure 4.4. Pleural exoskeleton of non-molted *Elrathia.* A) Downward deflection of several pleurae under burial compression, under petrographic microscope (composite image). Arrows show the position and direction of deflected exoskeleton with associated sediment (1), and the separation of sediment (2) and exoskeleton (3) by subsequent growth of CIC. Cone-in-cone crystallography is discontinuous above and below (2) but continuous across (3), indicating that CIC grew independently underneath both layers of exoskeleton, but also partially grew along the dorsal surface of the deflected pleurae, displacing the sediment upwards. Stylolites (4) indicate pressure solution of CIC under vertical strain. B) Calcite twinning at bottom of CIC. Primarily, CIC contains widely spaced thin twins, similar to twins on the left of image, characteristic of lower temperatures (<170 °C) and pressures, though infrequently denser-packed thick twins such as those on the right are observed, indicating slightly higher temperatures (170-200 °C; Ferrill et al., 2004). Scale bar = 0.25 mm.

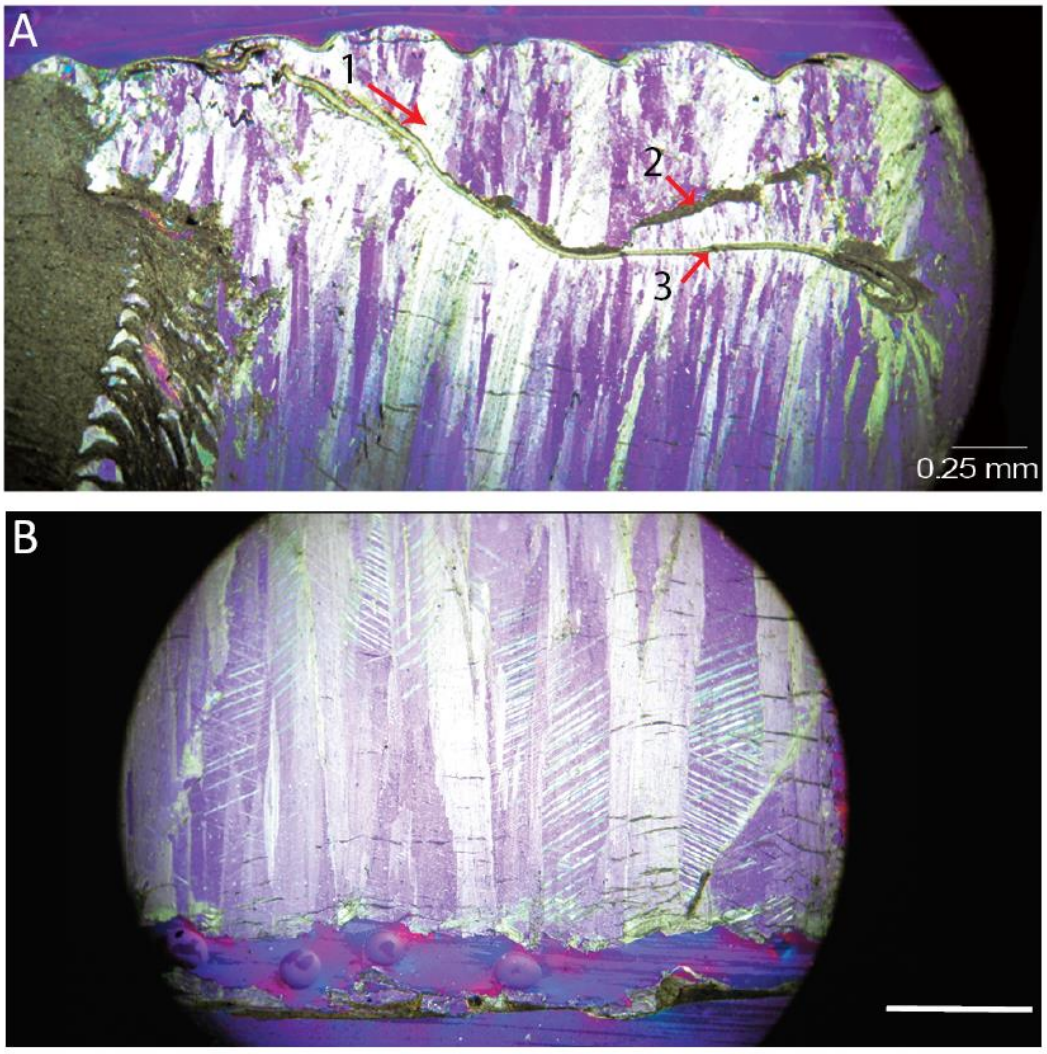
A
1
2
3
0.25 mm
B

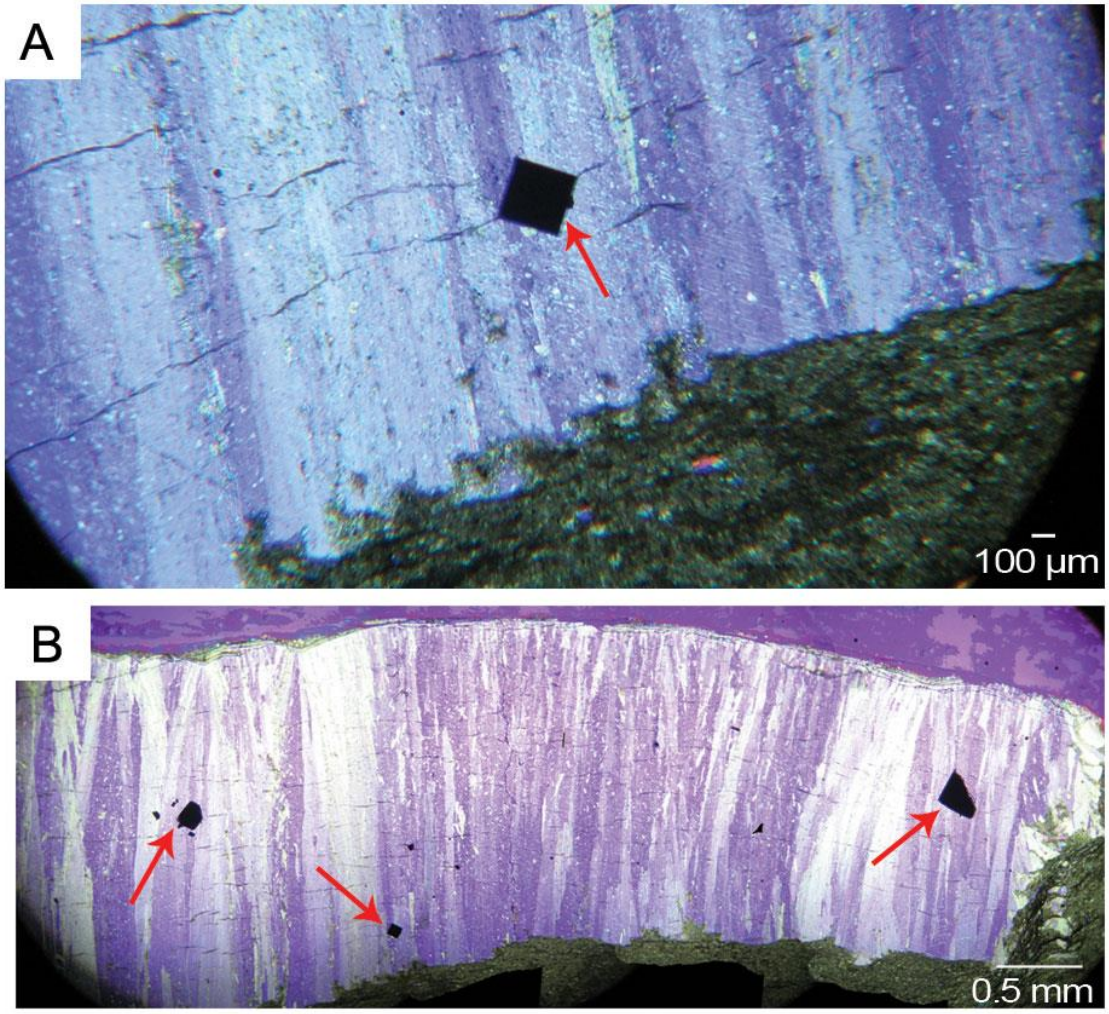

Figure 4.5. Sulfides associated with fossils and CIC under petrographic microscope. A) Cubic-sulfide crystal within *Elrathia* CIC. B) Cubic sulfide grains distributed through CIC of *Elrathia*, composite image.

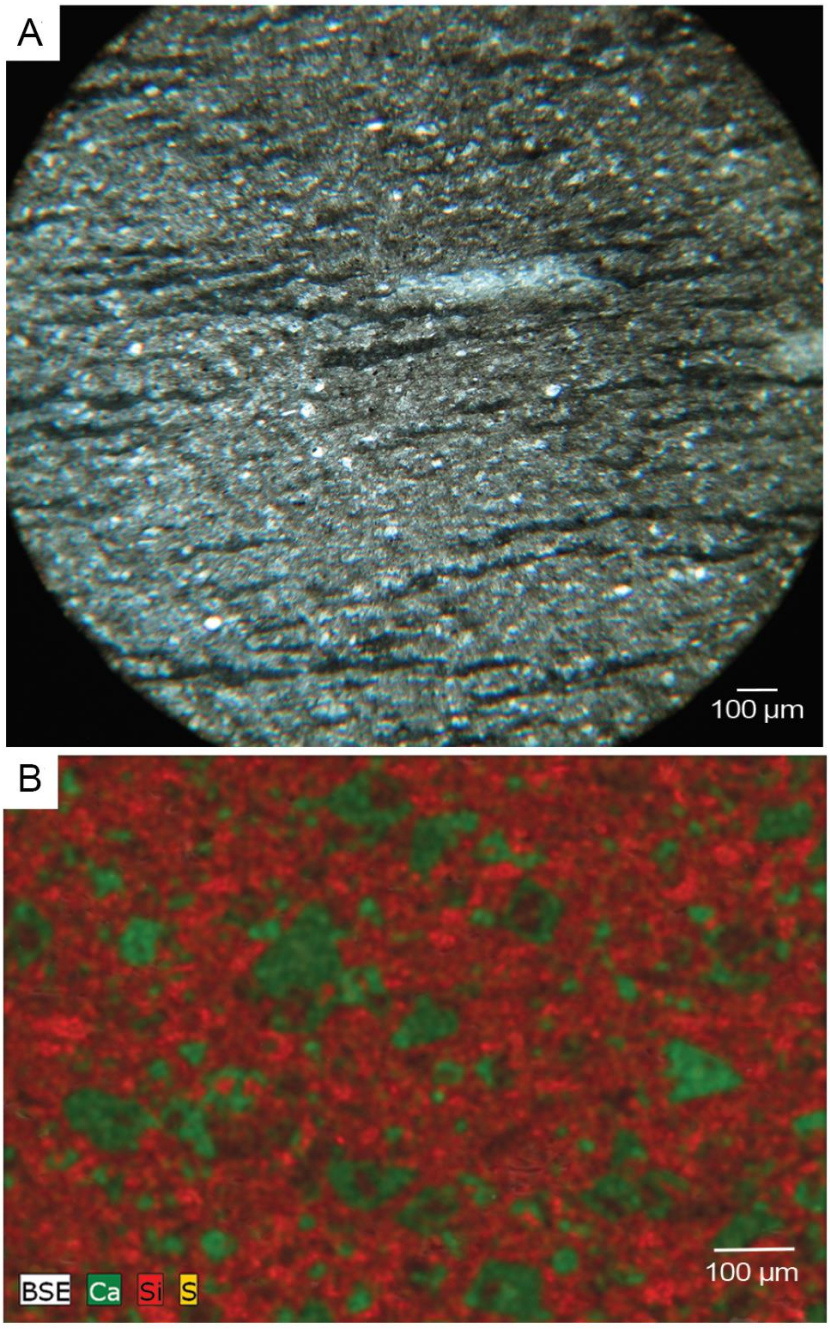

Figure 4.6. Texture and composition of sedimentary matrix. A) Sediment micrograph showing bright carbonate grains and gray siliciclastic clays, with bedding-parallel foliation. B) Microprobe EDS elemental map of sediment indicating mixed carbonate-siliciclastic composition. BSE=backscatter electron image, Ca=Calcium, Si=Silicon, S=Sulfur.

Figure 4.7. Deformation of sediment around fossil margins of *Elrathia* under petrographic microscope. A, B) Cone-in-cone intergrown with nearby compacted and cohesive sediment, which is deflected downward by CIC growth. Foliations remain distinct where deformed, indicating cohesive deformation of the sediment. Cone-in-cone beds intergrown with sedimentary layers suggest growth is mediated by low-pressure zones where shearing created vertical extension, reducing stress from compaction. Specimen figured in A) is same as in Fig. 4.4A and contains the microstylolites described there, indicating pressure dissolution of CIC carbonate in response to vertical strain.

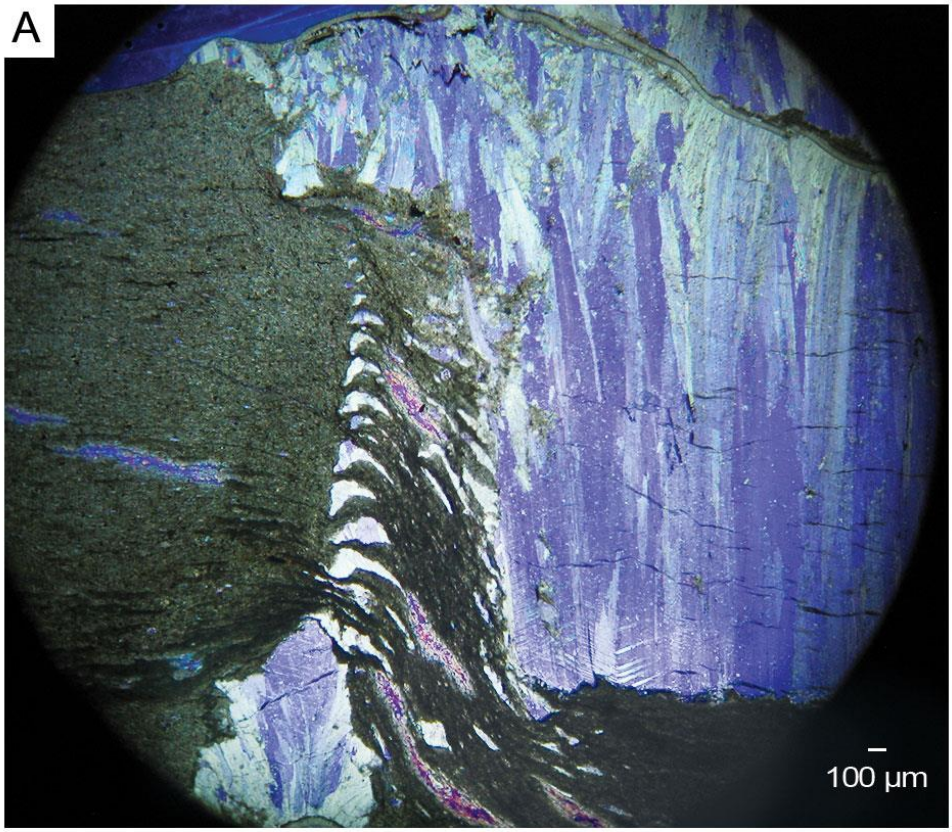
A
100 µm

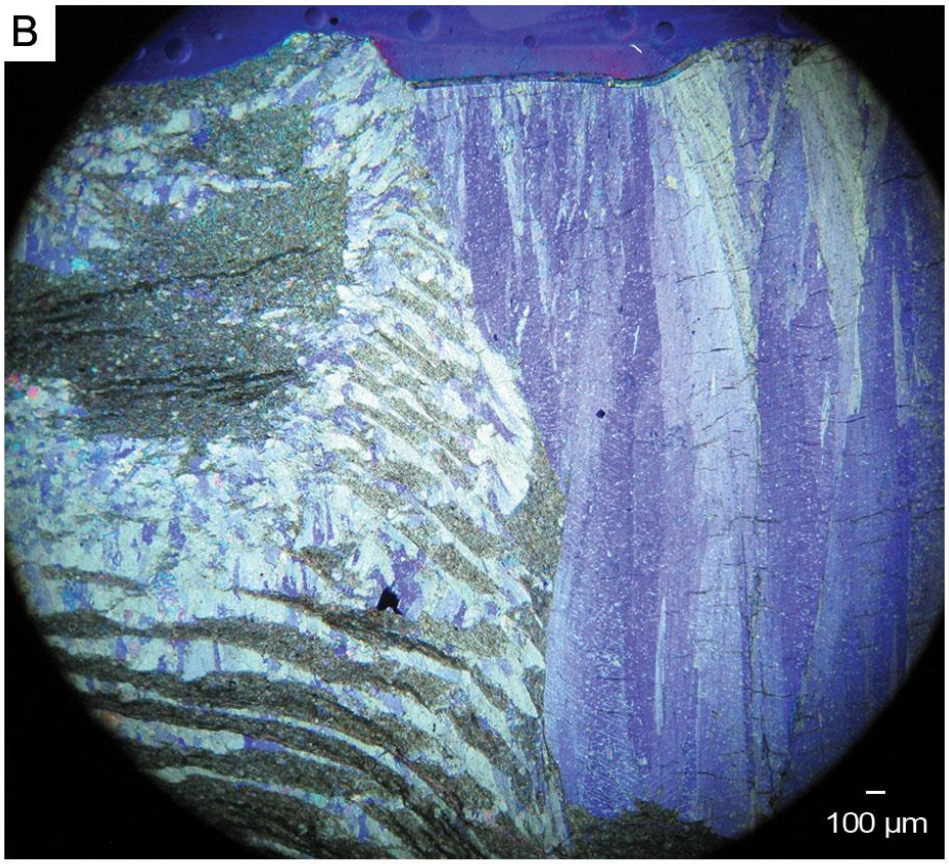
B
100 µm

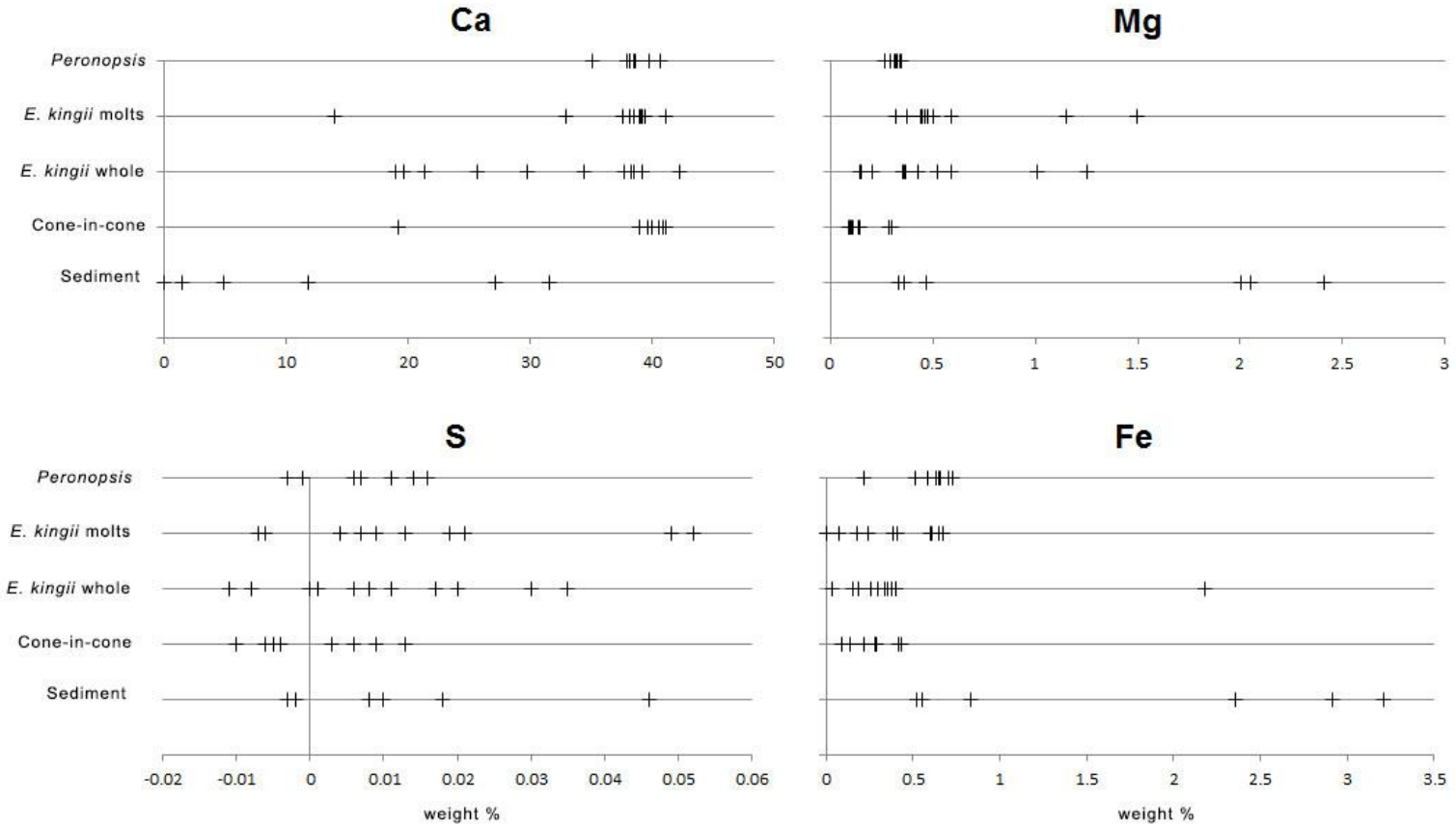

Figure 4.8. Graphical depiction of data in Table 4.1. Weight percentages of Ca, Mg, S, and Fe for each sample type: whole *Peronopsis* exoskeletons, molted and whole *Elrathia kingii* exoskeletons, CIC, and sediment. Sulfur values were at or below detection limits for most specimens.

Figure 4.9. Silicification of exoskeletal calcite. BSE=backscatter electron image, Ca=Calcium, Si=Silicon, S=Sulfur. A) *Elrathia* thoracic pleurae and deflected exoskeleton within CIC, photomicrograph. Arrows point to exoskeleton along surface (1), and inclusions of silicon-rich sediment within CIC structure (2-3). B) Microprobe EDS elemental map of area in A. Partially silicified exoskeleton and sediment inclusions are distinct from calcium in exoskeleton and CIC. C) *Peronopsis*, glabellar section, photomicrograph. Arrow points to exoskeleton between layers of CIC along glabellar furrow. D) Microprobe EDS elemental map of area in C. Exoskeleton is partially silicified between layers of CIC.

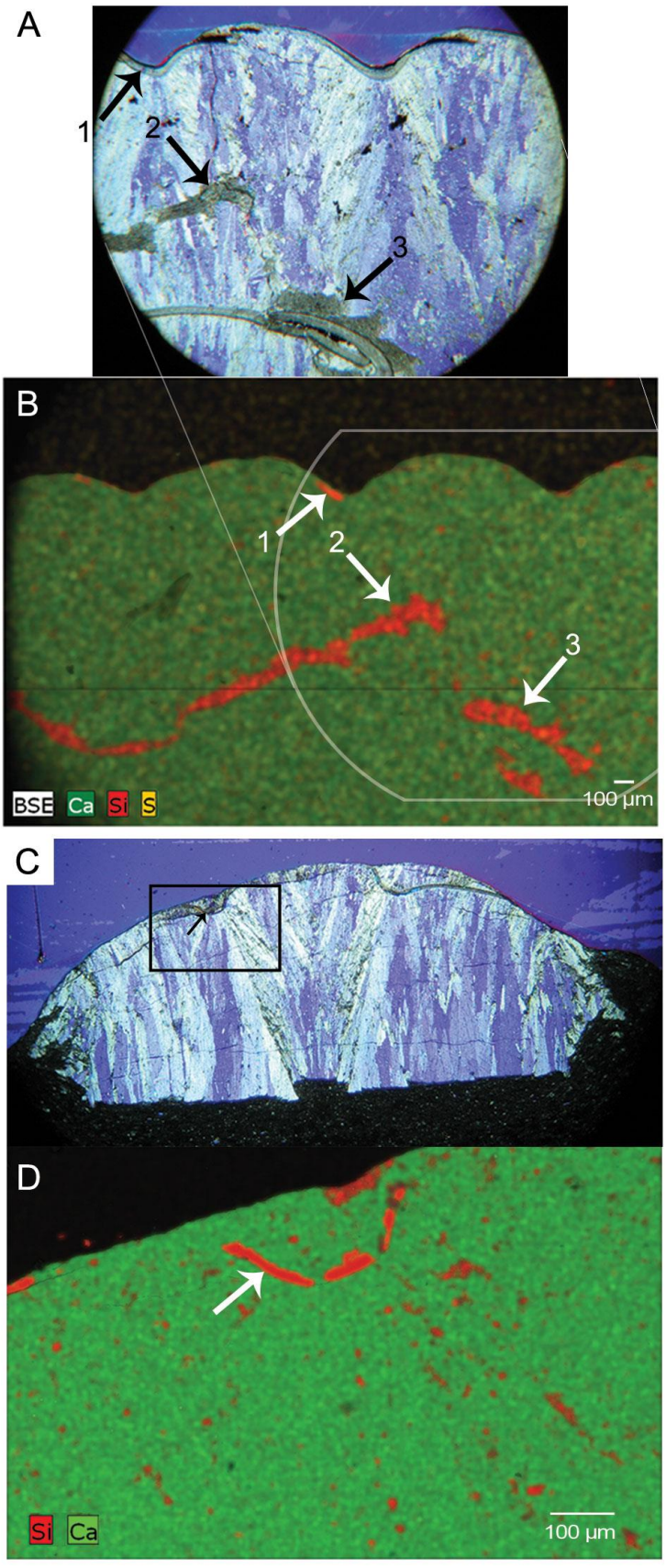
A
1
2
3
B
1
2
3
BSE
Ca
Si
S
100 µm
C
D
Si
Ca
100 µm

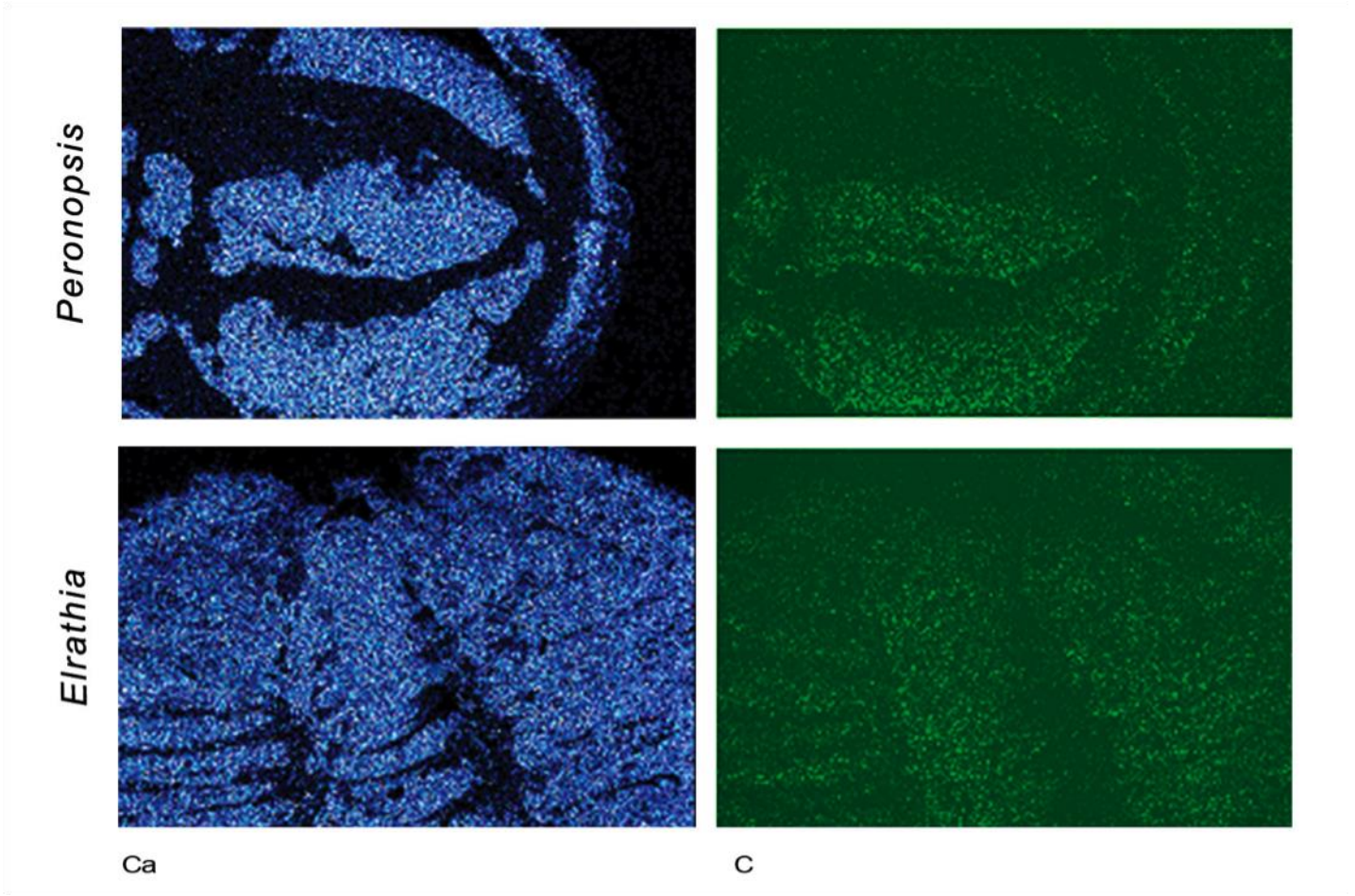

Figure 4.10. Carbon and calcium distributions under ESEM EDS elemental map. For both *Peronopsis* and *Elrathia*, carbon concentration does not appear to represent any soft tissue structures, but appears wherever carbonate exoskeleton, as indicated by the Ca distribution, is exposed.

Figure 4.11. Schematic of preservational pathway in Wheeler Shale. A) Life position. *Elrathia* inhabits the benthos while *Peronopsis* is pelagic. B) Post death and early diagenesis, a trilobite exoskeleton is buried, but conditions are not yet sulfur-reducing. C) Late diagenesis, compaction and heating begin, generating laminations in the sediment. The sediment becomes cohesive, but remains plastic. Bacterial sulfate reduction commences, forming cubic pyrite. D) Sulfate reduction has generated enough alkalinity to reach supersaturation. Porewaters diffuse upwards into carapace, concentrating and nucleating CIC along the ventral surface. Some nucleation may also occur on the dorsal surface. Exoskeleton recrystallizes to diagenetic calcite. E) Cone-in-cone continues to grow downward, displacing sediment layers. Additional CIC grows between displaced sediment layers where pressure from compaction is relieved. Pyrite inclusions become entrained in CIC. F) Late diagenesis to low-grade metamorphism. Compaction continues to compress trilobites, generating brittle fractures and microstylolites in CIC perpendicular to strain. Sediment becomes more lithified. G) Recent weathering. Oxic meteoric groundwater weathers the sediment, oxidizing any sedimentary pyrite. Inclusions of pyrite remain protected.

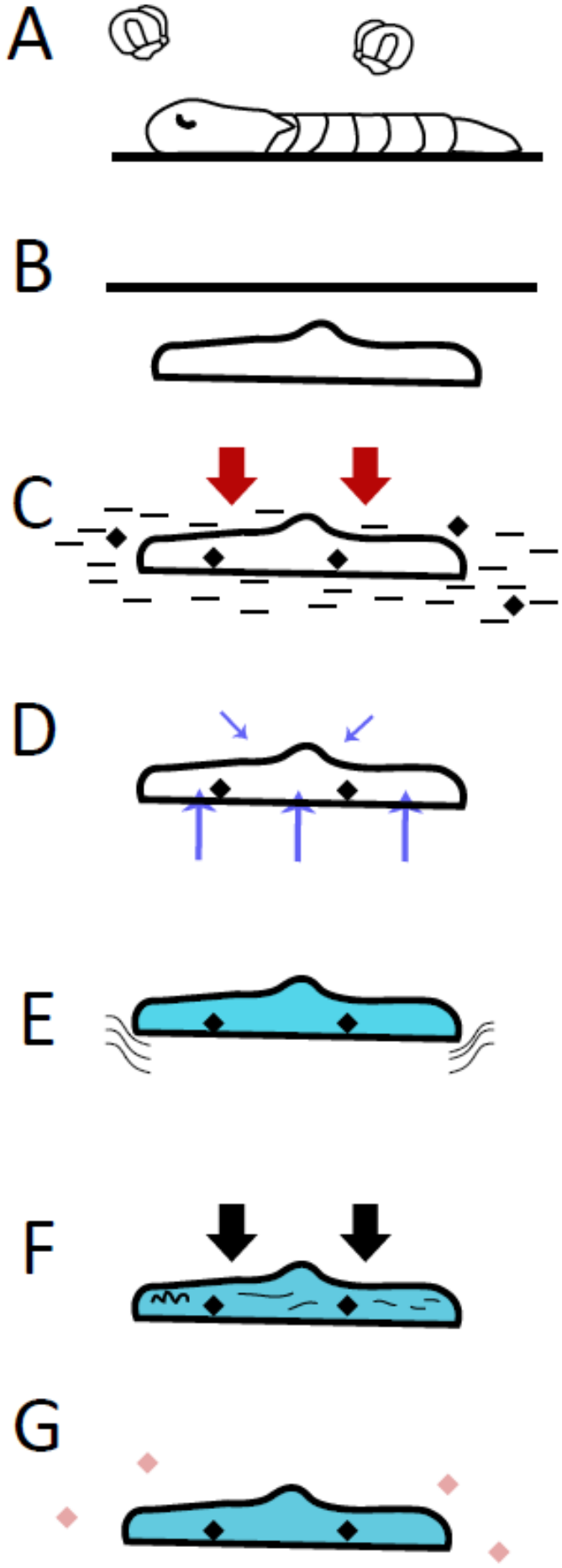
A
B
C
D
E
F
G

Table 4.1. Mean elemental weight percentages for different sample types under microprobe WDS analysis. Ca, Mg, Fe, and S average values are given for *Peronopsis* exoskeletons and associated CIC and sediment, for *Elrathia kingii* molted and whole specimens with associated CIC and sediment and for all *Elrathia* exoskeletons combined, and for total CIC and sediment from all sources combined. Precisions were ±0.04 for Ca, ±<0.01 for Mg, ±0.06 for Fe, and ±0.01 for S. Detection limits were 0.03 wt. % for Ca, 0.03 for Mg, 0.11 for Fe, and 0.01 for S. Original data tabulated in Appendix 4.1.

Sample type	Ca	Mg	Fe	S
Peronopsis				
total exoskeleton	38.37	0.31	0.59	0.01
cone-in-cone	39.49	0.12	0.25	0.00
sediment	29.43	0.35	0.54	0.03
Elrathia molts				
exoskeleton, molts	35.90	0.63	0.39	0.02
cone-in-cone, molts	40.74	0.11	0.22	0.01
sediment, molts	6.09	2.16	2.83	0.01
Elrathia whole				
exoskeleton	31.46	0.49	0.45	0.01
cone-in-cone	34.78	0.21	0.30	0.00
sediment	0.07	0.47	0.83	0.00
Elrathia total exoskeleton	33.57	0.56	0.42	0.01
Total exoskeleton	34.90	0.49	0.47	0.01
Total cone-in-cone	37.45	0.16	0.27	0.00
Total sediment	12.87	1.27	1.73	0.01

CHAPTER 5

CONSTRAINING OXYGEN AND SULFIDE LEVELS IN CAMBRIAN WHEELER SHALE SEDIMENTS[1]

[1] John, D. J. and Walker, S. E. To be submitted to *Geology*.

Abstract

Trilobites from the middle Cambrian Wheeler Shale of Utah have excellent preservation and unusual modes of life tied to distinctive sedimentological and chemical conditions. These conditions included fluctuations of oxygen levels in the benthos, driving distinct taphofacies for oxic, dysoxic, and anoxic conditions. Trilobites such as *Elrathia kingii* were interpreted to bear special adaptations for inhabiting dysoxic habitats, including potential symbiosis with sulfur-reducing bacteria. However, though it plays a large role in determining the life habits and preservation of benthic organisms, the oxygenation of the benthos has not been constrained through direct geochemical analyses. Here, we perform a suite of geochemical analyses targeting iron (Fe), sulfur (S), carbon (C), and trace metals such as chromium (Cr), vanadium (V), uranium (U), and molybdenum (Mo) to better constrain the presence of dysoxic benthic conditions in putatively dysoxic horizons containing abundant *E. kingii* and *Peronopsis interstricta* and few other species. We found that the geochemistry of these sediments does not support extreme dysoxia or free sulfide above the sediment-water interface. Iron was not extensively scavenged by sulfides, as it would be under euxinic conditions. The euxinia-sensitive trace metals Mo and U were not enriched above detrital values, indicating no free sulfide, but the anoxia-sensitive trace metals Cr and V were enriched, indicating reduced oxygen levels. *Elrathia* may have simply tolerated lower oxygen conditions than other benthic trilobites and, from previous work, was likely not symbiotic with sulfate-reducing bacteria. Our findings suggest that, within the dysoxic horizons examined, the ecology and preservation of organisms in the Wheeler Shale is not driven by exceptionally low-oxygen or euxinic conditions.

Introduction

The middle Cambrian Wheeler Shale of Utah is host to a famous and important trilobite *Lagerstätte* that includes the famous trilobite *Elrathia kingii*. Fossils exhibit several unusual and exceptional modes of preservation, including Burgess-Shale type preservation sediments, as well as cone-in-cone calcite (CIC) encrustations. The exceptional preservation in the Wheeler Shale has long been associated with dysoxia in the benthos (Bright, 1959; Rees, 1986) and drawn comparison to similar preservational pathways for the Burgess Shale (Halgedahl et al., 2009). The CIC encrustations that help enhance preservation are thought to be related to sulfur-reducing microenvironments contained within buried trilobite exoskeletons (Gaines et al., 2005). Likewise, *Elrathia* has been interpreted as a specialist for these exaerobic conditions, possibly through an association with sulfur-oxidizing bacterial symbionts (Gaines and Droser, 2003). However, an examination of the morphological basis for that interpretation suggested that *Elrathia* is not symbiotic (John and Walker, 2016). Trilobites occur within several taphofacies, thought to be controlled by changes in oxygen levels, with horizons containing high-abundance, low diversity assemblages of *E. kingii* and the smaller agnostid trilobite *Peronopsis interstricta* representing extreme low-oxygen environments (Gaines et al., 2005). However, the degree to which their habitats were dysoxic remains to be constrained. Oxygen conditions of the benthos have been interpreted using sedimentological and ichnofabric data, and isotopic sulfur analysis suggests fluctuations in bacterial sulfate reduction (Gaines et al., 2012). However, the sediments have not been directly tested for geochemical evidence of low-oxygen conditions. Here, we determine

if the geochemistry of the sediments supports a dysaerobic or euxinic environment for the Wheeler Shale through analysis of several redox-sensitive sedimentary elemental fluxes.

Iron (Fe), sulfur (S), organic carbon (TOC), and other metals and trace metals (Cr, Mo, Al, Ti) have proven useful in identifying dysaerobic and euxinic conditions in the modern Black Sea and in Proterozoic rocks (Lyons et al., 2009; Reinhard et al., 2013). For example, Fe speciation is sensitive to oxygen and sulfide abundance, and Fe accumulates in the water column if neither is abundant (Lyons et al., 2009). Additionally, total organic carbon influences the behavior of Fe, both by scavenging dissolved Fe to the sediment directly and by providing an energy source for sulfur-oxidizing bacteria that convert free sulfate to sulfide, which then combines with Fe to form pyrite (Lyons and Berner, 1992). If the Wheeler Shale is dysoxic within *E. kingii*-rich beds, then the sediment from those horizons should have evidence in its Fe, S, and TOC ratios of decreased oxygen and possibly free sulfide. Likewise, if bacterial sulfate reduction is crucial to achieving the exceptional fossil preservation, then the presence and extent of euxinia in the sediment will constrain whether sulfate reduction was dependent on organic carbon directly associated with buried trilobites or was occurring throughout the sediment.

Trace metals have seen widespread use as a tool for determining redox conditions in seawater from ancient rocks as far back as Archean in age (Schröder and Grotzinger, 2006; Wille et al., 2013). The trace metals molybdenum (Mo) and chromium (Cr) are derived from continental sources and have long residence times in the oceans, forming non-reactive soluble oxide phases and ensuring they are well-mixed (Mayer, 1988; Scott and Lyons, 2012). Both are gradually removed under normal seawater conditions by

complexing with Fe or manganese (Mn) oxyhydroxides, generating detrital fluxes comparable to crustal concentrations (Tribovillard et al., 2006). They can be used together to constrain oxygen levels because they are strongly redox-sensitive under different conditions: Mo is scavenged nearly quantitatively from solution exclusively under euxinic conditions, where it converts from non-reactive molybdate to a series of reactive thiomolybdates that form ligands with Fe- or S-rich particles and iron sulfides (Tribovillard et al., 2006). A similar behavior is observed for uranium (U), where U(VI) under oxic conditions is reduced to U(IV) in the presence of sulfide, adsorbing and scavenging to the sediment (Tribovillard et al., 2006). Conversely, Cr transitions from soluble, nonreactive Cr(IV) in chromate to reactive Cr(III) under anoxic conditions, and is scavenged by organic particles or Fe- or Mn-oxyhydroxides (Tribovillard et al., 2006). Thus Cr becomes enriched in the sediment under either anoxic or euxinic conditions (Tribovillard et al., 2006). Another trace metal behaving in this manner is vanadium (V), which also enriches under anoxic conditions, though it is slightly less sensitive to reductions in oxygen than Cr (Schröder and Grotzinger, 2006). An enrichment of all trace metals above background detrital levels suggests euxinia, an enrichment of only Cr and V suggests anoxia, while enrichment of Cr but not V suggests dysoxia, and oxic conditions can be inferred where none is enriched (Tribovillard et al., 2006; Lyons et al., 2003; 2009). Additionally, concentrations of Mo indicate the degree of euxinia. Under fully euxinic conditions in the water column (H_2S > ~100 μM), Mo is enriched hundreds of times higher than crustal input values (Lyons et al. 2003). Under dysaerobic conditions with low-oxygen waters overlying sulfidic pore waters in the sediment (H_2S > 0 μM), Mo is enriched only on the order of ten times higher than crustal input (Lyons et

al., 2003). While Mo and U concentrations can be interpreted directly, Cr and V enrichments are first normalized to the detrital flux by using their ratio with a detrital proxy element such as Ti. If the Wheeler Shale benthos are euxinic, then all trace metals should be enriched, indicating reduced oxygen levels and free sulfide in either the underlying sediment or the water column. If only Cr and V are enriched, that suggests bottom-water dysoxia but no free sulfide. If no trace metals are enriched in the sediments, then benthic conditions were more oxic and the ecology of *Elrathia* may not be exclusively dysaerobic.

Methods

Five tests were performed to examine the geochemistry of the Wheeler Shale sediment: 1) total carbon/total sulfur analysis, to give baseline values used to compare to organic carbon and pyrite sulfur; 2) total inorganic carbon analysis that when subtracted from total carbon yields organic carbon, which influences Fe and S cycles; 3) chromium reduction, to quantify the amount of pyrite; 4) sequential iron reduction, to quantify the amount of reactive Fe; and 5) total metal digest, to quantify the concentrations of metals such as Fe, aluminum (Al) and Ti, and trace metals. All sample preparation and analysis was performed at the Lyons Geochemistry Lab, UC Riverside, California (USA).

Twenty-five samples of sediment from the Wheeler Shale were used for the five analyses. Samples were collected by professional collectors from freshly-exposed outcrops buried under ~ five meters of overburden. Each sample was associated with a trilobite; 18 were associated with *E. kingii*, and 7 were associated with *P. interstricta*. These two species make up the preponderance of the dysoxic assemblage (Gaines et al.,

2005), and both were included in the analysis to control for any possible preservational bias for *Elrathia*. Trilobites with CIC were separated from the sediment using tungsten carbide-coated hand chisels, and sediment immediately underlying the fossil was isolated by breaking away adjacent sediment with a rock hammer (Fig. 5.1). The underlying sediment, which had not been in contact with steel tools, was then pulverized in a Spex 8000 mill with an aluminum ceramic grinding ball to yield approximately 20 ml of powder for each sample. Each powdered sample was subdivided for the five tests.

For the total carbon/total sulfur analysis, ~100 mg of sample powder was weighed into a crucible and fired on an Eltra furnace to approximately 1350 °C under a pure oxygen atmosphere. All C and S in the sample was converted to CO_2 and SO_2 gas, respectively, which was measured by infrared absorption on an Eltra CS500 determinator to yield total weight percent C and S in the sample. An Alpha Resources AR4007 ore standard was run six times before and twice after samples, and indicated a precision of ±1.8% for C and ±18.3% for S.

For the total inorganic carbon (TIC) analysis, sample powder (~100 mg) was weighed into a 250 ml flask and mixed with ethanol (~10 ml) to suspend the powder. The flask was connected to an Eltra CS500 determinator, 20% HCl (~10 ml) was added, and the mixture heated to ~50 °C to convert all inorganic carbon to CO_2. The CO_2 was measured to yield weight percent inorganic carbon. Weight percent of organic carbon was then determined as the difference between total and inorganic carbon. An Alpha Resources AR 4007 was run three times before and once after the samples, and indicated a precision of ±3.6% for C and ±5.5% for S.

For the chromium reduction, sample powder (~750 mg) was weighed into a reaction vial to three decimal places. The vial was attached to a gas-capture line and the powder was mixed with $CrCl_2$ (30 mL) and HCl (15 mL) to achieve complete conversion of pyrite to H_2S. The solution was heated at ~225 °C for 2 hours in a N_2-flushed atmosphere. The resultant exsolved gases were captured, cooled, and condensed to remove acid vapors and bubbled through a solution of 3% Zinc acetate to capture H_2S. This solution was removed and mixed with a starch indicator (1 ml) and 6M HCl (10 ml) in a sealed flask and titrated with 0.1M potassium iodide until a persistent color change occurred. The volume of titrant necessary for this was used to calculate the weight percent of pyrite in the original sample powder. Four samples were replicated, and indicated a precision of ±4.6%

For the sequential iron extraction, sample powder (~100 mg) was weighed to five decimal places into centrifuge tubes, the necessary level of precision for calculating accurate values. The tubes were filled with a solution of sodium acetate and acetic acid (10 ml) at a pH of 4.5 and were shaken for 48 hours to dissolve reactive Fe associated with carbonates. The tubes were spun down at 5000 rpm for 5 minutes to separate the powder and solution, and a split of solution (4 ml) was taken from each tube to analyze. The remainder of the acetate solution was discarded, while the sample powder was retained in the centrifuge tubes for the next solution treatment. A solution (10 ml) of 50 g/L sodium dithionite with 0.35M acetic acid and 0.2M sodium citrate at a pH of 4.8 was added to centrifuge tubes and shaken for 2 hours to dissolve reactive Fe associated with ferric oxides. The tubes were spun down and a split of the solution (4 ml) was taken for analysis and the rest of the solution was discarded, with the sediment retained in the

centrifuge tubes. A third solution of 0.2M ammonium oxalate with 0.17M oxalic acid and ammonium hydroxide at a pH of 3.2 (10 ml) was added to the tubes and shaken for 8 hours to dissolve reactive Fe associated with mixed-valence Fe oxides such as magnetite. The tubes were spun down and a split of the solution (4 ml) was taken for analysis. A split of each of the solvent mixtures (4 ml) was also taken at each step before they were added to sample tubes to serve as blanks. The splits of each of the sequential solutions were analyzed by ICP-MS to yield the amount of reactive Fe associated with each mineral phase (carbonates, ferric oxides, and magnetite).

For the total metal digest, sample powder (~100 mg) was weighed to five decimal places into a crucible. The powder was ashed at 800 °C for 8-12 hours to drive off any organic material and the mass loss on ignition recorded to five decimal places. The resulting ash was transferred to Teflon jars and weighed again to five decimal places. The ash was dissolved in a mixture of HNO_3 (4 ml) and HF (0.5 ml), and the jar was capped and heated to approximately 130 °C for 8-12 hours. The acid solution was uncapped and dried at 105 °C until almost dry then redissolved in HNO_3 (1 ml), followed by HCl (3 ml). The jar was recapped and heated again to 120 °C for 8-12 hours. The samples were uncapped and allowed to dry once more. Finally, samples were redissolved in deionized water (4.75 ml) with HNO_3 (0.25 ml) and transferred to Nalgene bottles. This sequential acid digestion draws out all metals and trace metals into solution for analysis via ICP-MS, which was performed at the Lyons Lab at UC Riverside, California (USA). Both the total metal digest and the sequential iron were measured on the same instrument; two standards were run with the total metal digest, indicating an average precision of ±4.3%

The first four tests combine to yield data to compare C (both inorganic and organic), S, and Fe, including the proportion of Fe and S from pyrite; pyrite Fe is added to the sequential iron extraction's three Fe concentrations to yield highly reactive Fe (Fe_{HR}). The fifth test yields metal and trace metal concentrations that can be directly interpreted as well as compared to the results from the first four tests.

Several ratios that give information about paleoenvironmental conditions were calculated for each sample from the results of these tests. First, the ratio of pyrite sulfur to total organic carbon (S_{py}/TOC) indicates euxinic bottom waters. Under oxic conditions, pyrite formation is linked to the abundance of organic carbon that drives bacterial sulfate reduction after burial, while under euxinic conditions, pyrite formation is instead limited by Fe availability, generating much more sedimentary pyrite and thus S_{py}/TOC ratios well above the expected Cambrian marine average of ~0.67 (Berner and Raiswell, 1983). Second, three ratios describe the activity of free sulfide in the water column (i.e., euxinia). Under euxinic conditions, dissolved Fe is converted to pyrite and deposited in the sediment, enriching it with highly reactive pyrite Fe relative to the flux of all iron to the sediment (Fe_{HR}/FeT). Ratio values of ~0.6 – 0.7 are characteristic of euxinic basins, while values of ~0.26 are characteristic of oxic sediments (Lyons and Severmann, 2006). The total flux of iron is also enriched relative to the rate of sedimentation (Fe_T/Al), with euxinic ratios ranging no lower than ~0.6 (Lyons and Severmann, 2006) and average shale values ~0.5 (Taylor and McLennan, 1985). The amount of reactive iron deposited as pyrite is enriched relative to the flux of reactive iron from non-pyrite phases (degree of pyritization, or DOP, calculated as Fe_{py}/Fe_{HR}), with values under 0.42 corresponding to oxic conditions, values above 0.42 representing

dysoxic conditions with euxinic porewaters, and values over 0.55 representing fully euxinic conditions, where the overlap represents gradation between the latter two (Raiswell et al., 1988; Lyons et al., 2009).

Among the trace metals, the ratio of Cr/Ti describes the enrichment of Cr relative to detrital sedimentation rate (which gives a ratio roughly equivalent to crustal ratios of ~0.017). Enrichment above background rates (up to ~0.025) indicates anoxic conditions where Cr scavenging by organic matter is enhanced, while enrichment at background rates shows that no scavenging is occurring, indicating oxic conditions (Reinhard et al., 2013). Similarly, V under sufficiently anoxic conditions will enrich beyond its crustal background rate of ~20 ppm (Schröder and Grotzinger, 2006). Concentrations of Mo vary strongly by redox conditions, with oxic waters only depositing detrital Mo at concentrations similar to crustal values of 1-2 ppm. Weakly dysoxic bottom waters overlying anoxic porewaters scavenge Mo across the sediment-water interface and enrich Mo to ~20 ppm. Intermittently euxinic waters scavenge directly from the water column and can enrich to ~60 ppm (Lyons et al., 2009). Concentrations of U follow a similar pattern to Mo, with non-euxinic conditions depositing at the crustal value of ~2 ppm and euxinic conditions concentrating upwards of ~10 ppm (Wille et al., 2013). Additionally, Mo scavenging is linked to abundance of TOC under euxinic conditions, where more TOC generates more sulfide production and thus more Mo scavenging. Under oxic conditions, though, Mo scavenging is tied to Mn oxyhydroxide formation, which is unrelated to TOC. Mo and TOC should therefore show a positive correlation under euxinic conditions, and no correlation under oxic conditions (Lyons et al., 2009).

Measurements of C, S, Fe, Mo, Cr, U, V, aluminum (Al) and titanium (Ti) were made for each of 25 samples, and means among the samples calculated for each measurement (Table 5.1; Appendices 5.1-5.5). From these, five ratios were calculated, along with their means for the 25 samples (Table 5.2).

Results

Variations within measurements

Total carbon ranged from 2.63 – 6.73 wt. %, with a mean of 3.91 wt. %, while TOC varied proportionally more, from 0.01 – 2.01 wt. % (Table 5.1). A single TOC measurement of 4.40%, nearly equal to the total carbon measured in Sample 16, is likely a measurement error, and an unusually low TOC measured in Sample 3 (0.01) potentially is as well. Ignoring those outliers, the remaining 24 samples have a mean of 0.41 wt. % organic carbon, comparable to TOC values of ~0.2% in the Burgess Shale (Butterfield, 1995) but less than those reported for the Chengjiang (up to 1.4%; Zhu et al., 2005) or black shales (up to 10%, Kennedy et al., 2002). Measurements for S and Fe were more consistent, as were concentrations for Al, Ti, and Cr. The two proxies for anoxia, V and Cr, corresponded tightly with each other, as did Al and Ti, the two proxies for detrital flux. However, Mo showed a decreasing pattern from the first nine samples (mean 5.23 ppm) through the last 16 (mean 1.15 ppm). However, the order of samples was random and this decrease does not correspond to any environmental gradient or difference between species; it may represent an error in the instrument or may simply be coincidental. Uranium, the counterpart to Mo as euxinic proxies, varied very little throughout the samples.

These raw values were used to calculate ratios that can indicate seawater conditions (Table 5.2). While data were generally consistent, a few abnormally high outliers were identified among TOC (3 samples for TOC ≥1.92 , where all others were ≤0.45) and Mo (Two samples ≥9.83, where all others range between 0.85-5.18). These are likely measurement errors, given the low concentration of TOC relative to TIC, and low absolute concentrations of Mo. Ignoring these TOC outliers, S_{py}/TOC ratios ranged between 0.03 – 1.32, with a mean of 0.50 (Table 5.3). Ratios of Fe_{HR}/Fe_T varied from 0.18 – 0.47, with a mean of 0.30. Ratios of Fe_T/Al varied from 0.32 – 0.66, with a mean of 0.43. Measurements of DOP ranged between 0.02 and 0.24, with a mean of 0.12. The ratio of Cr/Ti varied between 0.01 and 0.05, with a mean of 0.03.

Measured and calculated values generally did not vary between *Elrathia* (n = 18) and *Peronopsis* (n = 7), with a few exceptions. *Peronopsis* were significantly higher for total carbon (p = 0.032, H = 4.616, df = 1 by Kruskal-Wallis analysis with $\alpha = 0.05$) but not TOC (p = 0.154, H = 5.871, df = 1). *Elrathia* was significantly higher than *Peronopsis* for concentrations of Mo ($p < 0.001$, H = 14.538, df = 1). The lack of significant difference in all other samples suggests that there are no preservational biases between the two species, and values calculated for either are representative of the overall unit.

C-S-Fe variations in geochemical conditions in the Wheeler Shale

Carbon, sulfur, and iron suggest that benthic conditions varied between oxic and generally slightly euxinic conditions (Table 5.3). S_{py}/TOC ratios vary across euxinic threshold value of ~0.67, with five of 23 samples consistent with euxinia (mean = 0.48),

when two outliers are excluded. Fe_{HR}/Fe_T values are entirely below the threshold of ~0.6 – 0.7 that would indicate euxinia and closer to the oxic average of ~0.28 (mean = 0.30; Table 5.2; Fig. 5.2). Fe_T/Al ratios (mean = 0.43; Fig. 5.2) are close to average shale values of ~0.5 (Taylor and McLennan, 1985), with only two samples ranging above 0.6 into potentially euxinic values (Lyons and Severmann, 2006; Table 5.3). DOP values (mean = 0.121; Fig. 5.2) are all well below the threshold of ~0.42 where euxinia in the subsurface begins (Lyons et al., 2009).

Lack of euxinia in Wheeler Shale based on trace elements

Trace metal analyses suggest limited dysoxia with no euxinia in either bottom waters or sediments. Low values for Mo were detected in all sediments (mean = 2.62 ppm; Table 5.1; Fig. 5.2), similar to crustal values of 1-2 ppm. Of the 25 samples, five were above the 95% confidence interval (3.692 ppm) for the sample set, but all were still well below the expected values for weakly dysoxic bottom waters overlying euxinic porewaters (~20 ppm) or intermittently euxinic bottom waters (~60 ppm; Lyons et al., 2009; Fig 5.2). Values for U (mean = 2.43 ppm; Table 5.1) were similar to crustal values of ~2 ppm and well below the euxinic level of ~10 ppm, confirming the Mo values. Additionally, after removing five outliers with exceptionally high Mo or TOC readings and applying a natural-log transformation to correct for non-normality, values for Mo and TOC yielded a Pearson's correlation coefficient of r = -0.338; with outliers included, the correlation is weaker (r = -0.177). The correlation is not significant (p = 0.145; α = 0.05), indicating no correlation, and thus no euxinia in bottom waters (Fig. 5.3).

Cr is consistent with dysoxic seawater where trace metals begin to be scavenged to the sediment. Ratios of Cr/Ti are at the threshold of ~0.025 characteristic of Phanerozoic anoxic shales (mean = 0.03; Fig. 5.2) (Reinhard et al 2013). Values for V (mean = 78.67; Table 5.1) are markedly higher than average crustal values of ~20 ppm, indicating enrichment and dysoxia, confirming the Cr values.

Discussion

The Wheeler Shale benthos, inhabited by *Elrathia*, was most likely intermittently dysoxic and not euxinic. Iron, sulfur, and carbon analyses suggest very limited generation of pyrite from reactive Fe. The relatively low Fe_{HR}/Fe_T values indicate that the iron being delivered is not in reactive forms, as it would be if Fe was being scavenged under euxinic conditions. Rather, the Fe_T/Al ratios near the crustal average suggest that most of the iron is detrital, likely in non-reactive forms like iron silicates (Lyons and Severmann, 2006). Likewise, low DOP values suggest that Fe being scavenged into the sediment is not in the form of pyrite, indicating that the system is sulfide-limited and thus not euxinic (Lyons et al., 2009).

Trace metals likewise suggest redox-sensitive ions were not being enriched under euxinic conditions beyond detrital values, but may have been enriched under dysoxic conditions. Molybdenum and U were not enriched in the sediments as expected for persistently euxinic conditions (Tribovillard et al, 2006). Molybdenum levels also did not suggest euxinia in the sediment under a dysoxic water column (Lyons et al., 2009). The weakly negative correlation observed between Mo and TOC suggests that Mo deposition is not linked to the generation of free sulfide (Lyons et al., 2009). Therefore,

conditions in the Wheeler Shale were not euxinic. However, Cr/Ti ratios and V concentrations above crustal values suggest that their deposition in the Wheeler Shale was enriched by scavenging where dysoxic conditions were driving increased Cr and V flux to the sediment (Reinhard et al., 2013).

We found that sedimentary geochemistry suggests benthic conditions were slightly dysoxic, but not exaerobic (extremely dysoxic) as previously described (Gaines and Droser, 2003). The characteristic *Elrathia* from horizons we analyzed were thus not an extremophile species adapted for barely oxygenated conditions. Though dissolved oxygen levels may not have been low enough to cause a change in redox behavior for iron, sulfur, or trace metals, oxygenation may have still been reduced sufficiently to inhibit other benthic species, while *Elrathia* could tolerate those conditions. However, the lack of evidence for euxinia suggests that *Elrathia* did not inhabit conditions where symbiosis with sulfur-oxidizing bacteria (as described by Fortey, 2000) would be necessary or possible. This corroborates our findings in previous work that morphologies like *Elrathia*'s are not related to symbiosis (John and Walker, 2016).

The Fe, S, and euxinia-sensitive trace metal (i.e., U and Mo) data all indicate that there is not an active sulfate reduction zone close below the sediment-water interface, where metals and trace metals could flux from oxic bottom waters to euxinic pore waters and become fixed and enriched in the sediment. This is surprising, as sulfate-reducing conditions are necessary for the rapid precipitation of the CIC in the Wheeler Shale (Gaines et al., 2005). This preservation is thought to be related to extremely localized geochemical gradients driven by bacterial sulfate reduction of organic matter buried alongside trilobite exoskeletons, and physically contained within the carapace and by

occluded porosity in the sediments (Gaines et al., 2005). Our findings suggest that the sulfate-reduction zone necessary for precipitating CIC may be much deeper, and not interacting directly with bottom waters. This would suggest CIC formation does not occur rapidly after burial, but later in diagenesis, consistent with results from Chapter 4.

Conclusion

The geochemistry of the Wheeler Shale suggests weak dysoxia in the benthos, and a lack of euxinia in the benthos or the immediate subsurface. Carbon-sulfur-iron ratios all suggest limited formation of pyrite and sequestration of reactive iron, consistent with more oxic conditions. Trace metal analyses of Cr and V alongside Mo and U also suggest a lack of enrichment associated with scavenging by organic matter or sulfides under anoxic or euxinic conditions, respectively. Even within the sediments, low pyritization and extremely low Mo concentrations suggest a lack of widespread bacterial sulfate reduction. These findings stand somewhat at odds with the prevailing interpretations of the Wheeler Shale benthos, which are thought to be more pervasively dysoxic with active subsurface sulfate reduction. Our study raises the possibility that *Elrathia* may not be an extreme low-oxygen specialist, but merely tolerant of lower oxygen levels than other benthic trilobites. Likewise, the lack of geochemical evidence for a widespread, anoxic sulfate-reducing zone in the sediment, despite the presence of CIC growth on the trilobites that necessitates sulfate reduction, suggests that CIC may be forming later and slower than previously described. Our results, based on geochemical signals heretofore unexplored in the Wheeler Shale, bring a new perspective to our understanding of the ecology and exceptional preservation of its trilobites

References

Berner, RA and Raiswell, R. Burial of organic carbon and pyrite sulfur in sediments over Phanerozoic time: a new theory. Geochimica et Cosmochimica Acta, 47:855-862.

Bright, RC. 1959. A paleoecologic and biometric study of the middle Cambrian trilobite *Elrathia kingii* (Meek). Journal of Paleontology, 33:83-98.

Butterfield, NJ. 1995. Secular distribution of Burgess-Shale-type preservation. Lethaia, 28:1-13.

Ferrill, D.A., Morris, A.P., Evans, M.A., Burkhard, M., Groshong, R.H. Jr., and Onasch, C.M. 2004. Calcite twin morphology: a low-temperature deformation geothermometer. Journal of Structural Geology Acta, v. 26, p. 1521-1529.

Fortey, R. 2000. Olenid trilobites: the oldest known chemoautotrophic symbionts? PNAS, 97:6574-6578.

Gaines, RR and Droser, ML. 2003. Paleoecology of the familiar trilobite *Elrathia kingii*: an early exaerobic zone inhabitant. Geology, 31:941-944.

Gaines, RR, Kennedy, MJ, and Droser, ML. 2005. A new hypothesis for organic preservation of Burgess Shale taxa in the middle Cambrian Wheeler Formation, House Range, Utah. Palaeogeography, Palaeoclimatology, Palaeoecology, 220:193-205.

Gaines, RR, *et al*. 2012. Mechanism for Burgess Shale-type preservation. PNAS, 109:5180-5184.

Halgedahl, SL, Jarrard, RD, Brett, CE, and Allison, PA. 2009. Geophysical and geological signatures of relative sea level change in the upper Wheeler Formation,

Drum Mountains, West-Central Utah: A perspective into exceptional preservation of fossils. Palaeogeography, Palaeoclimatology, Palaeoecology, 277:34-56.

John, DJ and Walker, SE. 2016. Testing symbiotic morphology in trilobites under dysoxic and oxic conditions from Cambrian to Early Ordovician Lagerstätten. Palaeogeography, Palaeoclimatology, Palaeoecology, 441:704-720.

Kennedy, MJ, Pevear, DR, and Hill, RJ. 2002. Mineral surface control of organic carbon in black shale. Science, 295:657-660.

Lyons, TW and Berner, RA. 1992. Carbon-sulfur-iron systematics of the uppermost deep-water sediments of the Black Sea. Chemical Geology, 99:1-27.

Lyons, TW, and Severmann, S. 2006. A critical look at iron paleoredox proxies: new insights from modern euxinic marine basins. Geochimica et Cosmochimica Acta, 70:5698-5722.

Lyons, TW, Werne, JP, Hollander, DL, and Murray, RW. 2003. Contrasting sulfur geochemistry and Fe/Al and Mo/Al ratios across the last oxic-to-anoxic transition in the Cariaco Basin, Venezuela. Chemical Geology, 195:131-157

Lyons, TW, Anbar, AD, Severmann, S, Scott, C, and Gill, BC. 2009. Tracking euxinia in the ancient ocean: a multiproxy perspective and proterozoic case study. Annual Review of Earth and Planetary Science, 37:507-534.

Mayer, J. 1988. Geochemistry of chromium in the oceans. *in* Chromium in Natural and Human Environments, JO Nriagu and E Niebor, eds., Wiley.

Raiswell, R, Buckley, F, Berner, RA, and Anderson, TF. 1988. Degree of pyritization of iron as a paleoenvironmental indicator of bottom-water oxygenation. Journal of Sedimentary Petrology, 58:812-819

Reinhard, CT, Planavsky, NJ, Robbins, LJ, Partin, CA, Gill, BC, Lalonde, SV, Bekker, A, Konhauser, KO, and Lyons, TW. 2013. Proterozoic ocean redox and biogeochemical stasis. PNAS, 110:5357-5362.

Rees, MN. 1986. A fault-trough through a carbonate platform: the Middle Cambrian House Range embayment. GSA Bulletin, 97:1054-1069.

Scott, C and Lyons T. 2012. Contrasting molybdenum cycling and isotopic properties in euxinic versus non-euxinic sediments and sedimentary rocks: refining the paleoproxies. Chemical Geology, v. 324-325, p. 19-27.

Taylor, SR, and McLennan, SM. 1985. *The Continental Crust: Its Composition and Evolution*. Blackwell, Oxford.

Tribovillard, N, Algeo, TJ, Lyons, T, and Ribolleau, A. 2006. Trace metals as paleoredox and paleoproductivity proxies: an update. Chemical Geology, 232:12-32.

Wille, M, Nebel, O, Van Kranendonk, MJ, Schoenberg, R, Kleinhanns, IC, and Elwood, MJ. 2013. Mo-Cr evidence for a reducing Archean atmosphere in 3.4-2.76 Ga black shales from the Pilbara, Western Australia. Chemical Geology, 340:68-76.

Figures and Tables

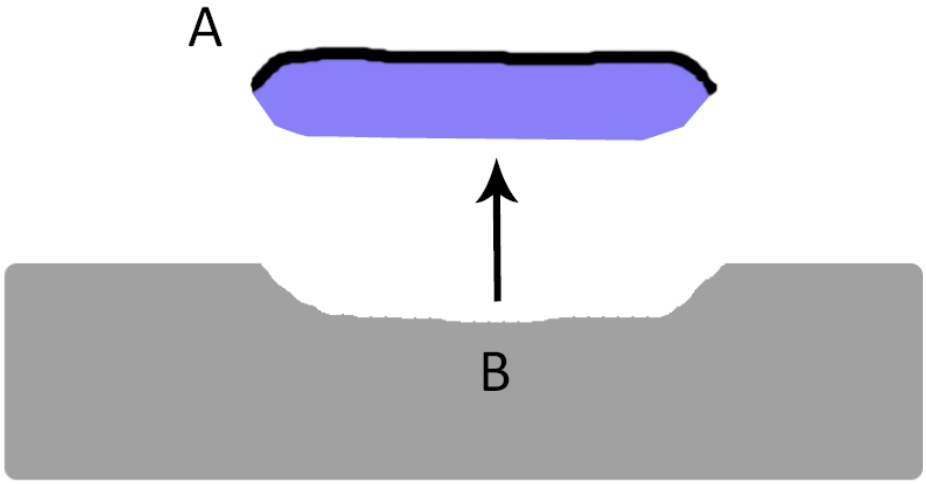

Figure 5.1. Location of samples taken. Fossil and cone-in-cone (A) was separated from underlying sediments (B), which were pulverized for geochemical analysis. Exoskeleton and cone-in-cone were not used for this analysis.

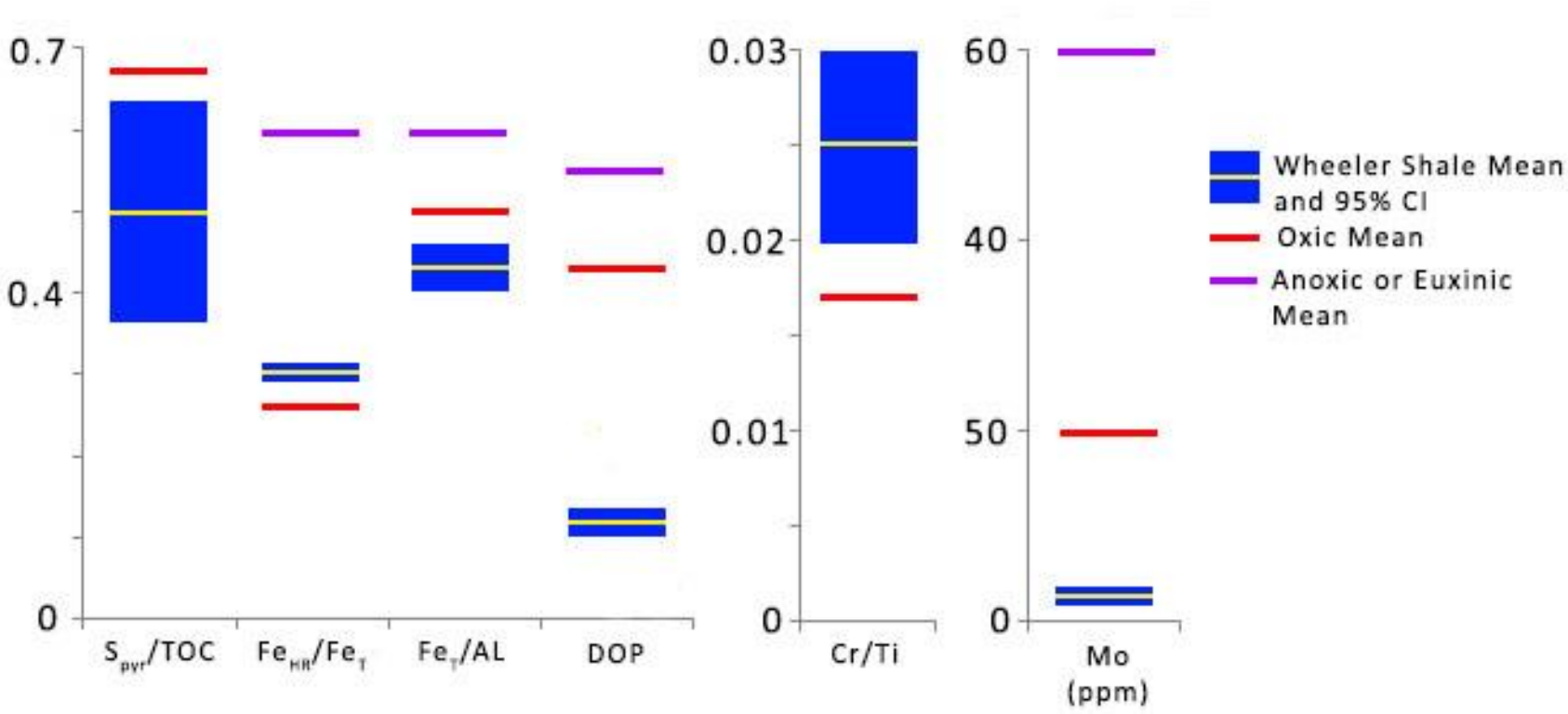

Figure 5.2. Mean measured geochemical values from C and S analyses, Fe extraction and total metal digests. Blue boxes represent 95% confidence intervals for Wheeler Shale sediments, red and purple lines to published means or thresholds for oxic and anoxic or euxinic sediments. All ratios and measurements are consistent with oxic or weakly dysoxic benthos except for Cr/Ti, which suggests more prevalent reduced oxygen levels. See Methods for descriptions of each ratio or measurement and citations for threshold values.

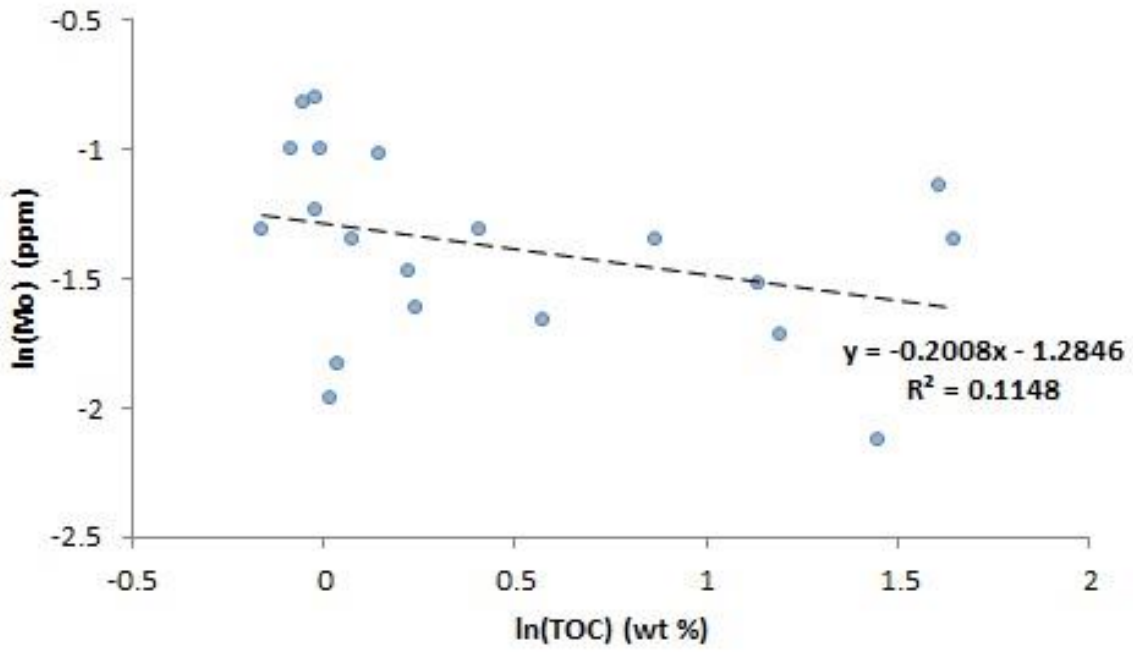

Figure 5.3. Total organic carbon (weight %) vs. Mo (ppm) for 20 analyzed specimens. Data have been log-transformed and outliers have been removed. Dashed line is the regression line, with formula and R^2 value. There is no strong positive correlation between the two elements, as seen in other euxinic localities where organic carbon drives sulfate reduction that sequesters Mo in the sediment. Molybdenum is thus likely not depositing under euxinia.

Table 5.1. Raw data for geochemical analyses. Data for carbon, sulfur, and iron analyses given in weight percentages: total carbon (TC), total organic carbon (TOC) as calculated by subtracting inorganic carbon from total carbon, from carbon-sulfur analysis; sulfur from pyrite (S_{py}) from chromium reduction analysis; total iron (Fe_T), highly reactive iron (Fe_{HR}), and iron associated with pyrite (Fe_{py}) from sequential iron extractions, and elemental concentrations from total metal digests for Al, Mo, Cr, and Ti. Values were averaged by type of fossil associated with sediments, and overall means were also calculated. Measurements considered potentially erroneous are marked with an asterisk.

Sample	Genus	TC (wt. %)	TOC (wt. %)	S_{py} (wt. %)	Fe_T (wt. %)	Fe_{HR} (wt. %)	Fe_{py} (wt. %)
1	*Elrathia*	3.16	0.26	0.135	3.330	0.856	0.118
2	*Elrathia*	5.84	1.92	0.091	2.612	0.755	0.079
3	*Elrathia*	3.05	0.01*	0.119	2.240	0.680	0.104
4	*Elrathia*	3.50	0.12	0.062	2.436	1.011	0.054
5	*Elrathia*	2.89	0.18	0.160	3.336	0.707	0.139
6	*Elrathia*	3.21	0.22	0.025	3.161	0.824	0.022
7	*Elrathia*	2.92	0.32	0.192	1.837	0.863	0.167
8	*Elrathia*	3.14	0.22	0.189	2.795	0.849	0.165
9	*Elrathia*	4.30	0.26	0.133	3.184	0.907	0.116
10	*Elrathia*	2.93	0.19	0.247	2.724	0.699	0.215
11	*Elrathia*	4.64	2.01	0.060	3.048	0.974	0.052
12	*Elrathia*	2.63	0.27	0.119	3.065	0.892	0.104
13	*Elrathia*	6.73	0.20	0.094	2.544	0.652	0.082
14	*Elrathia*	3.45	0.23	0.149	2.319	0.864	0.130
15	*Elrathia*	3.06	0.36	0.249	3.149	0.882	0.217
16	*Elrathia*	4.41	4.40*	0.073	2.441	0.657	0.064
17	*Elrathia*	3.13	0.16	0.022	2.930	0.888	0.019
18	*Elrathia*	3.39	0.26	0.235	2.850	0.955	0.205
	Mean, Elrathia	***3.69***	***0.64***	***0.131***	***2.778***	***0.829***	***0.114***
19	*Peronopsis*	5.20	0.29	0.149	1.748	0.759	0.130
20	*Peronopsis*	4.75	0.44	0.185	2.779	0.778	0.161
21	*Peronopsis*	3.16	0.37	0.170	2.347	0.612	0.148
22	*Peronopsis*	5.12	0.27	0.165	2.814	0.898	0.144
23	*Peronopsis*	5.25	0.37	0.148	3.127	0.754	0.129
24	*Peronopsis*	3.98	0.14	0.042	3.364	0.705	0.037
25	*Peronopsis*	3.87	0.45	0.021	3.611	0.662	0.018
	Mean, Peronopsis	***4.48***	***0.33***	***0.126***	***2.827***	***0.738***	***0.109***
Grand Mean		***3.91***	***0.56***	***0.13***	***2.792***	***0.803***	***0.113***

Sample	Genus	Al (ppm)	Mo (ppm)	Cr (ppm)	Ti (ppm)	U (ppm)	V (ppm)
1	*Elrathia*	91302.3	5.18	84.78	3588.4	3.12	97.87
2	*Elrathia*	41009.6	2.83	84.68	2165.4	3.04	95.79
3	*Elrathia*	61700.4	9.83	89.93	2167.4	2.83	102.82
4	*Elrathia*	68629.6	4.26	61.60	2643.3	2.75	73.27
5	*Elrathia*	83914.5	3.29	45.81	3582.8	2.58	53.40
6	*Elrathia*	75711.6	11.24	83.15	3496.2	2.64	93.29
7	*Elrathia*	53344.6	4.98	62.36	2124.1	2.84	70.92
8	*Elrathia*	70565.7	3.12	75.92	2823.6	2.48	85.65
9	*Elrathia*	59203.8	2.38	60.78	2872.6	2.07	70.21
10	*Elrathia*	83812.6	1.78	78.72	3022.9	2.30	82.49
11	*Elrathia*	69241.0	1.59	81.98	2919.9	2.36	95.53
12	*Elrathia*	86818.7	1.50	73.01	3331.6	2.15	81.83
13	*Elrathia*	38482.5	1.27	69.50	1816.4	1.98	83.71
14	*Elrathia*	56248.7	1.25	80.14	2488.9	2.39	93.60
15	*Elrathia*	63076.0	1.16	55.94	3146.7	2.35	65.73
16	*Elrathia*	59917.1	1.09	58.69	2511.8	2.22	68.43
17	*Elrathia*	89264.3	1.04	74.44	3223.1	2.22	84.27
18	*Elrathia*	79227.2	1.08	45.76	2829.3	2.14	54.47
	Mean, Elrathia	***68415.0***	***3.27***	***70.40***	***2819.7***	***2.47***	***80.74***
19	*Peronopsis*	32592.7	0.98	69.04	1522.9	2.36	80.45
20	*Peronopsis*	63432.7	0.95	72.40	2670.8	2.20	82.34
21	*Peronopsis*	68222.0	0.99	65.98	2495.5	2.49	76.22
22	*Peronopsis*	57216.8	0.85	68.94	2320.8	2.25	78.46
23	*Peronopsis*	67661.5	0.92	61.04	2939.3	2.14	71.58
24	*Peronopsis*	68833.4	1.02	51.20	2635.1	2.44	61.04
25	*Peronopsis*	71380.9	0.98	52.27	3104.4	2.51	63.38
	Mean, Peronopsis	***61334.3***	***0.96***	***62.98***	***2527.0***	***2.34***	***73.75***
Grand Mean		***66432.4***	***2.62***	***68.32***	***2737.7***	***2.43***	***78.67***

Table 5.2. Calculated ratios for elemental data indicating environmental conditions. Ratio of S as pyrite to total organic carbon (S_{py}/TOC), highly reactive to total Fe (Fe_{HR}/Fe_T), total Fe to Al (Fe_T/Al), Cr to Ti, and degree of pyritization (DOP), calculated as $Fe_{py}/(Fe_{py}+Fe_{HR})$. Ratios were averaged by type of fossil associated with sediments, and overall means were also calculated. Measurements considered potentially erroneous are marked with an asterisk.

Sample	Genus	S_{py}/TOC	Fe_{HR}/Fe_T	Fe_T/Al	DOP	Cr/Ti
1	*Elrathia*	0.52	0.257	0.36	0.121	0.024
2	*Elrathia*	0.05	0.289	0.64	0.095	0.039
3	*Elrathia*	9.88*	0.303	0.36	0.132	0.041
4	*Elrathia*	0.51	0.415	0.36	0.051	0.023
5	*Elrathia*	0.88	0.212	0.40	0.165	0.013
6	*Elrathia*	0.11	0.261	0.42	0.026	0.024
7	*Elrathia*	0.60	0.470	0.34	0.162	0.029
8	*Elrathia*	0.87	0.304	0.40	0.162	0.027
9	*Elrathia*	0.51	0.285	0.54	0.113	0.021
10	*Elrathia*	1.32	0.257	0.32	0.235	0.026
11	*Elrathia*	0.03	0.320	0.44	0.051	0.028
12	*Elrathia*	0.44	0.291	0.35	0.104	0.022
13	*Elrathia*	0.47	0.256	0.66	0.112	0.038
14	*Elrathia*	0.65	0.372	0.41	0.131	0.032
15	*Elrathia*	0.69	0.280	0.50	0.197	0.018
16	*Elrathia*	0.02*	0.269	0.41	0.088	0.023
17	*Elrathia*	0.14	0.303	0.33	0.021	0.023
18	*Elrathia*	0.91	0.335	0.36	0.177	0.016
	Mean, Elrathia	***1.03***	***0.304***	***0.42***	***0.119***	***0.026***
19	*Peronopsis*	0.52	0.434	0.54	0.146	0.045
20	*Peronopsis*	0.42	0.280	0.44	0.172	0.027
21	*Peronopsis*	0.46	0.261	0.34	0.195	0.026
22	*Peronopsis*	0.61	0.319	0.49	0.138	0.030
23	*Peronopsis*	0.40	0.241	0.46	0.146	0.020
24	*Peronopsis*	0.31	0.210	0.49	0.049	0.019
25	*Peronopsis*	0.05	0.183	0.51	0.027	0.017
	Mean, Peronopsis	***0.39***	***0.275***	***0.47***	***0.125***	***0.027***
Grand Mean		***0.85***	***0.296***	***0.43***	***0.121***	***0.026***

CHAPTER 6

CONCLUSIONS

My work suggests that the environments inhabited by *Elrathia* and *Peronopsis* were not extremely dysoxic. Thus, the role that trilobites such as *Elrathia* and *Peronopsis* played in the ecology of that benthos does not appear to be symbiotic, as previously suggested based on their similar morphology to olenid trilobites.

Morphological analysis for a wide set of Cambrian trilobites suggests that a similarity to olenids is not related to low-oxygen conditions, as would be expected if the morphology was an adaptation to facilitate symbiosis. Rather, it seems that the morphology is common among ptychopariid trilobites from all environments, suggesting that taxonomy is the main factor controlling olenimorphic trilobites.

Likewise, biomarker analysis did not find evidence of sulfur-oxidizing bacteria that would indicate symbiosis within trilobites, though results were equivocal because of the overprint of modern biogenic and anthropogenic compounds. However, these compounds bore a record of Recent ecological change in the overlying environment, and suggest that multibiomarker analyses of fossil material may be a useful tool in assessing anthropogenic effects on ecosystems.

The petrography and geochemistry of the fossils and associated cone-in-cone calcite (CIC) suggest that exceptional preservation did not begin immediately after burial in strongly euxinic conditions, but rather began after the development of overburden and sediment compaction. Cone-in-cone calcite grew within unconsolidated but cohesive

sediments. The presence of thick CIC on concave surfaces in complete individuals from both trilobite species, regardless of molt status, indicates the primary factor controlling CIC growth is not the abundance of organic carbon. Rather, CIC forms from a combination of supersaturation of diffuse pore fluids from a later sulfur-reducing stage and nucleation of calcite crystals along the surface of calcareous trilobite exoskeletons. This process was partially mediated by zones of low pressure within a vertical stress field, and may have occurred at temperatures bordering between late diagenetic and metamorphic. This process has overprinted the original chemistry of the trilobite exoskeletons through recrystallization, removing any original difference between benthic *Elrathia* and potentially pelagic *Peronopsis* and preserving only diagenetic chemistries within both exoskeletons and CIC.

The geochemistry of the sediments, heretofore unexplored, corroborates the previous interpretations of limited dysoxia in the benthos and limited euxinia in the shallow subsurface. Analysis of Fe, S, and C generate a range of values indicating oxic to dysoxic conditions, but analysis of Fe and trace metal analysis of Cr, V, U and Mo suggest that euxinia is not reached in the water column or in the sediments. This indicates that the bacterial sulfate reduction necessary for generating CIC and exceptional preservation does not immediately begin upon burial, but occurs deeper in the sediments, decoupled from exchanges at the sediment-water interface.

APPENDICES

Appendix 2.1. C**haracter scores, locality information, and NMDS1 scores for all trilobite genera** from the eight early–to-middle Cambrian *Lagerstätten*.

	Character States						
Genus	**Segments**	**Hypostome attachment**	**Pleural morphology**	**Carapace morphology**	**Exoskeletal ornamentation**	**Locality**	**NMDS1 Score**
Cambrian Trilobites							
Order Corynexochida							
Family Dolichometopidae							
Bathyuriscus	8	1	0.5	0.5	1	B W M S	0.3396
Glossopleura	8	0	0	1	0	B S	-1.0464
Hanburia	5	0	1	0.5	1	B	-0.0933
Hemirhodon	7	0	1	1	1	M	0.0341
Orria	8	0	1	0.5	1	M	-0.0857
Family Dorypyge							
Dorypyge	6	0	0	1	0	S	-1.0439
Kootenia	7	0	0	0.5	0	B M S	-1.0430
Ogygopsis	8	0	1	0.5	1	B S	-0.0857
Olenoides	8	0	0	0	0	B W M S	-1.2252
Family Oryctocephalidae							
Oryctocara	9	0	1	0.5	1	S	-0.0852
Oryctocephalites	11	0	0	1	1	S	-0.5466
Oryctocephalus	7	0	0.5	0.5	1	B	-0.3069
Family Zacanthoididae							
Parkaspis	9	0	0	0	1	B	-0.7201
Thoracocare	2	0	0.5	1	1	S	-0.2790
Zacanthoides	7	0	0	0	0	B W S	-1.2352
Order Ptychopariida							
Family Agraulidae							
Agraulos	12	1	0.5	0.5	1	J	0.3559
Litavkaspis	16	1	0.5	0.5	1	J	0.3782
Skreiaspis	14	1	1	0.5	1	J	0.5351
Family Alokistocaridae							
Alokistocare	17	1	0.5	0.5	1	W	0.3811
Alokistocarella	20	1	1	1	1	B S	0.7894
Altiocculus	31	1	1	0.5	1	W M S	0.7798
Bythicheilus	11	1	0.5	0.5	1	S	0.3655
Chancia	20	1	1	0.5	1	B	0.5937

Ehmaniella	13	1	0.5	0.5	1	B	0.3591
Elrathia	14	1	1	0.5	1	B W M	0.5351
Jenkinsonia	10	1	0	0	1	W M	0.0356
Utaspis	15	1	0	0.5	1	M	0.1892
Family Asaphiscidae							
Asaphiscus	8	1	1	1	1	W M	0.7486
Family Conocoryphidae							
Bailiella	15	1	0.5	1	1	J	0.5568
Conocoryphe	14	1	0.5	0.5	1	J	0.3645
Ctenocephalus	8	1	0.5	1	1	J	0.5401
Parabailiella	12	1	0.5	0.5	0	J	-0.1481
Family Conokephalinidae							
Lobocephalina	15	1	0	0.5	1	J	0.1892
Family Ellipsocephalidae							
Acadolenus	9	1	1	0.5	1	J	0.5344
Ellipsocephalus	12	1	1	0.5	1	J	0.5310
Germaropyge	14	1	1	1	1	J	0.7486
Kingaspis	8	1	0.5	0	1	J	0.1808
Ornamentaspis	12	1	0.5	1	1	J	0.5321
Family Estaingiidae							
Estaingia	15	0	0.5	1	1	E	-0.2271
Family Kingstoniidae							
Brachyaspidion	13	1	0.5	0	1	W M	0.2022
Family Marjumiidae							
Marjumia	12	1	0	1	1	M	0.3855
Modocia	13	1	0	1	1	W M	0.3841
Family Menomonididae							
Bolaspidella	13	0	1	0.5	1	W M	-0.0710
Family Palaeolenidae							
Palaeolenus	10	1	1	1	1	C	0.7469
Family Ptychopariidae							
Ptychoparella	16	1	1	0.5	1	B W M	0.5568
Ptychoparia	14	1	1	0.5	1	J	0.5351
Spencella	13	1	0.5	0.5	1	B	0.3591
Spencia	12	1	0.5	0.5	1	M	0.3559
Syspacephalus	17	1	1	0	1	S	0.5828
Family Solenopleuridae							
Jincella	11	1	1	0.5	1	J	0.5359
Sao	17	1	0.5	1	0	J	0.0078
Family Yunnanocephalidae							
Yunnanocephalus	13	1	0.5	0	1	C	0.2022
Order Redlichiida							
Family Emuellidae							

Holyoakia	12	0	0.5	0	1	E	-0.4588
Familiy Megapharanaspididae							
Megapharanaspis	14	0	0	0	1	E	-0.7008
Family Olenellidae							
Bristolia	8	0	0	0	0	L	-1.2252
Mesonacis	15	0	0	0	0	L	-1.2100
Olenellus	12	0	0	0	0	L	-1.2016
Peachella	8	0	1	0	0	L	-0.9633
Family Paradoxidae							
Acadoparadoxides	18	0	0	0.5	1	J	-0.5255
Eccaparadoxides	16	1	0	0.5	1	J	0.1931
Hydrocephalus	14	0	0.5	0.5	1	J	-0.2729
Paradoxides	19	1	0	0	1	J	0.1136
Family Redlichiidae							
Eoredlichia	10	0	1	0	1	C	-0.2339
Kuanyangia	16	0	0.5	1	0	C	-0.8325
Redlichia	15	0	0.5	0	1	E	-0.4506
Wutingaspis	13	0	0.5	1	1	C	-0.2178
Non-Cambrian trilobites also included							
Order Ptychopariida							
Family Olenidae							
Hypermecaspis	18	1	1	1	1	Bol	0.7767

Note: See Table 2.2 for descriptions of character scores. Locality codes for occurrence: B=Burgess Shale, W=Wheeler Shale, L=Latham Shale, C=Chengjiang, E=Emu Bay Shale, J=Jince, M=Marjum, S=Spence Shale. Locality codes B, W, E, and S correspond to mixed dysoxic localities, others to mostly oxic localities. Additional locality codes for non-Cambrian trilobites: Bol=Bolivia. NMDS1 score reflects the overall similarity of the morphology to an olenimorphic body plan, with high scores being more olenimorphic.

Data adapted from published descriptions by Rasetti (1951), Robison (1962, 1971), Fritz (1971), Oriel and Armstrong (1971), Hintze (1973), White (1973), Hintze and Robison (1975), Palmer and Halley (1979), Mount (1980), Rigby et al. (1983), Aitken and McIlreath (1984), Rogers (1984), Conway Morris (1986), Speyer and Brett (1986), Gunther et al. (1993), Sundberg (1994), Allison et al. (1995), Lehmann et al. (1995), Nedin (1995a, 1995b), Liddell et al. (1997), Fletcher and Collins (1998), Shu et al. (1999), Devereaux (2001), Gaines et al. (2001a, 2001b), Chlupac and Kordule (2002), Fletcher and Collins (2003), Gaines and Droser (2003), Babcock et al. (2004), Parsley and Prokop (2004), Fatka et al. (2004), Caron and Jackson (2008), Garson et al. (2008), Webster et al. (2008), and Brett et al. (2009).

Appendix 2.2. Character scores and NMDS1 scores for trilobites of the Alum Shale.

	Character States					
Genus	**Segments**	**Hypostome attachment**	**Pleural morphology**	**Carapace morphology**	**Exoskeletal ornamentation**	**NMDS1 Score**
Middle Cambrian Trilobites: Mostly Oxic						
Order Asaphida						
Family Anomocaridae						
Anomocare	10	1	1	0.5	1	0.297
Anomocarina	10	1	1	1	1	0.619
Order Ptychopariida						
Family Agraulidae						
Agraulos	12	1	0.5	0.5	1	0.130
Family Conocoryphidae						
Bailiaspis	13	1	1	0.5	1	0.292
Family Solenopleuridae						
Solenopleura	14	1	1	0.5	1	0.303
Order Redlichiida						
Family Centropleuridae						
Centropleura	13	0	1	0	1	-0.298
Family Paradoxidae						
Eccaparadoxides	16	0	0	0.5	1	-0.906
Paradoxides	19	0	0	0	1	-1.160
Upper Cambrian-Lower Ordovician Trilobites: Mixed						
Order Asaphida						
Family Asaphidae						
Eoasaphus	8	1	1	0.5	1	0.302
Niobella	8	1	0.5	0.5	1	0.027

Family Ceratopygidae						
Proceratopyge	10	1	1	0.5	1	0.297
Family Idahoiidae						
Maladioidella	10	1	0	0.5	1	-0.227
Order Ptychopariida						
Family Elviniidae						
Irvingella	12	1	1	0.5	1	0.295
Family Olenidae						
Acerocare	12	1	1	0.5	1	0.295
Ctenopyge	8	1	0	0	1	-0.490
Leptoplastides	11	1	0.5	0.5	1	0.025
Leptoplastus	10	1	0.5	0.5	1	0.022
Olenus	14	1	0.5	0.5	1	0.021
Parabolina	13	1	1	0	1	0.085
Parabolinella	14	1	1	1	1	0.610
Parabolinites	14	1	0.5	0.5	1	0.021
Peltura	12	1	0.5	0	1	-0.266
Protopeltura	8	1	1	0.5	1	0.302
Sphaerophthalmus	10	1	0	0	1	-0.475

Note: Middle Cambrian trilobites represent a mostly oxic assemblage while lower Cambrian to early Ordovician trilobites represent a mixed (more dysoxic) assemblage. See Table 2.2 for description of character states. NMDS1 score reflects the overall similarity of the morphology to an olenimorphic body plan, with high scores being more olenimorphic.

Data adapted from published descriptions by Berg-Madsen (1985), Clarkson and Taylor (1995), and Terfelt et al. (2011)

Appendix 2.3. NMDS scores of all trilobites from both datasets, before and after removal of segmentation from the NMDS model, with the net shift along each axis.

Genus	Scores with segmentation		Scores without segmentation		Shift in NMDS1	Shift in NMDS2
	NMDS1	**NMDS2**	**NMDS1**	**NMDS2**		
Alum Shale dataset						
Acerocare	0.295	-0.092	0.216	-0.157	-0.079	-0.065
Agraulos	0.013	0.144	0.071	0.247	0.058	0.103
Anomocare	0.297	-0.086	0.216	-0.157	-0.081	-0.071
Anomocarina	0.619	0.060	0.695	-0.045	0.076	-0.105
Bailiaspis	0.292	-0.097	0.216	-0.157	-0.077	-0.060
Centropleura	-0.298	-0.806	-0.329	-0.836	-0.031	-0.030
Ctenopyge	-0.490	0.426	-0.441	0.359	0.049	-0.068
Eccaparadoxides	-0.905	-0.256	-1.032	-0.181	-0.126	0.075
Eoasaphus	0.302	-0.088	0.216	-0.157	-0.087	-0.069
Irvingella	0.295	-0.092	0.216	-0.157	-0.079	-0.065
Leptoplastides	0.023	0.152	0.071	0.247	0.049	0.095
Leptoplastus	0.022	0.156	0.071	0.247	0.050	0.091
Maladioidella	-0.227	0.457	-0.414	0.376	-0.187	-0.080
Niobella	0.027	0.170	0.071	0.247	0.044	0.077
Olenus	0.021	0.147	0.071	0.247	0.050	0.100
Parabolina	0.085	-0.390	0.120	-0.247	0.035	0.143
Parabolinella	0.610	0.054	0.695	-0.045	0.085	-0.099
Parabolinites	0.021	0.147	0.071	0.247	0.050	0.100
Paradoxides	-1.160	-0.185	-1.013	-0.261	0.147	-0.077
Peltura	-0.267	0.027	0.006	0.292	0.273	0.266
Proceratopyge	0.297	-0.086	0.216	-0.157	-0.081	-0.071
Protopeltura	0.302	-0.088	0.216	-0.157	-0.087	-0.069
Solenopleura	0.303	-0.106	0.216	-0.157	-0.087	-0.051
Sphaerophthalmus	-0.475	0.430	-0.441	0.359	0.034	-0.072
Early-to-middle Cambrian dataset						
Acadolenus	0.534	0.152	0.589	0.139	0.055	-0.013
Acadoparadoxides	-0.526	0.068	-0.508	0.099	0.018	0.031
Agraulos	0.356	-0.128	0.352	-0.149	-0.004	-0.021
Alokistocare	0.381	-0.141	0.352	-0.149	-0.029	-0.008
Alokistocarella	0.789	0.046	0.732	0.093	-0.057	0.047
Altiocculus	0.780	0.231	0.589	0.139	-0.191	-0.092
Asaphiscus	0.749	0.072	0.732	0.093	-0.017	0.021
Bailiella	0.557	-0.236	0.530	-0.229	-0.027	0.007
Bathyuriscus	0.340	-0.115	0.352	-0.149	0.012	-0.034

Bolaspidella	-0.071	0.615	-0.069	0.625	0.002	0.010
Brachyaspidion	0.202	-0.197	0.333	-0.174	0.131	0.023
Bristolia	-1.225	-0.093	-1.253	-0.150	-0.028	-0.057
Bythicheilus	0.365	-0.126	0.352	-0.149	-0.013	-0.023
Chancia	0.594	0.151	0.589	0.139	-0.004	-0.012
Conocoryphe	0.364	-0.123	0.352	-0.149	-0.012	-0.026
Ctenocephalus	0.540	-0.248	0.530	-0.229	-0.010	0.019
Dorypyge	-1.044	-0.591	-1.100	-0.501	-0.056	0.091
Eccaparadoxides	0.193	-0.455	0.263	-0.441	0.070	0.013
Ehmaniella	0.359	-0.130	0.352	-0.149	-0.007	-0.019
Ellipsocephalus	0.531	0.133	0.589	0.139	0.058	0.006
Elrathia	0.535	0.136	0.589	0.139	0.054	0.003
Eoredlichia	-0.234	0.766	-0.242	0.762	-0.008	-0.004
Estaingia	-0.227	0.409	-0.283	0.330	-0.056	-0.078
Germaropyge	0.749	0.043	0.732	0.093	-0.017	0.050
Glossopleura	-1.046	-0.540	-1.100	-0.501	-0.054	0.039
Hanburia	-0.093	0.660	-0.069	0.625	0.024	-0.035
Hemirhodon	0.034	0.791	-0.003	0.714	-0.038	-0.077
Holyoakia	-0.459	0.374	-0.430	0.450	0.029	0.075
Hydrocephalus	-0.273	0.295	-0.295	0.313	-0.022	0.018
Hypermecaspis	0.777	0.049	0.732	0.093	-0.045	0.044
Jenkinsonia	0.036	-0.556	0.084	-0.508	0.049	0.048
Jincella	0.536	0.144	0.589	0.139	0.053	-0.005
Kingaspis	0.181	-0.192	0.333	-0.174	0.152	0.018
Kootenia	-1.043	-0.310	-1.067	-0.296	-0.024	0.014
Kuanyangia	-0.833	-0.526	-0.875	-0.467	-0.042	0.059
Litavkaspis	0.378	-0.135	0.352	-0.149	-0.026	-0.014
Lobocephalina	0.189	-0.447	0.263	-0.441	0.074	0.005
Marjumia	0.386	-0.601	0.327	-0.581	-0.059	0.020
Megapharanaspis	-0.701	0.197	-0.691	0.213	0.010	0.016
Mesonacis	-1.210	-0.119	-1.253	-0.150	-0.043	-0.031
Modocia	0.384	-0.595	0.327	-0.581	-0.058	0.014
Ogygopsis	-0.086	0.633	-0.069	0.625	0.017	-0.007
Olenellus	-1.201	-0.123	-1.253	-0.150	-0.052	-0.027
Olenoides	-1.225	-0.093	-1.253	-0.150	-0.028	-0.057
Ornamentaspis	0.532	-0.243	0.530	-0.229	-0.002	0.015
Orria	-0.086	0.633	-0.069	0.625	0.017	-0.007
Oryctocara	-0.085	0.630	-0.069	0.625	0.016	-0.004
Oryctocephalites	-0.547	-0.112	-0.534	-0.008	0.013	0.104
Oryctocephalus	-0.307	0.306	-0.295	0.313	0.012	0.007
Palaeolenus	0.747	0.060	0.732	0.093	-0.015	0.033
Parabailiella	-0.148	-0.775	-0.184	-0.777	-0.036	-0.001
Paradoxides	0.114	-0.615	0.084	-0.508	-0.029	0.107

Parkaspis	-0.720	0.217	-0.691	0.213	0.029	-0.004
Peachella	-0.963	0.691	-1.017	0.686	-0.054	-0.006
Ptychoparella	0.557	0.131	0.589	0.139	0.033	0.008
Ptychoparia	0.535	0.136	0.589	0.139	0.054	0.003
Redlichia	-0.450	0.364	-0.430	0.450	0.021	0.086
Sao	0.007	-0.978	0.033	-0.981	0.026	-0.003
Skreiaspis	0.535	0.136	0.589	0.139	0.054	0.003
Spencella	0.359	-0.130	0.352	-0.149	-0.007	-0.019
Spencia	0.356	-0.128	0.352	-0.149	-0.004	-0.021
Syspacephalus	0.583	0.377	0.559	0.289	-0.024	-0.088
Thoracocare	-0.279	0.519	-0.283	0.330	-0.004	-0.189
Utaspis	0.189	-0.447	0.263	-0.441	0.074	0.005
Wutingaspis	-0.218	0.393	-0.283	0.330	-0.066	-0.062
Yunnanocephalus	0.202	-0.197	0.333	-0.174	0.131	0.023
Zacanthoides	-1.235	-0.110	-1.253	-0.150	-0.018	-0.040

Appendix 2.4. R code for NMDS analysis.

```
#Prepare a dataset for MDS analysis
trilo.mds <- trilo1

#Start MDS and generate scree plot of stress as dimensionality increases
library(vegan)
trilo.mds.1 <- metaMDS(trilo.mds, distance="euclidean", k=1, autotransform=FALSE, noshare=FALSE)
trilo.mds.2 <- metaMDS(trilo.mds, distance="euclidean", k=2, autotransform=FALSE, noshare=FALSE)
trilo.mds.3 <- metaMDS(trilo.mds, distance="euclidean", k=3, autotransform=FALSE, noshare=FALSE)
trilo.mds.4 <- metaMDS(trilo.mds, distance="euclidean", k=4, autotransform=FALSE, noshare=FALSE)
dev.new()
barplot(c(trilo.mds.1$stress, trilo.mds.2$stress, trilo.mds.3$stress, trilo.mds.4$stress), xlab="Dimensions",
ylab="Stress", names.arg=1:4, las=1)

#Plot the MDS analyses
dev.new()
trilo.mds.2$points[,1] <- trilo.mds.2$points[,1]*-1
t.points <- trilo.mds.2$points
#Segment score
plot(trilo.mds.2, type="t", display=c("species"), las=1, xlim=c(min(t.points[1:length(segments)])-.25,
max(t.points[1:length(segments)])+.5))
points(t.points[seg.score==2,], pch=2, col="blue", cex=1)
points(t.points[seg.score==0,], pch=17, col="orange", cex=1)
points(t.points[seg.score==1,], pch=9, col="violet", cex=1)
points(mean(t.points[seg.score==2,1]), mean(t.points[seg.score==2,2]), pch=4, lwd=2, cex=1.5)
points(mean(t.points[seg.score==0,1]), mean(t.points[seg.score==0,2]), pch=4, lwd=2, cex=1.5)
points(mean(t.points[seg.score==1,1]), mean(t.points[seg.score==1,2]), pch=4, lwd=2, cex=1.5)
legend(.45, -0.8, c("High # Segments","Med # Segments","Low # Segments", "Centroids"),
pch=c(2,9,17,4), col=c("blue","violet","orange","black"))
#Carapace morphology
dev.new()
```

```
plot(trilo.mds.2, type="t", display=c("species"), las=1, xlim=c(min(t.points[1:length(segments)])-.25,
max(t.points[1:length(segments)])+.5))
points(t.points[carap.morph==1,], pch=2, col="blue", cex=1)
points(t.points[carap.morph==0,], pch=17, col="orange", cex=1)
points(t.points[carap.morph==.5,], pch=9, col="violet", cex=1)
points (mean(t.points[carap.morph==1,1]), mean(t.points[carap.morph==1,2]), pch=4, lwd=2, cex=1.5)
points (mean(t.points[carap.morph==0,1]), mean(t.points[carap.morph==0,2]), pch=4, lwd=2, cex=1.5)
points (mean(t.points[carap.morph==.5,1]), mean(t.points[carap.morph==.5,2]), pch=4, lwd=2)
legend(.34, -.8, c("Flat Carapace","Arched Carapace","Highly Arched Carap.", "Centroids"),
pch=c(2,9,17,4), col=c("blue","violet","orange","black"))
#Pleural morphology
dev.new()
plot(trilo.mds.2, type="t", display=c("species"), las=1, xlim=c(min(t.points[1:length(segments)])-.25,
max(t.points[1:length(segments)])+.5))
points(t.points[pleur.morph==1,], pch=2, col="blue", cex=1)
points(t.points[pleur.morph==0,], pch=17, col="orange", cex=1)
points(t.points[pleur.morph==.5,], pch=9, col="violet", cex=1)
points (mean(t.points[pleur.morph==1,1]), mean(t.points[pleur.morph==1,2]), pch=4, lwd=2, cex=1.5)
points (mean(t.points[pleur.morph==0,1]), mean(t.points[pleur.morph==0,2]), pch=4, lwd=2, cex=1.5)
points (mean(t.points[pleur.morph==.5,1]), mean(t.points[pleur.morph==.5,2]), pch=4, lwd=2)
legend(.45, -.8, c("Flat Pleurae","Arched Pleurae","Arched and Spiny", "Centroids"), pch=c(2,9,17,4),
col=c("blue","violet","orange","black"))
#Hypostome attachment
dev.new()
plot(trilo.mds.2, type="t", display=c("species"), las=1, xlim=c(min(t.points[1:length(segments)])-.25,
max(t.points[1:length(segments)])+.5))
points(t.points[hypost.att==1,], pch=2, col="blue", cex=1)
points(t.points[hypost.att==0,], pch=17, col="orange", cex=1)
points (mean(t.points[hypost.att==1,1]), mean(t.points[hypost.att==1,2]), pch=4, lwd=2, cex=1.5)
points (mean(t.points[hypost.att==0,1]), mean(t.points[hypost.att==0,2]), pch=4, lwd=2, cex=1.5)
legend(.25, -.8, c("Non-Attached Hypostome", "Attached Hypostome", "Centroids"), pch=c(2,17,4),
col=c("blue","orange","black"))
#Ornamentation
dev.new()
plot(trilo.mds.2, type="t", display=c("species"), las=1, xlim=c(min(t.points[1:length(segments)])-.25,
max(t.points[1:length(segments)])+.5))
points(t.points[exosk.ornam==1,], pch=2, col="blue", cex=1)
points(t.points[exosk.ornam==0,], pch=17, col="orange", cex=1)
points (mean(t.points[exosk.ornam==1,1]), mean(t.points[exosk.ornam==1,2]), pch=4, lwd=2, cex=1.5)
points (mean(t.points[exosk.ornam==0,1]), mean(t.points[exosk.ornam==0,2]), pch=4, lwd=2, cex=1.5)
legend(.45, -.8, c("Not Ornamented","Ornamented", "Centroids"), pch=c(2,17,4),
col=c("blue","orange","black"))
dev.new()
plot(trilo.mds.2, type="n", display=c("species"), las=1, xlim=c(min(t.points[1:length(segments)])-.25,
max(t.points[1:length(segments)])+.5))
points(t.points[,1], t.points[,2], col="black", pch=16, cex=.5)
points(t.points[row.names(t.points)=="Elrathia",1], t.points[row.names(t.points)=="Elrathia",2], pch=17,
cex=1.5)
points(t.points[row.names(t.points)=="Hypermecaspis",1],
t.points[row.names(t.points)=="Hypermecaspis",2], pch=2, cex=1.5)
points(t.points[row.names(t.points)=="Olenellus",1], t.points[row.names(t.points)=="Olenellus",2], pch=9,
cex=1.5)
points(.76, .4727, pch=1, cex=1.5)
points(-.4651, .3558, pch=3, cex=1.5)
points(-.4727, .3646, pch=4, cex=1.5)
```

```
legend(.55, -.5, c("Hypermecaspis","Elrathia","Olenellus","Triarthrus","Phacops","Greenops"),
pch=c(2,17,9,1,3,4))
#Order
dev.new()
plot(trilo.mds.2, type="n", display=c("species"), las=1, xlim=c(min(t.points[1:length(segments)])-.25,
max(t.points[1:length(segments)])+.5))
points(t.points[trilo1$Order=="Corynexochida",1], t.points[trilo1$Order=="Corynexochida",2], pch=4,
col="orange", cex=1)
points(t.points[trilo1$Order=="Ptychopariida",1], t.points[trilo1$Order=="Ptychopariida",2], pch=2,
col="blue", cex=1)
points(t.points[trilo1$Order=="Redlichiida",1], t.points[trilo1$Order=="Redlichiida",2], pch=9,
col="violet", cex=1)
legend(.45, -.8, c("Ptychopariida","Corynexochida","Redlichiida"), pch=c(2,4,9),
col=c("blue","orange","violet"))
#Environment, Ptychs
dev.new()
plot(trilo.mds.2, type="n", display=c("species"), las=1, xlim=c(min(t.points[1:length(segments)])-.25,
max(t.points[1:length(segments)])+.5))
points(t.points[trilo1$Order=="Ptychopariida"&trilo1$LOC=="1",1],
t.points[trilo1$Order=="Ptychopariida"&trilo1$LOC=="1",2], pch=9, col="blue", cex=1)
points (mean(t.points[trilo1$Order=="Ptychopariida"&trilo1$LOC==1,1]),
mean(t.points[trilo1$Order=="Ptychopariida"&trilo1$LOC==1,2]), pch=4, lwd=2, cex=1.5)
points(t.points[trilo1$Order=="Ptychopariida"&trilo1$LOC==0,1],
t.points[trilo1$Order=="Ptychopariida"&trilo1$LOC==0,2], pch=2, col="orange", cex=1)
points (mean(t.points[trilo1$Order=="Ptychopariida"&trilo1$LOC==0,1]),
mean(t.points[trilo1$Order=="Ptychopariida"&trilo1$LOC==0,2]), pch=4, lwd=2, cex=1.5)
legend(.45, -.8, c("Mixed","Mostly Oxic","Centroids"), pch=c(2,9,4), col=c("orange","blue","black"))
#Environment, Reds
dev.new()
plot(trilo.mds.2, type="n", display=c("species"), las=1, xlim=c(min(t.points[1:length(segments)])-.25,
max(t.points[1:length(segments)])+.5))
points(t.points[trilo1$Order=="Corynexochida"&trilo1$LOC=="1",1],
t.points[trilo1$Order=="Corynexochida"&trilo1$LOC=="1",2], pch=9, col="blue", cex=1)
points (mean(t.points[trilo1$Order=="Corynexochida"&trilo1$LOC==1,1]),
mean(t.points[trilo1$Order=="Corynexochida"&trilo1$LOC==1,2]), pch=4, lwd=2, cex=1.5)
points(t.points[trilo1$Order=="Corynexochida"&trilo1$LOC==0,1],
t.points[trilo1$Order=="Corynexochida"&trilo1$LOC==0,2], pch=2, col="orange", cex=1)
points (mean(t.points[trilo1$Order=="Corynexochida"&trilo1$LOC==0,1]),
mean(t.points[trilo1$Order=="Corynexochida"&trilo1$LOC==0,2]), pch=4, lwd=2, cex=1.5)
legend(.45, -.8, c("Mixed","Mostly Oxic","Centroids"), pch=c(2,9,4), col=c("orange","blue","black"))
#Environment, Corys
dev.new()
plot(trilo.mds.2, type="n", display=c("species"), las=1, xlim=c(min(t.points[1:length(segments)])-.25,
max(t.points[1:length(segments)])+.5))
points(t.points[trilo1$Order=="Redlichiida"&trilo1$LOC=="1",1],
t.points[trilo1$Order=="Redlichiida"&trilo1$LOC=="1",2], pch=9, col="blue", cex=1)
points (mean(t.points[trilo1$Order=="Redlichiida"&trilo1$LOC==1,1]),
mean(t.points[trilo1$Order=="Redlichiida"&trilo1$LOC==1,2]), pch=4, lwd=2, cex=1.5)
points(t.points[trilo1$Order=="Redlichiida"&trilo1$LOC==0,1],
t.points[trilo1$Order=="Redlichiida"&trilo1$LOC==0,2], pch=2, col="orange", cex=1)
points (mean(t.points[trilo1$Order=="Redlichiida"&trilo1$LOC==0,1]),
mean(t.points[trilo1$Order=="Redlichiida"&trilo1$LOC==0,2]), pch=4, lwd=2, cex=1.5)
legend(.45, -.8, c("Mixed","Mostly Oxic","Centroids"), pch=c(2,9,4), col=c("orange","blue","black"))
#Get MDS loadings
trilo.mds.2$species
```

```
#Plot distribution along MDS1
dev.new()
hist(t.points[,1], xlab="NMDS1", main="All genera", xlim=c(min(t.points[1:length(segments)])-.5,
max(t.points[1:length(segments)])+1), ylim=c(0,15), xaxt="n")
axis(1, at=trilo1$breaks, line=-.95)
segments(-2,0,1.5,0)
dev.new()
hist(t.points[trilo1$Order=="Ptychopariida",1], xlab="NMDS1", main="Ptychopariida",
xlim=c(min(t.points[1:length(segments)])-.5, max(t.points[1:length(segments)])+1), ylim=c(0,15),
xaxt="n")
axis(1, at=trilo1$breaks, line=-.95)
segments(-2,0,1.5,0)
dev.new()
hist(t.points[trilo1$Order=="Corynexochida",1], xlab="NMDS1", main="Corynexochida",
xlim=c(min(t.points[1:length(segments)])-.5, max(t.points[1:length(segments)])+1), ylim=c(0,15),
breaks=8, xaxt="n")
axis(1, at=trilo1$breaks, line=-.95)
segments(-2,0,1.5,0)
dev.new()
hist(t.points[trilo1$Order=="Redlichiida",1], xlab="NMDS1", main="Redlichiida",
xlim=c(min(t.points[1:length(segments)])-.5, max(t.points[1:length(segments)])+1), ylim=c(0,15),
breaks=8, xaxt="n")
axis(1, at=trilo1$breaks, line=-.95)
segments(-2,0,1.5,0)
dev.new()
hist(t.points[trilo1$LOC=="1",1], xlab="NMDS1", main="Mixed Genera",
xlim=c(min(t.points[1:length(segments)])-.5, max(t.points[1:length(segments)])+1), ylim=c(0,15),
breaks=11, xaxt="n")
abline(v=mean(trilo1$NMDS1[trilo1$LOC=="1"]),,col="red", lty=2)
abline(v=median(trilo1$NMDS1[trilo1$LOC=="1"]),,col="red", lty=3)
axis(1, at=trilo1$breaks, line=-.95)
segments(-2,0,1.5,0)
dev.new()
hist(t.points[trilo1$LOC=="0",1], xlab="NMDS1", main="Mostly-oxic Genera",
xlim=c(min(t.points[1:length(segments)])-.5, max(t.points[1:length(segments)])+1), ylim=c(0,15),
xaxt="n")
abline(v=mean(trilo1$NMDS1[trilo1$LOC=="0"]),,col="red", lty=2)
abline(v=median(trilo1$NMDS1[trilo1$LOC=="0"]),,col="red", lty=3)
axis(1, at=trilo1$breaks, line=-.95)
segments(-2,0,1.5,0)

#Calculate correlation coefficients between variables and NMDS1
cor(trilo1, method="spearman") #pairwise correlations between characters
cor.test(trilo1[,1], t.points[,1], method="spearman") #correlations between characters and NMDS1, with p-
value
cor.test(trilo1[,3], t.points[,1], method="spearman")
cor.test(trilo1[,4], t.points[,1], method="spearman")
cor.test(trilo1[,5], t.points[,1], method="spearman")
cor.test(trilo1[,6], t.points[,1], method="spearman")

#Kruskal-Wallis test between variables and LOCs
kruskal.test(trilo1$LOC~trilo1$segments)
kruskal.test(trilo1$LOC~trilo1$hypost.att)
kruskal.test(trilo1$LOC~trilo1$carap.morph)
kruskal.test(trilo1$LOC~trilo1$pleur.morph)
kruskal.test(trilo1$LOC~trilo1$exosk.ornam)
```

```
#Welch two-sample t-test between taxonomic orders
t.test(trilo1$NMDS1[trilo1$Order=="Corynexochida"], trilo1$NMDS1[trilo1$Order=="Redlichiida"])
t.test(trilo1$NMDS1[trilo1$Order=="Ptychopariida"], trilo1$NMDS1[trilo1$Order=="Redlichiida"])
t.test(trilo1$NMDS1[trilo1$Order=="Corynexochida"], trilo1$NMDS1[trilo1$Order=="Ptychopariida"])

#Welch two-sample t-test between oxic/dysoxic
t.test(trilo1$NMDS1[trilo1$LOC=="0"], trilo1$NMDS[trilo1$LOC=="1"])

#Welch two-sample t-test between oxic ptychs/dysoxic ptychs
t.test(trilo1$NMDS1[trilo1$LOC=="0"&trilo1$Order=="Ptychopariida"],
trilo1$NMDS[trilo1$LOC=="1"&trilo1$Order=="Ptychopariida"])

#One-sample T-tests
t.test(trilo1$NMDS1[trilo1$Order=="Ptychopariida"])
t.test(trilo1$NMDS1[trilo1$Order=="Ptychopariida"&trilo1$NMDS>0.4908])

#Determine number of clusters
dev.new()
wss <- (nrow(t.points)-1)*sum(apply(t.points,2,var))
 for (i in 2:15) wss[i] <- sum(kmeans(t.points,
    centers=i)$withinss)
 plot(1:15, wss, type="b", xlab="Number of Clusters",
   ylab="Within groups sum of squares")

#run K-means analysis
km <- kmeans(t.points, centers=6, nstart=20, iter.max=100)

#plot K-means results
dev.new()
plot(trilo.mds.2, type="n", display=c("species"), las=1, xlim=c(min(t.points[1:length(segments)])-.25,
max(t.points[1:length(segments)])+.5))
points(t.points[km$cluster==1,1], t.points[km$cluster==1,2], pch=4, col="orange", cex=1)
points(t.points[km$cluster==2,1], t.points[km$cluster==2,2], pch=5, col="red", cex=1)
points(t.points[km$cluster==3,1], t.points[km$cluster==3,2], pch=6, col="purple", cex=1)
points(t.points[km$cluster==4,1], t.points[km$cluster==4,2], pch=3, col="blue", cex=1)
points(t.points[km$cluster==5,1], t.points[km$cluster==5,2], pch=8, col="green", cex=1)
points(t.points[km$cluster==6,1], t.points[km$cluster==6,2], pch=9, col="brown", cex=1)

#Logistic Regression of Environment Type as a function of NMDS1 scores
lr <- glm(trilo1$LOC~trilo1$NMDS1, family="binomial")
summary(lr)
layout(matrix(1:4,2,2))
plot(lr)
```

Appendix 3.1. Supplementary methods for biomarker analyses.

Trilobites were quarried commercially from the middle Cambrian Wheeler Shale by professional collectors (West Desert Collectors and Terra Trilobites, Delta UT) from rock depths up to 5 meters representing rock with little, if any, weathering. Two specimens of *Elrathia* and 16 *Peronopsis* with robust and complete exoskeletons were used (Fig. 3.1). The 16 *Peronopsis* were combined into two sets of eight for analysis, to yield a comparable sample mass to the *Elrathia* and ensure sufficient material for analysis. Because compounds from anthropogenic polymers are particularly pervasive, to minimize plastic contamination, two additional *Elrathia kingii* and five *Peronopsis*, both with associated sediment, were collected and protected from contact with any type of plastics during extraction, shipping, and handling. The five protected *Peronopsis* were combined for analysis, but did not yield any compounds above the detection limit, despite repeated tests on the sample material, and thus these samples could not be interpreted.

Total carbon for sediments was determined by powdering sediment samples associated with both trilobite species in a Spex 8000 ball mill to produce approximately 20 ml of powdered sediment. 100 mg of these powders were weighed into a crucible boat and fired on an Eltra furnace to 1350°C under a pure oxygen atmosphere. The resultant carbon dioxide was measured by infrared absorption on an Eltra CS500 determinator to yield the total weight percent carbon in the sample. Total inorganic carbon was then determined by weighing another 100 mg of the same sample powder into a 250 ml flask and mixing with 10 ml of ethanol, then connecting the flask to an Eltra CS500 determinator, adding 10 ml of 20% HCl and heating to 50°C, and measuring the resultant carbon dioxide as above. Total organic carbon was determined by subtracting

the inorganic carbon from the total carbon for each sample, and averaging values by species. Carbon and inorganic carbon analysis was performed at the Lyons Lab at UC Riverside.

Sediment and exoskeletal samples were prepared for multibiomarker analysis by GC-MS, yielding a profile of individual biomarkers present in each sample, following a multibiomarker method established by Medeiros and Simoneit (Medeiros and Simoneit, 2007, 2008a, 2008b) and Simoneit et al. (2014). This method allows for a simultaneous characterization of the different chemical classes spanning a wide range of polarities, without a need to isolate certain chemical classes before analysis. Protected samples were rinsed with Milli-Q water upon arrival, and after drying, they were gently rinsed with dichloromethane followed by methanol and left to dry again at room temperature. All samples were powdered in a solvent pre-cleaned ball mill and then weighed in a pre-combusted (450°C for 5 h) beaker. Samples were then sonicated twice for 15 min in a 30 mL mixture of dichloromethane:methanol (2:1, v/v). The extract aliquots were combined and filtered using a Gelman Swinney filtration unit containing an annealed pre-combusted glass fiber filter (42.5 mm, Whatman) for the removal of insoluble particles. The filtrate was first concentrated in a RapidVap (solvent evaporation system) to about 1.5 mL, then further to 500 μL using a stream of high-purity nitrogen. Aliquots of the total extracts were evaporated completely using a stream of filtered nitrogen gas, and then converted to their trimethylsilyl derivatives using BSTFA containing 1% TMCS and pyridine for 3 h at 70°C. Immediately before GC-MS analysis, derivatized extracts were evaporated to dryness using nitrogen gas and redissolved in hexane for injection.

Aliquots of 1 μL of silylated total extracts were analyzed within 24 hours using a HP 6890 gas chromatograph interfaced with a HP 5975 mass selective detector (GC-MS). A DB5-MS capillary column (30 m x 0.25 mm I.D. and film thickness of 0.25 μm) was used with helium as the carrier gas at a constant flow rate of 1.3 mL min^{-1}. The injector and MS source temperatures were maintained at 280°C and 230°C, respectively. The column temperature program consisted of injection at 65°C and hold for 2 min, temperature increase of 6°C min^{-1} to 300°C, followed by an isothermal hold at 300°C for 15 min. The MS was operated in the electron impact mode with an ionization energy of 70 eV. The scan range was set from 50 to 650 Da and the samples were analyzed in splitless mode.

Data were acquired and processed with the HP-Chemstation software. Individual compounds were identified by comparison of mass spectra with literature and library data, comparison of mass spectra and GC retention times with those of authentic standards and/or interpretation of mass spectrometric fragmentation patterns. Compounds were quantified using the total ion current (TIC) peak area, and converted to compound mass using calibration curves of external standards: *n*-eicosene for *n*-alkanes, isoprenoids, UCM, and phthalates; *n*-hexadecanoic acid for *n*-alkanoic acids, *n*-alkanols and glyceride derivatives; lupeol for diterpenoids, sterols and lignin derivatives; glucose for monosaccharides; sucrose for disaccharides. A procedural blank was run in sequence to samples, presenting no significant background interferences.

Appendix 3.2. Concentrations (10^{-9}g g^{-1}) of biomarkers and other chemical compounds present in middle Cambrian Wheeler Shale trilobites and sediment samples. Samples include exoskeletal material (exos.) from *Elrathia kingii* (*Elr*) and *Peronopsis* (*Per*), and sediments (sed.) associated with both trilobites and from the broader Wheeler Shale (WS). Protected samples were guarded against contact with plastics during collection and transport.

	Unprotected samples						Protected samples				
	Elr exos.	*Elr* exos.	*Per* exos.	*Per* exos.	WS sed.	WS sed.	*Elr* exos.	*Elr* exos.	*Elr* sed.	*Elr* sed.	*Per* sed.
Chemical Class Individual Compound											
***n*-Alkanes**											
Heptadecane	0.0	0.0	0.0	0.0	13.1	0.0	0.0	0.0	0.0	0.0	0.0
Octadecane	0.0	0.0	0.0	0.0	41.7	6.7	0.0	14.1	0.0	0.0	1.7
Nonadecane	0.0	0.0	0.0	0.0	37.0	12.2	0.0	0.0	0.0	0.0	0.0
Eicosane	0.0	0.0	0.0	0.0	0.0	11.4	0.0	0.0	0.0	0.0	4.3
Tetracosane	62.6	33.4	96.0	334.1	0.0	0.0	0.0	0.0	0.0	0.0	0.0
Pentacosane	49.6	37.3	142.3	543.4	0.0	12.1	0.0	0.0	0.0	0.0	0.0
Hexacosane	82.8	44.4	147.1	817.6	0.0	0.0	0.0	0.0	0.0	0.0	0.0
Heptacosane	61.8	29.9	91.4	729.4	0.0	0.0	0.0	0.0	0.0	0.0	0.0
Octacosane	38.4	22.8	71.8	599.2	0.0	0.0	0.0	0.0	0.0	0.0	0.0
Nonacosane	35.2	15.0	0.0	453.2	0.0	0.0	0.0	0.0	0.0	0.0	0.0
Triacontane	19.9	10.4	0.0	324.5	0.0	0.0	0.0	0.0	0.0	0.0	0.0
Total	**350.2**	**193.1**	**548.6**	**3801.4**	**91.9**	**42.3**	**0.0**	**14.1**	**0.0**	**0.0**	**6.0**
CPI[a]	**0.7**	**0.7**	**0.7**	**0.8**	**-**	**-**	**-**	**-**	**-**	**-**	**-**

***n*-Alkanols**											
Dodecanol	0.0	0.0	0.0	0.0	8.5	0.0	0.0	0.0	0.0	0.0	0.8
Tetradecanol	0.0	0.0	0.0	0.0	36.0	8.4	3.0	0.0	0.0	0.0	4.0
Eicosanol	0.0	0.0	0.0	0.0	0.0	0.0	0.0	0.0	0.0	0.0	2.5
Docosanol	0.0	0.0	0.0	0.0	0.0	0.0	0.0	0.0	0.0	0.0	2.8
Tetracosanol	0.0	0.0	0.0	0.0	0.0	0.0	0.0	0.0	0.0	0.0	5.4
Hexacosanol	0.0	5.9	0.0	0.0	81.6	32.5	19.2	0.0	0.0	0.0	18.4
Octacosanol	0.0	14.2	0.0	0.0	22.7	30.7	12.9	7.0	1.8	0.0	23.0
Total	**0.0**	**20.1**	**0.0**	**0.0**	**148.7**	**71.7**	**35.1**	**7.0**	**1.8**	**0.0**	**56.9**
***n*-Alkanoic acids**											
Nonanoic acid	0.0	0.0	0.0	0.0	0.0	4.4	0.0	0.0	0.0	0.0	0.0
Tridecanoic acid	0.0	2.7	0.0	0.0	0.0	0.0	0.0	0.0	0.0	0.0	0.0
Tetradecanoic acid	0.0	5.9	0.0	0.0	13.1	0.0	0.0	4.1	0.0	0.0	1.0
Hexadecanoic acid	146.2	284.2	734.1	353.4	87.1	68.8	71.8	83.5	5.9	26.0	10.6
Octadecanoic acid	72.1	172.6	311.6	194.0	12.1	53.2	16.8	30.0	1.2	11.9	3.0
Total	**218.3**	**465.4**	**1045.8**	**547.5**	**112.4**	**126.3**	**88.6**	**117.7**	**7.2**	**38.0**	**14.6**
Isoprenoids											
Squalene	0.0	47.6	0.0	0.0	28.8	38.9	100.0	71.4	2.6	14.4	71.3
Diterpenoids											
Dehydroabietic acid	0.0	0.0	0.0	0.0	3.1	2.9	3.8	1.8	1.2	0.9	2.5
Steroids											
Cholesterol	0.0	0.0	0.0	0.0	90.4	31.7	64.7	37.4	2.0	11.9	44.2
Stigmasterol	0.0	0.0	0.0	0.0	0.0	0.0	0.0	0.0	0.0	0.0	5.2
Sitosterol	0.0	0.0	0.0	0.0	0.0	10.3	0.0	0.0	0.0	0.0	0.0
Total	**0.0**	**0.0**	**0.0**	**0.0**	**90.4**	**41.9**	**64.7**	**37.4**	**2.0**	**11.9**	**49.5**

Lignin derivatives											
Vanillin	0.0	0.0	0.0	0.0	2.7	0.0	0.0	0.0	0.0	0.0	3.9
3-Methoxy-Benzaldehyde	0.0	0.0	0.0	0.0	0.0	0.0	0.0	0.0	0.0	0.0	8.2
Total	**0.0**	**0.0**	**0.0**	**0.0**	**2.7**	**0.0**	**0.0**	**0.0**	**0.0**	**0.0**	**12.1**
Saccharides											
α- + β-Glucose	0.0	0.0	0.0	0.0	222.0	244.0	401.5	146.9	2315.1	5513.1	2.7
α- + β-Fructose	0.0	0.0	0.0	0.0	0.0	0.0	0.0	0.0	220.1	900.4	0.0
Dulcitol	0.0	0.0	0.0	0.0	0.0	0.0	0.0	0.0	40.3	209.2	0.0
myo-Inositol	0.0	0.0	0.0	0.0	35.2	15.0	0.0	0.0	0.0	0.0	0.0
scillo-Inositol	0.0	0.0	0.0	0.0	13.8	10.5	4.8	0.0	0.0	0.0	0.0
Levoglucosan	0.0	0.0	90.2	7.0	3.1	1.7	2.3	1.3	14.9	16.6	1.2
Sucrose	0.0	0.0	0.0	0.0	233.1	146.5	0.0	28.0	4.8	40.1	2.1
Mycose	0.0	0.0	0.0	0.0	0.0	10.8	0.0	0.0	0.0	0.0	0.0
Total	**0.0**	**0.0**	**90.2**	**7.0**	**507.2**	**428.4**	**408.5**	**176.3**	**2595.1**	**6679.4**	**5.9**
Glyceride derivatives											
Glycerol	0.0	0.0	0.0	0.0	0.0	8.7	0.0	0.0	0.0	0.0	0.0
1-*O*-Hexadecanoyl glycerol	0.0	0.0	0.0	0.0	30.5	4.8	19.5	12.4	0.0	0.0	6.5
1-*O*-Octadecanoyl glycerol	0.0	0.0	0.0	0.0	2.4	2.6	0.0	0.0	0.0	0.0	1.1
Total	**0.0**	**0.0**	**0.0**	**0.0**	**32.9**	**16.2**	**19.5**	**12.4**	**0.0**	**0.0**	**7.6**
Amides											
Benzamide	0.0	0.0	0.0	0.0	10.5	0.0	0.0	0.0	0.0	0.0	0.0
m-Toluamide	0.0	0.0	0.0	0.0	0.0	8.5	0.0	0.0	0.0	0.0	0.0
Total	**0.0**	**0.0**	**0.0**	**0.0**	**10.5**	**8.5**	**0.0**	**0.0**	**0.0**	**0.0**	**0.0**

Organophosphines											
Tributylphosphine	10.1	8.2	0.0	47.6	0.0	0.0	0.0	0.0	0.0	0.0	0.0
Triphenylphosphine oxide	736.5	708.2	667.6	754.3	20.3	0.0	22.8	47.3	18.4	9.7	15.4
Total	**746.6**	**716.4**	**667.6**	**801.9**	**20.3**	**0.0**	**22.8**	**47.3**	**18.4**	**9.7**	**15.4**
Plasticizers											
Terephthalic Acid	0.0	0.0	117.5	0.0	46.1	0.0	0.0	0.0	0.0	0.0	0.0
Butyl phthalate	3051.3	246.8	63667.5	19032.2	308.3	63.0	215.9	178.3	85.4	4.8	204.7
Butyl hexyl phthalate	46.9	26.0	1315.2	553.5	249.9	27.6	28.8	68.4	68.5	3.6	52.6
Bis(2-ethylhexyl) phthalate	1126.1	302.8	19645.4	6630.1	213.9	41.8	499.3	668.4	228.5	83.5	162.6
Phthalic Anhydride	0.0	0.0	264.0	51.0	0.0	0.0	0.0	0.0	0.0	0.0	0.0
Total	**4224.3**	**575.6**	**85009.5**	**26266.8**	**818.3**	**132.4**	**744.0**	**915.1**	**382.4**	**91.9**	**419.9**
Other											
Unresolved Complex Mixture	0.0	0.0	0.0	0.0	17252.5	9950.9	0.0	0.0	0.0	0.0	73902.9
Total compounds	**5539**	**2018**	**87362**	**31425**	**19120**	**10860**	**1487**	**1400**	**3011**	**6846**	**74565**

[a]Carbon Preference Index. CPI = $(C_{23}+C_{25}+C_{27}+C_{29})/(C_{24}+C_{26}+C_{28}+C_{30})$

Appendix 4.1. Elemental weight percentages for individual samples of trilobites, from microprobe WDS analysis. Section orientation refers to direction of cuts for thin section: transverse cuts were made across the cephalon and through the thorax, while longitudinal cuts were made through the central axis and distally offset from the center. Cone-in-cone and sediment associated with each sample were also measured, as was a Taylor calcite standard.

Sample Type	Section Orientation	Ca	Mg	Fe	S
Peronopsis					
glabellar	transverse cephalic	38.15	0.35	0.73	0.01
glabellar	transverse cephalic	35.09	0.32	0.51	0.01
thoracic	longitudinal central	38.20	0.32	0.71	0.02
thoracic	longitudinal central	38.62	0.33	0.58	0.01
thoracic	longitudinal central	38.50	0.34	0.66	0.01
thoracic	longitudinal central	40.73	0.27	0.22	0.01
thoracic	longitudinal central	37.93	0.27	0.63	0.00
pygidial	longitudinal central	39.77	0.30	0.65	0.00
Mean, exoskeleton		*38.37*	*0.31*	*0.59*	*0.01*
cone-in-cone	transverse cephalic	39.95	0.10	0.09	-0.01
cone-in-cone	longitudinal central	39.03	0.14	0.42	0.01
Mean, cone-in-cone		*39.49*	*0.12*	*0.25*	*0.00*
sediment	transverse cephalic	31.64	0.36	0.52	0.05
sediment	longitudinal central	27.23	0.33	0.55	0.02
Mean, sediment		*29.43*	*0.35*	*0.54*	*0.03*
Elrathia kingii					
molts					
cephalic	longitudinal distal	33.00	0.46	0.67	0.00
thoracic	transverse thoracic	41.16	0.44	0.60	0.01
thoracic	transverse thoracic	39.18	1.50	0.08	0.02
thoracic	transverse thoracic	39.40	0.38	0.18	-0.01
thoracic	transverse thoracic	38.96	0.32	0.65	-0.01
thoracic	longitudinal distal	38.48	0.59	0.41	0.01
thoracic	longitudinal distal	38.14	0.50	0.61	0.01
thoracic	longitudinal distal	14.01	0.48	0.00	0.02
pygidial	longitudinal distal	37.57	1.15	0.25	0.05

pygidial	longitudinal distal	39.11	0.45	0.39	0.05
Mean, exoskeleton		*35.90*	*0.63*	*0.38*	*0.02*
cone-in-cone	transverse thoracic	40.89	0.10	0.29	0.00
cone-in-cone	longitudinal distal	40.60	0.11	0.14	0.01
Mean, cone-in-cone		*40.74*	*0.11*	*0.22*	*0.01*
sediment	transverse thoracic	4.89	2.01	2.92	0.00
sediment	longitudinal distal	11.89	2.05	3.21	0.01
sediment	longitudinal distal	1.51	2.41	2.36	0.01
Mean, sediment		*6.70*	*2.23*	*2.78*	*0.01*
sulfide inclusion	longitudinal distal	0.03	0.02	54.26	56.26
***Elrathia kingii* whole**					
glabellar	transverse cephalic	19.73	0.16	0.26	0.01
glabellar	transverse cephalic	19.02	0.35	0.18	0.00
glabellar	transverse cephalic	25.73	0.15	0.40	-0.01
thoracic	longitudinal central	38.52	0.43	0.36	0.04
thoracic	longitudinal central	38.33	0.37	0.40	0.03
thoracic	longitudinal central	29.74	0.36	0.38	0.02
thoracic	longitudinal central	37.69	1.01	0.34	0.02
thoracic	longitudinal central	21.35	0.59	0.16	0.01
thoracic	longitudinal central	39.24	0.52	0.30	0.01
thoracic	longitudinal central	42.30	0.21	0.04	0.00
pygidial	longitudinal central	34.40	1.25	2.18	-0.01
Mean, exoskeleton		*31.46*	*0.49*	*0.45*	*0.01*
cone-in-cone	transverse cephalic	39.72	0.14	0.28	0.00
cone-in-cone	transverse cephalic	41.14	0.09	0.22	-0.01
cone-in-cone	transverse cephalic	39.02	0.29	0.44	-0.01
cone-in-cone	longitudinal central	19.22	0.30	0.28	0.01
Mean, cone-in-cone		*34.78*	*0.21*	*0.30*	*0.00*
sediment	longitudinal central	0.07	0.47	0.83	0.00
Taylor Calcite standard					
standard		20.19	0.00	-0.05	-0.01
standard		20.16	0.00	0.06	-0.01
standard		20.19	0.00	-0.05	-0.01
standard		20.11	0.00	0.00	0.00

Appendix 5.1. Total carbon and sulfur data, from infrared absorption spectrometry. Alpha Resources AR 4007 ore standard was run before and after specimens, and blank crucibles were also run.

Sample	Total C (wt. %)	Total S (wt. %)
Standard	7.17	3.83
Standard	7.18	4.31
Standard	7.44	4.42
Standard	7.22	4.65
Standard	7.18	3.42
Standard	7.20	3.35
1	3.16	0.11
2	5.84	0.04
3	3.05	0.06
4	3.50	0.03
5	2.89	0.12
6	3.21	0.00
7	2.92	0.12
8	3.14	0.00
9	4.30	0.11
10	2.93	0.09
11	4.64	0.00
12	2.63	0.00
13	6.73	0.00
14	3.45	0.06
15	3.06	0.12
16	4.41	0.04
17	3.13	0.00
18	3.39	0.08
19	5.20	0.00
20	4.75	0.00
21	3.16	0.02
22	5.12	0.00
23	5.25	0.00
24	3.98	0.00
25	3.87	0.00
Blank	0.05	0.02
Blank	0.02	0.00
Standard	7.34	3.25
Standard	7.32	3.35

Appendix 5.2. Total inorganic carbon data, from infrared absorption spectrometry. Alpha Resources AR 4007 ore standard was run before and after specimens. Some specimens were run multiple times, and their data were averaged to represent that sample.

Sample	Inorganic C (wt. %)
Standard	7.28
Standard	7.17
Standard	7.43
Standard	7.28
1	2.89
2	3.92
3	3.03
4	3.38
5	2.71
6	2.99
7	2.60
8	2.92
9	4.04
10	2.75
10	2.62
11	2.63
12	2.36
13	6.53
14	3.22
15	2.70
16	5.43
17	2.97
18	3.13
19	4.91
20	4.31
21	2.79
22	4.85
23	4.88
24	3.85
25	3.43
25	3.75
25	3.76
Standard	7.39

Appendix 5.3. Weight percent S_{py} from Cr reduction analysis.

Sample	Wt. % S_{pyr}
1	0.14
2	0.09
3	0.12
4	0.06
5	0.16
6	0.03
7	0.19
8	0.19
9	0.13
10	0.25
11	0.06
12	0.12
13	0.09
14	0.15
15	0.25
16	0.07
17	0.02
18	0.24
19	0.15
20	0.19
21	0.17
22	0.17
23	0.15
24	0.04
25	0.02

Appendix 5.4. Mg, Al, Ca, Mn and Fe data from sequential Fe extraction. 25 samples and a blank were analyzed by ICP-MS after extracting metals from sediments in acetate, dithionite, and oxalate solutions, representing reactive Fe from carbonates, simple oxides, and multivalent oxides, respectively.

	Raw ICP-MS Data (counts)					Mg	Al	Ca	Mn	Fe
Sample	**^{24}Mg**	**^{27}Al**	**^{43}Ca**	**^{55}Mn**	**^{56}Fe**	**wt. %**	**wt. %**	**wt. %**	**ppm**	**wt. %**
Acetate										
1	1.33	0.042	8.79	25.79	0.71	1.22	0.04	8.08	23.70	0.65
2	0.87	0.012	18.36	33.11	0.59	0.86	0.01	18.34	33.07	0.59
3	0.90	0.022	7.28	20.06	0.52	0.89	0.02	7.22	19.88	0.51
4	1.24	0.016	8.95	25.25	0.69	1.30	0.02	9.39	26.48	0.72
5	0.74	0.005	5.47	16.03	0.44	0.81	0.01	5.98	17.52	0.48
6	1.07	0.008	7.29	22.19	0.58	1.10	0.01	7.51	22.85	0.60
7	1.06	0.010	5.98	19.44	0.57	1.10	0.01	6.19	20.12	0.59
8	0.99	0.013	7.61	20.52	0.58	1.02	0.01	7.83	21.12	0.60
9	1.29	0.014	11.36	30.05	0.74	1.24	0.01	10.88	28.79	0.71
10	0.75	0.013	7.72	16.54	0.43	0.72	0.01	7.37	15.81	0.41
11	0.98	0.017	16.57	34.43	0.57	1.00	0.02	16.94	35.19	0.59
12	1.13	0.024	6.79	19.31	0.56	1.12	0.02	6.76	19.23	0.56
13	0.70	0.007	19.00	32.33	0.46	0.71	0.01	19.44	33.09	0.47
14	1.19	0.015	8.31	24.77	0.68	1.13	0.01	7.88	23.48	0.64
15	0.96	0.021	5.96	19.57	0.59	0.95	0.02	5.93	19.47	0.59
16	0.77	0.007	11.22	25.10	0.46	0.70	0.01	10.15	22.71	0.41
17	1.13	0.024	7.70	22.07	0.64	1.12	0.02	7.67	21.97	0.64
18	1.34	0.020	8.81	25.87	0.71	1.28	0.02	8.41	24.69	0.68
19	0.87	0.017	13.71	26.44	0.54	0.87	0.02	13.75	26.52	0.54
20	1.02	0.012	14.81	31.35	0.56	0.96	0.01	13.88	29.39	0.52
21	0.60	0.017	7.26	14.82	0.35	0.62	0.02	7.40	15.10	0.35
22	1.07	0.042	16.58	32.37	0.67	1.05	0.04	16.34	31.91	0.66
23	0.90	0.029	16.26	32.43	0.56	0.82	0.03	14.93	29.77	0.52
24	0.77	0.012	12.20	41.78	0.25	0.77	0.01	12.18	41.71	0.25
25	0.72	0.018	10.51	39.38	0.24	0.69	0.02	10.16	38.05	0.23
Blank	-0.01	-0.027	-0.14	-2.89	-0.12	0.00	0.00	-0.01	-0.28	-0.01
Dithionite										
1	0.05	0.011	0.41	3.58	0.05	0.05	0.01	0.38	3.26	0.04
2	0.04	0.008	0.49	3.18	0.02	0.04	0.01	0.47	3.02	0.02
3	0.04	0.008	0.22	2.88	0.02	0.04	0.01	0.21	2.82	0.02
4	0.05	0.013	0.36	3.41	0.18	0.05	0.01	0.36	3.46	0.18
5	0.04	0.011	0.31	3.06	0.04	0.04	0.01	0.32	3.17	0.05
6	0.04	0.012	0.25	3.13	0.16	0.04	0.01	0.25	3.10	0.16
7	0.04	0.009	0.24	2.91	0.07	0.04	0.01	0.24	2.90	0.07
8	0.05	0.010	0.32	3.15	0.03	0.05	0.01	0.32	3.12	0.03
9	0.05	0.009	0.33	3.33	0.03	0.05	0.01	0.32	3.26	0.03

10	0.04	0.009	0.29	3.04	0.04	0.04	0.01	0.26	2.76	0.03
11	0.04	0.019	0.34	3.34	0.27	0.04	0.02	0.34	3.31	0.27
12	0.04	0.015	0.25	3.04	0.17	0.04	0.01	0.25	3.04	0.17
13	0.04	0.007	0.45	3.21	0.03	0.04	0.01	0.45	3.20	0.03
14	0.05	0.010	0.29	3.02	0.04	0.05	0.01	0.29	3.02	0.04
15	0.05	0.009	0.28	2.98	0.02	0.05	0.01	0.28	3.02	0.02
16	0.04	0.011	0.37	3.28	0.14	0.04	0.01	0.34	3.04	0.13
17	0.04	0.012	0.22	2.94	0.17	0.04	0.01	0.23	3.03	0.17
18	0.05	0.010	0.30	3.09	0.02	0.05	0.01	0.28	2.86	0.02
19	0.05	0.009	0.43	3.35	0.03	0.05	0.01	0.42	3.31	0.03
20	0.06	0.011	0.52	3.54	0.03	0.06	0.01	0.54	3.63	0.03
21	0.04	0.011	0.39	3.36	0.05	0.05	0.01	0.40	3.38	0.05
22	0.04	0.010	0.40	3.37	0.03	0.05	0.01	0.41	3.44	0.03
23	0.05	0.010	0.53	3.52	0.05	0.04	0.01	0.50	3.28	0.05
24	0.04	0.026	0.27	3.53	0.32	0.04	0.02	0.26	3.43	0.31
25	0.04	0.028	0.26	3.48	0.36	0.04	0.03	0.24	3.24	0.34
Blank	0.02	0.004	0.12	2.39	-0.01	0.00	0.00	0.01	0.24	0.00
Oxalate										
1	0.02	0.018	0.03	0.19	0.05	0.02	0.02	0.03	0.17	0.05
2	0.04	0.007	0.04	0.83	0.06	0.04	0.01	0.04	0.81	0.06
3	0.02	0.015	0.03	0.12	0.05	0.02	0.01	0.03	0.12	0.05
4	0.02	0.037	0.04	0.13	0.05	0.02	0.04	0.04	0.13	0.06
5	0.02	0.012	0.03	0.07	0.04	0.02	0.01	0.03	0.07	0.04
6	0.01	0.010	0.03	-0.01	0.04	0.01	0.01	0.03	-0.01	0.04
7	0.02	0.014	0.03	0.05	0.04	0.02	0.01	0.03	0.05	0.04
8	0.03	0.060	0.04	0.18	0.05	0.03	0.06	0.04	0.18	0.05
9	0.04	0.014	0.04	0.49	0.06	0.03	0.01	0.03	0.47	0.05
10	0.02	0.016	0.03	0.10	0.05	0.02	0.02	0.03	0.10	0.04
11	0.02	0.021	0.04	0.07	0.06	0.02	0.02	0.04	0.07	0.06
12	0.02	0.044	0.04	0.02	0.05	0.02	0.05	0.04	0.03	0.05
13	0.04	0.014	0.03	0.61	0.07	0.04	0.01	0.04	0.64	0.07
14	0.03	0.038	0.04	0.18	0.05	0.03	0.04	0.04	0.18	0.05
15	0.03	0.033	0.03	0.14	0.05	0.03	0.03	0.04	0.14	0.05
16	0.03	0.017	0.03	0.22	0.05	0.03	0.02	0.03	0.21	0.05
17	0.02	0.033	0.04	0.09	0.05	0.02	0.03	0.04	0.10	0.06
18	0.03	0.019	0.04	0.22	0.05	0.03	0.02	0.04	0.22	0.05
19	0.04	0.029	0.04	0.32	0.06	0.04	0.03	0.04	0.34	0.06
20	0.04	0.022	0.07	0.51	0.06	0.04	0.02	0.07	0.50	0.06
21	0.03	0.060	0.05	0.27	0.06	0.03	0.06	0.05	0.28	0.06
22	0.03	0.037	0.04	0.44	0.06	0.04	0.04	0.04	0.46	0.07
23	0.03	0.014	0.03	0.42	0.06	0.03	0.01	0.03	0.42	0.06
24	0.02	0.043	0.04	0.09	0.10	0.02	0.04	0.04	0.09	0.10
25	0.01	0.022	0.04	0.04	0.07	0.01	0.02	0.04	0.04	0.08
Blank	0.00	-0.008	0.03	-0.07	0.03	0.00	0.00	0.00	-0.01	0.00

Appendix 5.5. Metal concentrations from total metal digest. Some samples were analyzed twice. All units are in ppm.

Sample	^{23}Na	^{24}Mg	^{27}Al	^{31}P	^{39}K	^{44}Ca	^{47}Ti	^{56}Fe	^{51}V	^{52}Cr	^{55}Mn	^{59}Co
1	3553.2	29698.7	91302.3	285.5	21669.0	20140.5	3588.4	33295.8	97.87	84.78	270.95	16.67
2	2440.0	18958.5	41009.6	101.6	9328.9	35996.1	2165.4	26122.0	95.79	84.68	335.66	25.99
3	3105.9	18301.2	61700.4	145.9	17684.7	12701.8	2167.4	22397.6	102.82	89.93	310.39	13.21
4	3312.8	21755.6	68629.6	369.6	21393.9	18194.2	2643.3	24364.3	73.27	61.60	323.94	11.48
5	2995.9	26188.3	83914.5	215.4	19055.3	18301.2	3582.8	33362.0	53.40	45.81	443.16	8.37
6	2773.7	24191.0	75711.6	146.3	17124.3	19758.4	3496.2	31614.4	93.29	83.15	305.50	13.50
6	3132.4	25225.3	69444.8	167.3	18871.9	16966.3	2982.6	28119.3	94.77	82.95	335.56	13.90
7	2546.0	16940.9	53344.6	153.0	16191.9	9502.2	2124.1	18372.5	70.92	62.36	392.26	11.46
8	2871.5	21261.4	70565.7	61.3	17134.5	16304.0	2823.6	27951.1	85.65	75.92	247.57	13.23
9	2779.3	25123.4	59203.8	170.5	13720.8	25495.3	2872.6	31838.6	70.21	60.78	476.94	10.41
10	3589.4	24496.7	83812.6	237.0	21113.7	17455.4	3022.9	27237.8	82.49	78.72	315.07	12.46
11	3080.9	23559.3	69241.0	197.0	14026.5	32042.4	2919.9	30483.3	95.53	81.98	339.73	15.10
12	3195.6	24420.3	86818.7	288.9	19896.0	15514.3	3331.6	30651.5	81.83	73.01	253.22	19.60
13	2752.8	17710.2	38482.5	7.7	7831.0	44265.3	1816.4	25444.4	83.71	69.50	259.18	21.16
14	2926.1	20823.2	56248.7	119.0	17159.9	15733.3	2488.9	23192.4	93.60	80.14	310.08	17.23
15	2635.1	21200.3	63076.0	257.0	15840.3	16028.9	3146.7	31492.2	65.73	55.94	320.22	9.95
16	3105.9	18474.4	59917.1	20.0	14444.3	26020.1	2511.8	24410.1	68.43	58.69	453.81	10.36
17	3675.0	29010.9	89264.3	254.3	19473.1	18097.4	3223.1	29296.2	84.27	74.44	285.22	6.89
18	3597.1	27339.7	79227.2	139.9	17659.2	17577.7	2829.3	28501.4	54.47	45.76	345.39	8.27
19	2096.1	14755.1	32592.7	8.8	9058.9	20894.6	1522.9	17480.9	80.45	69.04	276.81	17.63
20	3352.0	20680.6	63432.7	132.2	14281.3	30524.1	2670.8	27793.2	82.34	72.40	247.16	18.37
21	2833.3	19254.0	68222.0	84.6	16956.1	15921.9	2495.5	23467.5	76.22	65.98	301.32	8.52
22	3173.2	23452.3	57216.8	126.5	12177.0	31996.6	2320.8	28134.6	78.46	68.94	272.79	10.98
23	3673.5	23854.8	67661.5	135.2	12890.3	39012.4	2939.3	31268.0	71.58	61.04	344.47	10.72
24	2769.6	24140.1	68833.4	224.2	15820.0	25429.1	2635.1	33637.1	61.04	51.20	334.23	8.71
24	2271.3	20884.4	61598.5	75.6	13945.0	23151.7	2452.7	29000.7	59.46	53.09	414.53	9.80
25	2585.2	25373.1	71380.9	204.1	15534.6	29601.9	3104.4	36113.3	63.38	52.27	327.15	10.37
Std	2036.5	8824.5	58898.1	290.5	22438.4	1917.2	3489.1	60579.5	145.00	54.26	281.04	40.64
Std	2081.8	7515.1	56299.7	322.6	20925.1	1681.9	3366.3	59305.7	150.35	55.28	288.38	40.54

Sample	^{60}Ni	^{63}Cu	^{66}Zn	^{75}As	^{88}Sr	^{90}Zr	^{98}Mo	^{111}Cd	^{185}Re	^{208}Pb	^{232}Th	^{238}U
1	35.72	27.16	69.29	6.30	253.53	60.27	5.18	7.16	0.53	11.10	14.43	3.12
2	37.56	22.51	87.63	6.99	268.91	55.23	2.83	7.05	0.49	10.29	14.90	3.04
3	31.91	26.34	63.53	5.49	197.89	52.63	9.83	7.06	0.50	7.79	13.03	2.83
4	27.49	13.84	74.59	3.62	308.76	47.33	4.26	6.99	0.50	13.33	9.53	2.75
5	24.07	14.89	64.15	3.19	441.48	43.65	3.29	7.11	0.50	6.38	8.13	2.58
6	32.04	22.41	58.69	5.73	199.11	50.29	11.24	7.12	0.50	6.54	10.57	2.64
6	33.58	23.44	61.29	7.90	234.17	69.75	10.51	7.67	0.74	7.49	13.88	3.10
7	31.24	15.99	77.55	4.47	392.42	48.12	4.98	7.16	0.50	87.12	10.96	2.84
8	29.52	18.07	58.59	6.07	193.25	49.39	3.12	7.11	0.50	11.54	12.16	2.48
9	28.60	18.00	63.18	2.91	282.21	52.17	2.38	7.12	0.50	11.12	10.32	2.07
10	30.38	16.95	57.32	5.81	251.08	40.36	1.78	7.11	0.50	9.54	11.56	2.30
11	33.35	20.26	83.20	4.95	239.11	50.22	1.59	7.11	0.50	20.88	11.58	2.36
12	31.93	16.83	60.43	5.62	220.36	40.87	1.50	7.09	0.50	8.03	10.42	2.15
13	31.29	18.69	55.03	6.50	212.61	34.65	1.27	7.18	0.50	13.78	9.38	1.98
14	35.06	18.23	75.92	4.07	224.89	45.01	1.25	7.23	0.50	8.46	11.58	2.39
15	23.34	17.76	60.83	3.63	305.90	47.92	1.16	7.07	0.49	35.51	9.16	2.35
16	27.64	17.45	60.73	2.88	300.55	49.13	1.09	7.12	0.49	10.29	9.27	2.22
17	28.50	18.27	58.49	3.51	196.00	49.71	1.04	7.11	0.50	6.84	10.50	2.22
18	23.92	13.49	51.05	2.85	329.14	41.59	1.08	7.07	0.50	10.32	6.92	2.14
19	31.27	16.18	64.66	4.09	217.45	69.80	0.98	7.10	0.50	8.11	10.98	2.36
20	31.49	18.36	65.42	5.54	214.30	39.81	0.95	7.11	0.49	9.06	9.78	2.20
21	25.66	19.14	62.62	3.83	309.98	43.05	0.99	7.36	0.49	7.41	9.72	2.49
22	29.45	15.90	51.77	3.68	193.41	51.31	0.85	7.16	0.50	5.40	10.31	2.25
23	28.56	14.60	76.37	3.46	277.27	36.90	0.92	7.13	0.50	5.60	9.09	2.14
24	25.49	14.38	65.98	3.15	336.63	55.59	1.02	7.09	0.50	6.95	8.36	2.44
24	25.51	16.05	58.44	3.90	281.96	42.95	3.74	7.20	0.51	9.71	9.89	2.24
25	24.94	15.15	69.80	3.52	346.20	47.38	0.98	7.12	0.49	5.91	8.51	2.51
Std	83.91	49.70	59.20	70.72	58.75	65.83	141.44	7.28	0.50	27.29	9.60	41.24
Std	80.81	47.84	56.35	70.62	54.87	65.32	133.13	7.29	0.50	25.94	9.23	40.71